

Study of Cell Nucleation in Nano Polymer Foams: An SCFT Approach

by

Yeongyoon Kim

A thesis
presented to the University of Waterloo
in fulfillment of the
thesis requirement for the degree of
Doctor of Philosophy
in
Physics

Waterloo, Ontario, Canada, 2012

© Yeongyoon Kim 2012

I hereby declare that I am the sole author of this thesis. This is a true copy of the thesis, including any required final revisions, as accepted by my examiners.

I understand that my thesis may be made electronically available to the public.

Abstract

This thesis is about “nano-cellular” polymer foams, i.e., to understand nano-bubble nucleation and growth mechanisms, we used Self-Consistent Field Theory(SCFT) for the research.

Classical Nucleation Theory (CNT) is often used to calculate nucleation rates, but CNT has assumptions which break down for a nano-sized bubble: it assumes planar sharp interfaces and bulk phases inside bubbles. Therefore, since the size of a nano-sized bubble is comparable to the size of the polymer molecule, we assumed that a bubble surface is a curved surface, and we investigated effects of curvature on the nucleation barrier. SCFT results show that sharper curvatures of smaller s cause a higher polymer configurational entropy and lower internal energy, and also the collapse of the bulk phase for smaller bubbles causes low internal energy. Consequently, the homogenous bubble nucleation barrier for curved surfaces is much smaller than flat surface (CNT prediction).

We calculated direct predictions for maximum possible cell densities as a function of bubble radius without calculation of nucleation barrier or nucleation rates in CNT. Our results show higher cell densities at higher solvent densities and lower temperatures. Moreover, our cell density prediction reveals that rather than surface tension, the volume free energy, often labelled as a pressure difference in CNT, is the dominant factor for both cell densities and cell sizes. This is not predicted by CNT.

We also calculated direct predictions for the maximum possible cell densities as a function of system volume in compressible systems. With an assumption that system pressure has an optimal pressure which gives the maximal density of good quality foams (bulk phase inside bubble), we calculated the inhomogeneous system pressure, the homogeneous system, and cell density as a function of system volume.

Maximal cell prediction in compressible system shows the incompressible system prediction is the upperbound maximal cell density, and qualitatively consistent with the compressible system results - higher cell densities at low temperatures and high solvent densities.

In addition, our results show a bigger expansion as well as a high cell density at low temperature and high solvent density, but temperature is a more dominant factor than the solvent density. From our results, we assume that a quick pressure dropping is required to get a better quality foam of a higher cell density.

Acknowledgements

I would like to sincerely thank my supervisor, Prof. Russell B. Thompson. Without his help, this thesis wouldn't have been completed. It has been a precious time for me to learn from him and work with him for the past 4 years.

I would like to thank to my Graduate Committee members, Prof. Pu Chen, Prof. Bizheva Kostadinka, Prof. Bae-Yeun Ha, and Prof. Robert Wickham for their strong support and kind guidance during my Ph. D. program. I would like to thank to my Defence Committee members, Prof. Apichart Linhananta, and Prof. Cecile Devaud for their kind and helpful comments on this thesis.

Especially, I would like to thank Prof. Chul B. Park for his help and encouragement. The conversations with him were very helpful for the researching this thesis.

I would like to thank to my colleagues in my office - Azadeh Bagheri, Kier von Konigslow, Yu-Cheng Su, Murthy SRC Ganti, Zheng Ma, Dr. Ying Jiang, Dr. Zi jian Long, Dr. Sergey Mkrtchyan, and Dr. Wuyang Zhang, and my friends - Miok Park and Dr. Gopika Sreenilayam. They were always willing to help me whenever I needed. It was a good time to have been with them during my Ph. D. program.

And, especially I would like to thank to my current roommate, Ms. Becky Lawn, for her kind help with the grammar correction in this thesis.

Lastly, I would like to thank my beloved sisters and brother for their love. I dedicate this thesis to my late parents, and I cannot help giving thanks to God since I believe in his guidance in my life.

Dedication

I dedicate this thesis to my parents.

Table of Contents

List of Figures	viii
1 Introduction	1
1.1 Introduction to Polymer Foam	2
1.2 Background literature	5
1.2.1 Theory	5
1.2.2 Experiment	8
1.3 Outline of Thesis	11
2 Basic Theory	12
2.1 Classical Nucleation Theory	12
2.2 Self - Consistent Field Theory	14
2.2.1 Modeling	14
2.2.2 Meanfield Theory and Density Functional Method	16
2.2.3 Numerical Method	19
2.3 Theory for a Compressible System	19
2.3.1 Compressible Lattice Liquid Theory	19
2.3.2 Equation of State	22

3	Microscopic Origin of the Failure of Classical Nucleation Theory	24
3.1	Theory	25
3.2	Surface Tension, Volume Free Energy Density and Nucleation Barrier in a Curved Surface and a Flat Surface	29
3.3	Microscopic Origins of the Failure of CNT	35
3.4	Discussion and Conclusion	41
4	Maximal Cell Density and Temperature Effect on Cell Density	43
4.1	Calculation of Bubble Number Density	44
4.2	The "Best" Foam	45
4.3	Temperature Effect on the Bubble Number Density	52
4.4	Discussion and Conclusion	58
5	Maximal Cell Density in Compressible Systems	59
5.1	Theory	60
5.1.1	Optimal Pressure	60
5.2	Maximal Cell Density	66
5.2.1	Different Temperature Cases with the Same Initial High Pressure	66
5.2.2	Different Solvent Density Cases at the Same Temperature	75
5.2.3	Different Temperature Cases with the Same Solvent Volume Fraction	75
5.3	Discussion and Conclusion	78
6	Conclusions	82
	Permissions	87
	References	88

List of Figures

1.1	Thermoplastic foaming process.	3
1.2	Schematic phase diagram of polymer solution at constant temperature using pressure p and solvent molar fraction x as variables. In this diagram, the pressure quench ends in the unstable region,i.e., spinodal region. However, if the pressure quench ends in metastable region, then phase separation will start by homogeneous nucleation.	4
1.3	(a) Phase diagram at temperature $k_B T/\epsilon = 0.75 \approx 41^\circ\text{C}$ as a function of pressure p and molar fraction x . Three constant nucleation barrier line are shown. We can see pressure jump would induce bubble nucleation. From [39] (b) Nucleation behavior of a hexadecane + carbon dioxide mixture at $T = 40^\circ\text{C}$. Full circles indicates the starting and ending point at which the homogeneous nucleation is induced by pressure jump. Open circles mark points at which no nucleation occur. From [50]	7
1.4	(a) Processing temperature effect on foam structure. We can see small size bubbles (high cell density) at low temperature. From [47] (b) Effects of (a)pressure drop rate ($-dP/dt$), (b) solvent density, (c) temperature. From [29]	10
2.1	Plot of the nucleation barrier ΔF^* and critical radius R^*	13
2.2	numerical method of solving self -consistent eqs. in real space	20

3.1	(a) Profile of the initial homogeneous system which has initial global volume fraction values. (b) Profile of the bulk phase separated homogenous system which would be formed if there was no interface. Each bulk system has volume fraction values on either side of interface of the inhomogeneous system. Each bulk system volume V_1 and V_2 are determined by conservation of molecules. (c) Profile of the final inhomogeneous system after formation of a bubble, i.e., after formation of interface	27
3.2	Homogeneous free energy versus global solvent volume fraction at $\chi N = 140$	30
3.3	(a) Profiles of local volume fractions of three different sizes of bubble in the flat surface case. (b) In this blow up graph, we can see that at the outside of a bubble, three different sizes of bubble have the same solvent volume fraction value, which is the equilibrium value.	31
3.4	(a) Profiles of local volume fractions of three different sizes of bubble in the curved surface case and one profile of a flat surface. (b) In this blow up graph, we can see that in curved surface, three different sizes of bubble have different solvent volume fraction values at the outside of a bubble. Compared to the flat surface, in curved surface, smaller bubbles have more deviated volume fraction values from the equilibrium solvent volume fraction value.	32
3.5	(a) Surface tension values versus radius of a bubble. For curved surfaces, surface tension is decreasing for the smaller bubble in contrast to the constant value of surface tension for the flat surface. (b) The negative of volume free energy density($-\widetilde{\Delta F_V}$) versus radius of a bubble. As the sign of $\widetilde{\Delta F_V}$ is minus, the sign of $-\widetilde{\Delta F_V}$ is positive. The negative volume free energy density is increasing for smaller bubbles in contrast to the constant value of volume free energy density for the flat surface.	33
3.6	The solid line shows the free energy necessary to form a bubble of radius R ($\widetilde{\Delta F}(R)$) in the flat surface case. The open circle and dotted line shows the free energy necessary to form a bubble of radius R ($\widetilde{\Delta F}(R)$) in the curved surface case.	34
3.7	Thermodynamic components of surface tension versus bubble radius R . Increasing polymer configurational entropy is the main cause, and the decreasing internal energy is a secondary cause of decreasing surface tension for smaller bubbles. Below $0.9 R_g$, the internal energy shows a sharper decreasing.	36

3.8	In (a) and (b) the polymer has same configuration. However, for the flat surface (a), since the surface is flat, the polymer has more contact with solvent causing higher internal energy. (b) In the curved surface, since the surface has curvature, the polymer has less contact with solvent causing lower internal energy.	37
3.9	Thermodynamic components of volume free energy density versus bubble radius R . By same mechanism of surface tension, together with increasing internal energy, increasing entropy is the cause of increasing volume free energy density for smaller bubbles.	38
3.10	(a) Profile of a critical radius of a bubble in which inside the bubble does not reach the perfect bulk phase in case of $\chi N = 120$, $\phi_s = 0.23$. (b) Profile of a bubble with a perfect bulk phase inside a bubble in the case of $\chi N = 120$, $\phi_s = 0.23$. (c) Profile of a critical radius of $\chi N = 160$, $\phi_s = 0.26$ case. We can see a clear collapse of the bulk phase inside the bubble. (d) To compare with (c), one profile of a bubble with perfect bulk phase inside the bubble for the $\chi N = 160$, $\phi_s = 0.26$ case.	39
3.11	Thermodynamic components of surface tension versus bubble radius R for the case of $\chi N = 160$, $\phi_s = 0.26$. Near the critical radius, at a small radius of bubble, the decreasing internal energy becomes a main cause of decreasing surface tension for smaller bubbles.	40
4.1	At $\chi N = 160$ (a) Dimensionless bubble number density versus radius of a bubble. (b) Dimensionless bubble number density at the critical radius of a bubble at different solvent volume fraction systems.	46
4.2	At $\chi N = 160$ (a) Dimensionless bubble surface area per bubble box volume ($\phi_s \times V_{box}$) versus radius of bubble. (b) Dimensionless bubble number density at the radius of the maximum of A/V	47
4.3	At $\chi N = 160$ (a) Solvent volume fraction value at the center of bubble versus radius of the bubble (b) Dimensionless bubble number density at the bubble radius $R = 0.7R_g$ at different solvent volume fraction systems . . .	49
4.4	At $\chi N = 160$, dimensionless bubble number density at different solvent volume fraction systems in view of maximal number density, maximal bubble surface area, and bulk condition at the center of a bubble.	50
4.5	At $\chi N = 160$, (a) Dimensionless surface tension γ versus radius of bubble. (b) - ΔF_V at $R = 0.7R_g$ at different solvent volume fraction systems. . . .	51

4.6	Solvent volume fraction value at the center of a bubble versus radius of the bubble at different solvent volume fraction systems at $\chi N = 160$. (b) Surface tension versus radius of a bubble at different solvent volume fraction systems at $\chi N = 120$ and at $\chi N = 160$	53
4.7	At $\chi N = 120$, (a) Negative volume free energy density ΔF_V and (b) dimensionless bubble number density at different solvent volume fraction systems	54
4.8	At $\chi N = 160$, $\phi_s = 0.29$ and $\chi N = 120$, $\phi_s = 0.29$ (a) Dimensionless bubble number density. (b) ΔF_V versus radius of bubble	56
4.9	At different solvent density systems at $\chi N = 120$ and $\chi N = 160$ (a) $-\Delta F_V$ (b) Dimensionless bubble number density	57
5.1	(a) Plot of several bubble pressures at different system volumes. (b) Blow up of several bubble pressures at $V_{sys} = 1.1V_0$. (c) Three representative bubble pressures at $V_{sys} = 1.1V_0$	63
5.2	(a) Cell density versus bubble radius at different system volumes. (b) A_{bubble}/V_{box} versus bubble radius at different system volume.	64
5.3	(a) Solvent volume fraction value at the center of bubble versus bubble radius at different system volumes. (b) Plot of three optimal pressures of smallest cell, maximum A_{bubble}/V_{box} , and $\varphi_s(0) \approx 1$ at the center of bubble.	65
5.4	At $T = 1.5$ (a) Three optimal pressures versus system volume. (b) Blow up plot of optimal pressure values at $V_{sys} = 1.1V_0$	67
5.5	Three maximal cell densities corresponding to three optimal pressures versus system volume at $T = 1.5$	68
5.6	At $T = 2.0$ (a) Three optimal pressures versus system volume. (b) Blow up plot of optimal pressure values at $V_{sys} = 1.1V_0$	70
5.7	Three maximal cell densities corresponding to the three optimal pressures versus system volume at $T = 2.0$	71
5.8	At $T = 1.5$ and $T = 2.0$ (a) Pressure of the inhomogeneous system and the homogeneous system versus system volume (b) Blow up plot of the pressure at $V = 1.05V_0$. (c) Blow up plot of the pressure at $V = 1.3V_0$	73
5.9	Cell density versus system volume at $T = 1.5$ and $T = 2.0$	74

5.10	At different solvent volume fractions (solubilities) for $\chi N = 120$ (a) Pressure of the inhomogeneous system and the homogeneous system versus system volume (b) Blow up plot of the pressure $V = 1.05V_0$. (c) Blow up plot of the pressure at $V = 1.1V_0$	76
5.11	Cell density versus system volume at different solvent volume fractions (solubilities) for $\chi N = 120$	77
5.12	At $\chi N = 120$, $\phi_s = 0.32$ and $\chi N = 160$, $\phi_s = 0.32$ (a) Pressure of the inhomogeneous system and the homogeneous system versus system volume (b) Blow up plot of pressure at $V = 1.05V_0$. (c) Blow up plot of pressure at $V = 1.1V_0$	79
5.13	Cell density versus system volume at $\chi N = 120$, $\phi_s = 0.32$ and $\chi N = 160$, $\phi_s = 0.32$	80

Chapter 1

Introduction

Microcellular foam is a polymeric foam with a cell size less than $10\ \mu m$ and a cell density greater than $10^9\ \text{cells}/\text{cm}^3$. It was first developed at the Massachusetts Institute of Technology [33] in the early 1980s to increase the toughness of materials and reduce the materials consumption. Because of the small cell size, microcellular foams show increased thermal and electrical insulation and superior mechanical properties. With these benefits, microcellular foams also reduce the material cost.

Therefore, intensive efforts have been made to develop foams with a higher cell density and with smaller bubble sizes such as nano-size. Nanocellular foam is a polymeric foam with cell size less than $0.1\ \mu m$ and cell density greater than $10^{15}\ \text{cells}/\text{cm}^3$. In recent years, several successful implementations of nanocellular foams have been reported [22, 11, 32, 69]. However, due to the high cost and slow production rates, commercial application has been limited.

Thus, for the large -scale production of a high quality foam such as a nanocellular polymeric foam, it is required to understand the mechanism of bubble nucleation and growth that is influenced by foaming processing parameters such as temperature, pressure, solvent concentration, and depressurization rate, etc.

To have foams of a high cell density with small-sized bubbles, a high nucleation rate is required. People often use classical nucleation theory (CNT) for simplicity of approach. However, CNT has been shown to be insufficient in many cases [53, 42, 38, 44], especially for small-size bubble nucleation. Since we investigate nanocellular foams, we used self-consistent field theory (SCFT), which is a mean field equilibrium statistical mechanical theory containing a microscopic model of polymer degrees of freedom. In addition, as the cell size is comparable to the polymer molecular size, we assumed bubble surface as a

curved surface in contrast to the flat surface assumption for a bubble surface in CNT. For simplicity, we used an incompressible polymer + solvent system. We observed that the homogeneous nucleation barrier of the curved surface is much smaller than the corresponding value of the flat surface. We investigated the microscopic origin of this by studying the thermodynamic components of the free energy.

To calculate the bubble number density by using CNT, one needs to calculate an exponential prefactor and integrate over time of the nucleation rate. By using our model, we directly calculated the maximal cell density without the calculation in CNT.

Based on our results, we investigated the cell density dependence on temperature and solvent density. Our results were qualitatively consistent with experimental results, but there was qualitative difference between the expectation of SCFT and CNT. It turns out that surface tension is not a dominant factor for cell density and size.

To investigate a more realistic system, i.e., a compressible system, we used a hole-based SCFT developed by Hong and Noolandi[17]. With an assumption that a system has an optimal pressure which gives the best form, i.e., a foam which have the smallest bubbles that reached the bulk phase at the center, we calculated system pressure, the maximal cell density, expansion ratio, and void fraction as a function of system volume. Based on our result, we investigated cell density, expansion ratio, cell morphology for different processing conditions such as different temperatures and solvent densities.

In the first section, we briefly introduce polymer foam. In section 2, we present background literature of theory and experiment, and in section 3, we outline the thesis.

1.1 Introduction to Polymer Foam

The word "foam" originates from the medieval German word veim which means "froth" [63]; however, the terminology "foam" refers to bubbles dispersed in a dense continuum like a solid. Polymer foams, which consist of polymer matrices with fluid bubble inclusions, are used in furniture, automotive parts, construction materials, insulation board, and many other areas [26].

Foaming is a temperature or pressure controlled phenomenon. Gas foaming can be generated by dropping pressure or temperature. In this thesis we only investigate pres-

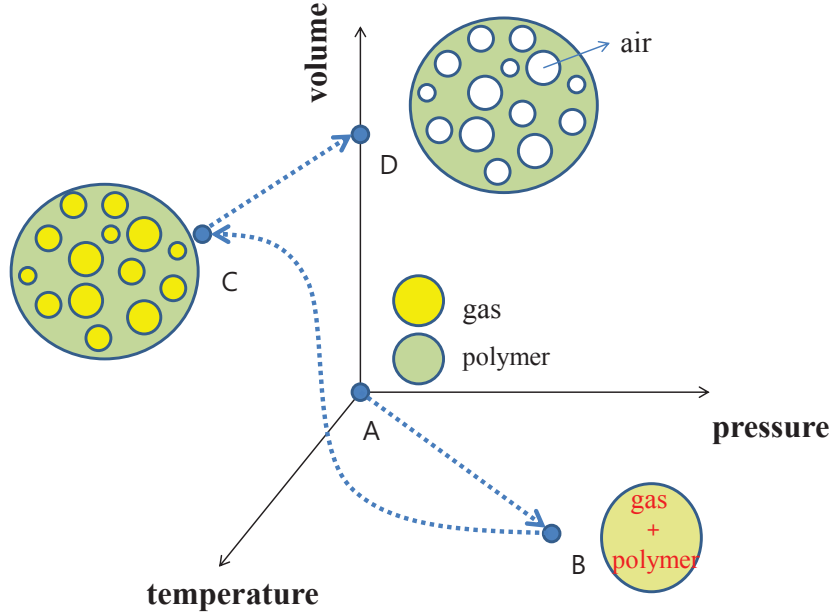


Figure 1.1: Thermoplastic foaming process.

sure induced foaming. Fig.(1.1) explains the process of thermoplastic foaming induced by pressure dropping. First, from state (A) to (B) by raising temperature and pressure, the raw plastic materials is heated and pressurized and blowing agent (solvent) is dissolved at this fluid-like melt to form a homogeneous melt solution. Then, from state (B) to (C), suddenly by dropping pressure, the foaming processing occurs due to the instant supersaturation induced by the pressure drop. And, finally from state (C) to (D) by replacing the gas to air the final foam product is made.

We regard foaming as a phenomenon of a phase transition from one phase to two phases. Fig.(1.2) shows a schematic phase diagram of a compressible polymer solution at constant temperature. In this diagram, variables are pressure p and solvent molar fraction x . We can see the phase separation between the polymer and the molecular solvent is induced by a pressure jump, and Fig.(1.2) shows that the system would be separated two phases, i.e., polymer with some dissolved solvent molecules and solvent (molar fraction $x = 1$) in the vapor phase. In the diagram, it is assumed the pressure jump ends in unstable (spinodal) region. However, if the pressure quench ends in the metastable (nucleation and growth) region, the phase separation will occur by homogeneous nucleation.

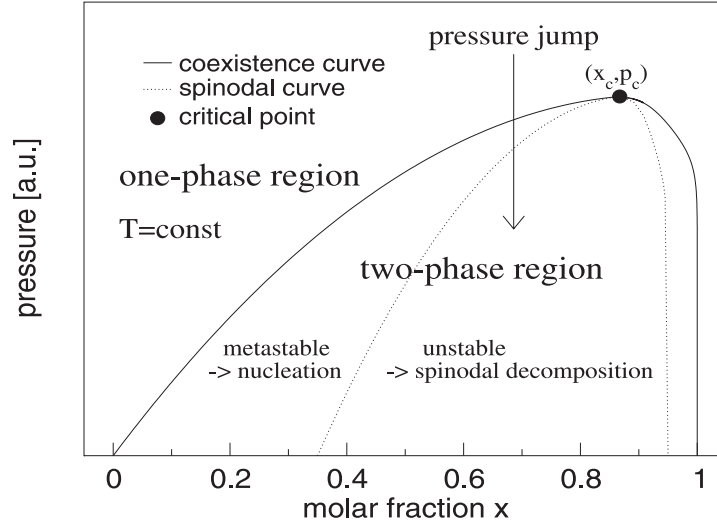


Figure 1.2: Schematic phase diagram of polymer solution at constant temperature using pressure p and solvent molar fraction x as variables. In this diagram, the pressure quench ends in the unstable region, i.e., spinodal region. However, if the pressure quench ends in metastable region, then phase separation will start by homogeneous nucleation.

On the other hand, there are fundamental relationships between foam structure and its properties. The properties of polymeric foams are determined by the following structural parameters: cell density, cell size and its distribution, expansion ratio, and open cell content, etc. The density and distribution of cells are critical parameters in determining the final property of the polymeric foam. Also, the cell size is an important factor. It is well known that insulation ability depends on the cell size. According to studies of microcellular foam with a cell size on the order of 10 microns, small cells provide a better energy absorption capability. In addition, plastics with a high cell density and uniform cell density show superior mechanical properties such as higher toughness as well as better thermal and acoustic insulation properties. [2, 45].

And, the cells are divided into the open cell and closed cell. Open-cells are connected with each other, and closed-cells are discrete, each surrounded by the polymer. Open-cell and closed-cell each has advantages and disadvantages - open cell is desirable in gas exchange, absorption and sound deadening, but has poor mechanical properties. Thus, open cell content is not desirable for closed-cell foams. In addition, the blowing agent(solvent)'s quality, quantity and nature are also important factors for the production of a foamed structure

with certain desired properties.

Therefore, there are enormous efforts to get an insight of mechanisms of bubble nucleation and growth and proper foaming process conditions for a desired foam morphology. In particular, the improvements of quality of foam are sought by reducing the cell size to nanometer dimensions for nanocellular foams.

1.2 Background literature

1.2.1 Theory

Colton and Suh [5, 6] used CNT as the basis to develop a model of the nucleation of microcellular foam with additives. They used a polystyrene-zinc stearate system and used nitrogen and carbon dioxide as additives. They reported that the theoretical and experimental results reasonably agree. However, they considered that homogeneous nucleation and heterogeneous nucleation occur together, and that heterogeneous nucleation dominates because of a high homogeneous nucleation barrier. It is considered that their classical homogeneous nucleation is able to fully describe the nucleation activity.

Goel and Beckman [13] generated microcellular foam by a pressure quench in a CO_2 - swollen poly(methylmethacrylate), PMMA, sample. They used CNT for their model, and found that agreement between experimental data and model calculation is very good at high pressure. But, they observed a limited nucleation at low pressure (~ 10 MPa), and they explained that it could be due to a high heterogeneous nucleation at low pressure. In addition, in their model, for the surface tension, they used the correlation for the surface tension mixture given by Reid[?].

Shukla and Koelling [53] used a modified CNT which accounts for diffusional and viscosity constraints to calculate the rate of homogeneous nucleation of microcellular foam of a polystyrene - CO_2 system. They found that the capillary approximation of CNT is not valid for bubble nucleation. After a correction accounting for the curvature effect of surface tension along the lines suggested by Tolman [59], they observed the theoretically predicted rate is consistent with the experimental results.

On the other hand, there are also Monte Carlo simulation studies of droplet nucleation by using CNT. Neimark and Vishnyakov [42] studied nucleation barriers for droplets in Lennard-Jones fluids. Based on their data by MC simulation, they investigated the limits of applicability of the capillarity approximation of CNT and the Tolman equation. They report that the Tolman equation can not be approximated for small droplets of a radius less than four molecular diameters.

Merikanto and Vehkamäki [38] used CNT based on a liquid drop model. They showed that CNT can be used to fit small cluster sizes, but there was error in modeling the smallest of clusters. They show that the liquid model can be used to calculate the work related to addition of monomer to cluster sizes between 8 to 50 molecules. But they pointed out that the microscopic effect related to the formation of the smallest clusters, the total cluster work given by CNT might introduce a large correction term.

Beyond CNT, Lee and Flumerfelt [24] used the integral overall energy balance and the integral Clausius - Duhem inequality to analyze a bubble nucleation experiment. They observed that for molten low-density polyethylene with dissolved nitrogen, surface tension decreases as the cluster size becomes smaller, and they explained the reduction of surface tension is due to the dissolved gas in molten polymer and small critical cluster size.

As a nonclassical theory for a homogeneous nucleation of gas to liquid, Oxtoby and Evans [44] used a density functional method. They used a grand potential to be a functional of the inhomogeneous density, and used the Yukawa potential. Thus, the gas-liquid surface free energy for a planar interface is inversely proportional to λ . λ is a parameter of Yukawa potential which is related to a range of attractive potential. Oxtoby and Evans observed that the agreement of the nonclassical and classical expectation depends strongly on the λ . For $\lambda = 1$, i.e., the range of attractive potential is equal to the hard sphere diameter, the deviation between nonclassical and classical results for the bubble formation from liquid is much bigger than the liquid formation from gas. Especially, the classical theory predicts no transition to occur because the potential barrier is too high. They also observed that in the density functional calculation, the potential barrier vanished at the spinodal in contrast to the potential barrier which has a finite value at spinodal in CNT.

Ghosh and Ghosh[12] presented a theory for homogeneous nucleation using DFT with a square gradient approximation for the free energy functional to get an analytical expression for the size-dependent free energy formation of a liquid drop. They applied the

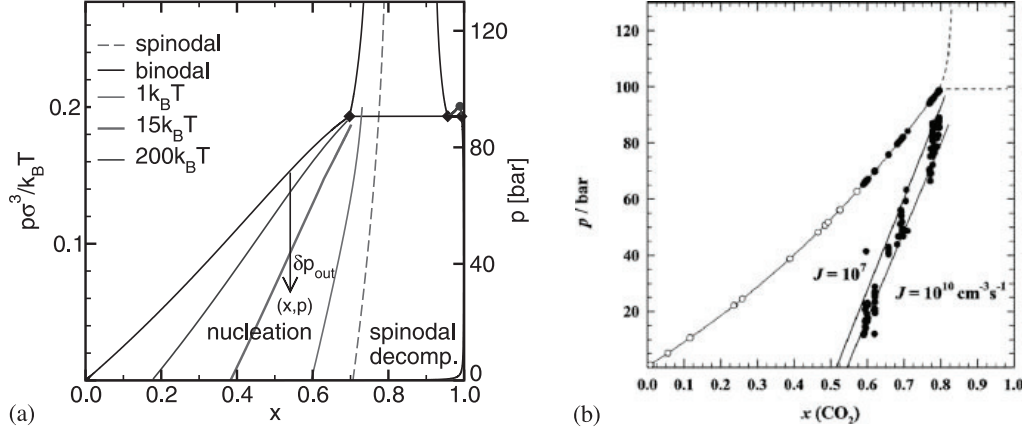


Figure 1.3: (a) Phase diagram at temperature $k_B T / \epsilon = 0.75 \approx 41^\circ\text{C}$ as a function of pressure p and molar fraction x . Three constant nucleation barrier line are shown. We can see pressure jump would induce bubble nucleation. From [39] (b) Nucleation behavior of a hexadecane + carbon dioxide mixture at $T = 40^\circ\text{C}$. Full circles indicates the starting and ending point at which the homogeneous nucleation is induced by pressure jump. Open circles mark points at which no nucleation occur. From [50]

theory for droplet nucleation from supersaturated vapor of Lennard-Jones fluid, and found the nucleation barrier calculated by the nonclassical theory is significantly lower than the prediction of CNT.

Parra and Grana [49] analyzed the influence of attractive pair-potentials in density functional models of homogeneous nucleation. They showed that if asymptotic decay at infinity of attractive potential is strong enough, then the ratio of nucleation barrier of the density functional and corresponding classical result weakly dependent on the form of the pair-potential. However, if the asymptotic decay at infinity is not weak enough, then the nucleation barrier ratio decreases significantly with interaction potential strength.

Binder et. al. [4] used SCFT as a nonclassical theory for homogeneous bubble nucleation in polymer + solvent systems. They chose the mixture of hexadecane with carbon dioxide as a polymer + solvent system. In the SCF calculation, they used the grand canonical ensemble and observed only critical bubbles. As we can see Fig. 1.4, they could reproduce qualitative features of experimental data from Rathke et al. [50], i.e., measured nucleation

rate in hexadecane + CO_2 mixture at $40^\circ C$. They observed that in Fig. 1.4(a), as the molar fraction increases at constant pressure the nucleation barrier decreases, and it vanishes at the spinodal, which is similar what we observe in our research - as pressure drops at constant temperature the nucleation barrier approaches to the zero, i.e., approaches to spinodal.

We used SCFT in this thesis. It is a mean field equilibrium statistical equilibrium theory, but Oxtoby[43] pointed out that in the grand canonical ensemble in which the number of molecules fluctuate, a dynamically unstable state like a critical radius is not stable, but in the canonical ensemble in which the number of molecules is fixed, a system consisting of a critical radius surrounded by original phase is thermodynamically stable.

In microcellular foams Goel and Beckman [13] reported that their results of microcellular foam can be fit with CNT for high pressure, but they observed a limited nucleation at low pressure and explained that it is due to a high heterogeneous nucleation at low pressure. For a homogeneous nucleation, Shukla and Kellings [53] were only able to fit with CNT when they modified their surface tension using the Tolman approximation. However, MC studies [42][38] showed that even the Tolman equation cannot be approximated for small droplets of a radius less than four molecular diameters, and pointed that microscopic effects related to the smallest cluster might introduce a large correction term to CNT expectations. Lee and Flumerfelt [24] showed that surface tension decreases as the cluster size becomes smaller, and the surface tension reduction is the cause of the seriously under-predicted nucleation rate of CNT. However, they couldn't explain the microscopic origin of the surface reduction at smaller cluster sizes. They assumed a perfectly sharp bubble interface and didn't use a model containing polymer degrees of freedom. In this thesis, we used SCFT which is a coarse-grained microscopic model, and investigated the microscopic origin of the failure of CNT.

1.2.2 Experiment

To make a desired foam morphology there have been enormous efforts to choose correct combination of processing conditions such as temperature, solvent concentration, pressure dropping rate, etc.

Goel and Beckman [13], Leung et. al. [29], Ito et. al. [19], Tsivintzelis et. al. [60], Han

et. al. [14] investigated cell density dependence on solvent density by using a polymer with CO_2 . Their results show higher cell density with increased solvent density. Thus, there have been also intensive researches for the solubility. [31, 15, 52, 30]

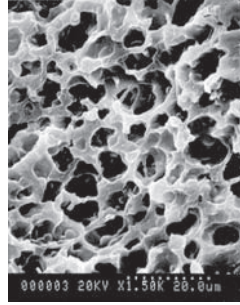
Also, Goel and Beckman [13], Leung et. al. [29], Tsivintzelis et. al. [60], Matuana et. al. [37], Wong et. al. [65] also investigated cell density dependence on temperature by using a polymer with CO_2 . Higher cell density with lower temperature is observed

Surface tension is known to be a crucial factor in polymer foaming processes. Thus, there is much research about the surface tension. [48, 57, 57, 64, 9, 8, 27] Park et al. [48] investigated effect of temperature and pressure in surface tension of polystyrene in supercritical CO_2 . Their results show that surface tension decreases for high temperature and pressure.

However, we notice that Goel and Beckman [13] needed a low surface tension at low temperature to fit to CNT and their increased cell density at low temperature. Experimentally, Leung et. al. [28] observed high cell density at low temperature and found the surface tension has a minimal effect. Amon and Deson [1] also found surface tension to be unimportant to the foaming process in their theoretical work. We observed that the driving force to make the bubble, i.e., pressure difference in CNT, is a more dominant factor than the surface tension.

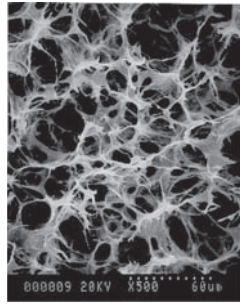
Aside from cell density and cell size, foam properties are also determined by foam volume expansion ratio or open-cell content. There are efforts to know the expansion behavior. [40, 66, 47, 41] The experimental results showed the volume expansion ratio increased with decreased temperature. Fig. 1.3(a) shows Park et. al.'s result [47]. As for the processing condition, except temperature or solvent density mentioned above, there are also works to see effects of pressure dropping rate on foam properties. [45, 29, 25]. Leung and Guo [29] investigated cell density by using polycarbonate foams blown with supercritical CO_2 . Their results show high cell densities at higher pressure dropping rate. Fig. 1.3(b) shows their result.

We compared qualitatively our theoretical results, i.e., foam morphology dependence on processing conditions, with these experimental results.



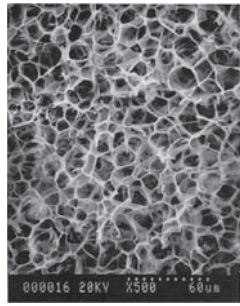
(a)

$T_c = 170^\circ\text{C}$



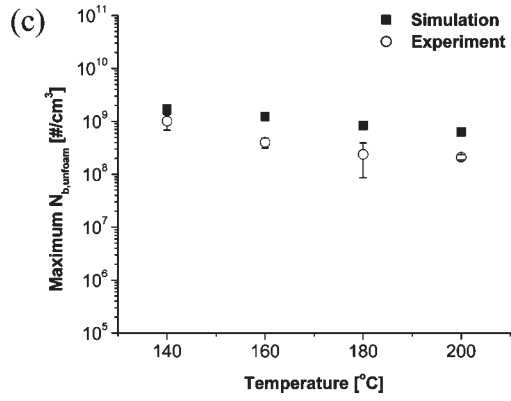
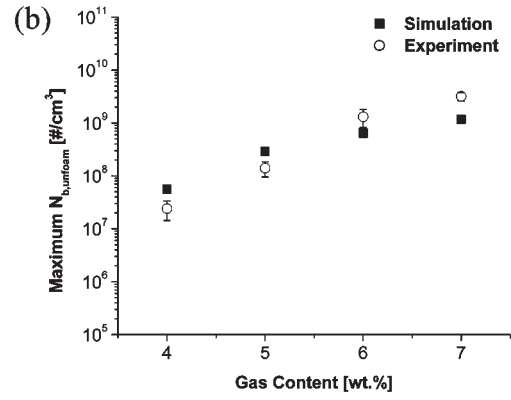
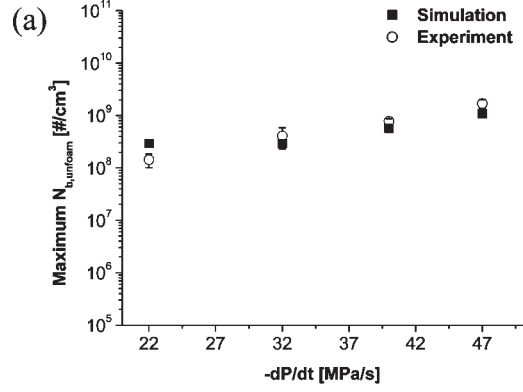
(b)

$T_c = 150^\circ\text{C}$



(c)

$T_c = 120^\circ\text{C}$



(a)

(b)

Figure 1.4: (a) Processing temperature effect on foam structure. We can see small size bubbles (high cell density) at low temperature. From [47] (b) Effects of (a) pressure drop rate ($-dP/dt$), (b) solvent density, (c) temperature. From [29]

1.3 Outline of Thesis

In chapter 2, we introduce basic theories used in this thesis.

In chapter 3, for nano-sized bubbles, since the curvature of the bubble surface is comparable to the size of the polymer molecule, we represent bubble surface as a curved surface. We investigate the effect of curvature on the nucleation energy of a bubble, and our results show that a nano-sized polymeric bubble has a much smaller nucleation energy than CNT predicts. We also investigate the microscopic origins of the failure of CNT for nanopolymeric foams.

In chapter 4, by using SCFT and our model, we calculate direct predictions for the maximal possible cell densities as a function of radius of a bubble without calculating the nucleation energy and nucleation rate, as is required for CNT. With the results of cell density at different temperatures and solvent densities, we investigate the effects of temperature and solvent density on cell density. We present result which contradict CNT prediction, and it is found that for different temperatures, the volume free energy density is a more dominant factor than surface tension for both cell density and cell size.

In chapter 5, we drop the incompressible limitation used in chapter 3 and chapter 4. By using a hole-based SCFT developed by Hong and Noolandi, we calculate system pressure as a function of system volume. For the calculations, we assume our system has an optimal pressure of the best foam in which the bulk phase is reached inside the bubble. Then, we calculate the maximal cell density and polymer density outside a bubble as well as system pressure as a function of system volume. We investigate qualitatively the system expansion ratio and open cell content for different processing conditions such as different temperatures, solvent densities, and the pressure drop rate.

In chapter 6, conclusions and discussion are presented.

Chapter 2

Basic Theory

2.1 Classical Nucleation Theory

According to the CNT [44], the nucleation of a bubble from a supersaturated liquid involves two energy changes: one is negative energy change due to the inside bubble bulk phase change which is a driving force of the nucleation of a bubble, and another is positive energy change from the interface formation which is a required energy change to form interface between old and new phase. If the radius of bubble is R , then the total energy change after the nucleation of a bubble of radius R is written as

$$\Delta F(R) = \frac{4\pi}{3} R^3 \Delta p + 4\pi R^2 \gamma, \quad (2.1)$$

where Δp is pressure difference between inside and outside bubble, i.e., free energy difference per unit volume due to the new bulk phase nucleation inside the bubble, and γ is the surface tension defined as the excess free energy per unit area required to form the interface inside and outside bubble. Thus, the sign of Δp is negative and the sign of γ is positive. Fig.(2.1) shows a schematic diagram of the CNT. In Fig.(2.1), there is a radius at which the total free energy change is maximum and which is defined as the critical radius. Bubble would be shrinking or growing depending on whether the bubble radius is smaller or bigger than this critical radius. This critical radius of a bubble is found out by taking the derivative

$$\frac{\partial \Delta F}{\partial R} = 0. \quad (2.2)$$

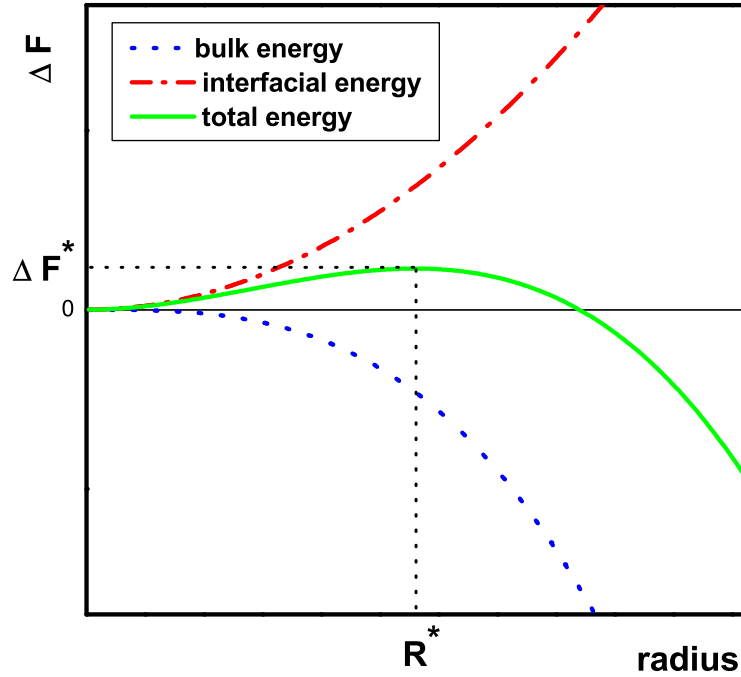


Figure 2.1: Plot of the nucleation barrier ΔF^* and critical radius R^*

The critical radius is then found to be

$$R^* = -\frac{2\gamma}{\Delta p} \quad (2.3)$$

Then, the nucleation barrier is defined as the total free energy at the critical radius, i.e., the bubble should overcome this nucleation barrier to grow. The nucleation barrier is simply found by substituting the critical radius in eq.(2.1)

$$\Delta F^* = \frac{16\pi}{3} \left(\frac{\gamma^3}{\Delta p^2} \right). \quad (2.4)$$

According to CNT, the steady-state nucleation rate has the form

$$J = J_0 \exp \left(-\frac{\Delta F^*}{kT} \right), \quad (2.5)$$

where J_0 is a dynamical prefactor that is related to the characteristic time scale for motion in the system, k is Boltzmann constant, and T is absolute temperature. Here we can see that the nucleation barrier is a very important factor in determining the nucleation rate. If nucleation barrier is small, then the nucleation rate is increased exponentially. However, in CNT there are several limitations to calculate the nucleation barrier of nano-polymer bubble.

First of all, CNT assumes both the inside and outside bubble phases are bulk phase no matter how much small the bubble size is. If the bubble size is nano-size, then the bubble might be all interface without a bulk phase in the interior of the bubble, i.e., bubble might never reach the bulk phase at the center of a bubble. Secondly, CNT assumes the surface is a sharp flat surface, but for small bubbles like nano-sized bubbles, the surface curvature is significant, so it is not proper to assume there is no curvature. The curvature effect on surface tension might be very significant. Thirdly, in CNT, they assume there is no thickness in interface assuming the interface be like step function. Due to these above CNT assumptions that are not suitable for nano-sized bubbles, CNT nucleation rate predictions might deviate significantly from real nucleation rates in nano-sized bubbles.

2.2 Self - Consistent Field Theory

We use Self - Consistent Field Theory(SCFT) to calculate the total free energy change before and after formation of a bubble. SCFT[35, 10] is an equilibrium statistical mechanical mean field theory. Oxtoby[43] pointed out that bubbles are stable as opposed to the grand canonical ensemble in canonical ensemble formalism where the free energies can be correctly calculated. Thus, SCFT is suitable to calculate free energy of inhomogeneous polymer system. We use constraint free, canonical ensemble in this thesis. The bubbles we study are stable against growth above the critical radius.

2.2.1 Modeling

Our system is a homopolymer + solvent system. We use a standard coarse-grained Gaussian string model for the polymer, so the polymer is described as a chain of segments whose

orientation is random and the distribution of a segment length is Gaussian distribution[34]. We model the solvent as a particle which has an excluded volume. For the interaction of molecules, we assume there are contact interactions between polymer segments, solvent molecules, and polymer segment and solvent molecule. Then, the Hamiltonian of our system is written as the polymer configuration energy which is like a segment stretching energy to treat polymer configurational entropy plus the interaction energy between molecules. Hamiltonian H is given by

$$H = \sum_{i=1}^{n_p} \frac{3}{2Na^2} \int_0^1 ds \left| \frac{d\mathbf{r}_\alpha(s)}{ds} \right|^2 + \chi \int \hat{\phi}_p(\mathbf{r}) \hat{\phi}_s(\mathbf{r}) d\mathbf{r}, \quad (2.6)$$

where a is a statistical segment length, $\mathbf{r}_\alpha(s)$ is a space curve of a polymer, χ is the Flory-Huggins parameter which is a segregation parameter defined by

$$\begin{aligned} \chi &= \tilde{\chi}_{ps} - \frac{1}{2}(\tilde{\chi}_{pp} + \tilde{\chi}_{ss}) \\ \tilde{\chi}_{ij} &= \frac{\rho_i \rho_j}{k_B T} \int V_{ij}(|\mathbf{r}|) d\mathbf{r}. \end{aligned} \quad (2.7)$$

$\hat{\phi}_p(\mathbf{r}), \hat{\phi}_s(\mathbf{r})$ are the concentration operator of polymer and solvent molecule at a given point \mathbf{r} and are defined as

$$\hat{\phi}_p(\mathbf{r}) = \frac{N}{\rho_p} \sum_{\alpha=1}^{n_p} \int_0^1 ds \delta(\mathbf{r} - \mathbf{r}_\alpha(s)) \quad (2.8)$$

$$\hat{\phi}_s(\mathbf{r}) = \frac{1}{\rho_s} \sum_{i=1}^{n_s} \delta(\mathbf{r} - \mathbf{r}_i), \quad (2.9)$$

where N is the degree of polymerization based on the polymer segment volume ρ_p^{-1} , and n_p, n_s are number of polymer molecules and solvent molecules respectively, and ρ_p^{-1}, ρ_s^{-1} are the volumes of one segment of polymer molecule and a solvent molecule, respectively. Then, with an incompressible system constraint, the partition function of our system is written

$$\begin{aligned} Z &= \frac{1}{n_p! n_s!} \int \prod_{\alpha=1}^{n_p} \tilde{D}\mathbf{r}_\alpha \int \prod_{i=1}^{n_s} d\mathbf{r}_i \delta(1 - \hat{\phi}_p(\mathbf{r}) - \hat{\phi}_s(\mathbf{r})) \\ &\times \exp\left(-\chi \rho_p \int \hat{\phi}_p(\mathbf{r}) \hat{\phi}_s(\mathbf{r}) d\mathbf{r}\right), \end{aligned} \quad (2.10)$$

where

$$\tilde{D}\mathbf{r}_\alpha \equiv D\mathbf{r}_\alpha \exp\left(\frac{-3}{2Na^2} \int_0^1 da \left| \frac{d\mathbf{r}_\alpha(s)}{ds} \right|^2\right) \quad (2.11)$$

, which is a functional integral of all possible configurations of a polymer.

2.2.2 Meanfield Theory and Density Functional Method

To transform the operators $\hat{\phi}_p$ and $\hat{\phi}_s$ to the field functions Φ_p and Φ_s one uses the δ functional integral representation,

$$\int D\Phi_p \delta[\Phi_p(\mathbf{r}) - \hat{\phi}_p(\mathbf{r})] F(\Phi_p(\mathbf{r})) = F(\hat{\phi}_p(\mathbf{r})) \quad (2.12)$$

$$\int D\Phi_s \delta[\Phi_s(\mathbf{r}) - \hat{\phi}_s(\mathbf{r})] F(\Phi_s(\mathbf{r})) = F(\hat{\phi}_s(\mathbf{r})) \quad (2.13)$$

$$\delta[\Phi_p(\mathbf{r}) - \hat{\phi}_p(\mathbf{r})] = \int_{-i\infty}^{+i\infty} DW_p \exp \left[\frac{\rho_p}{N} \int d\mathbf{r} W_p(\mathbf{r}) (\Phi_p(\mathbf{r}) - \hat{\phi}_p(\mathbf{r})) \right] \quad (2.14)$$

$$\delta[\Phi_s(\mathbf{r}) - \hat{\phi}_s(\mathbf{r})] = \int_{-i\infty}^{+i\infty} DW_s \exp \left[\rho_s \int d\mathbf{r} W_s(\mathbf{r}) (\Phi_s(\mathbf{r}) - \hat{\phi}_s(\mathbf{r})) \right] \quad (2.15)$$

By using above expressions, partition function Z is written

$$\begin{aligned} Z = & \frac{1}{n_p! n_s!} \int \prod_{\alpha=1}^{n_p} \tilde{D}\mathbf{r}_\alpha \int \prod_{i=1}^{n_s} d\mathbf{r}_i \int D\Phi_p D\Phi_s DW_p DW_s D\Xi \\ & \times \exp \left[\frac{\rho_p}{N} \int d\mathbf{r} W_p(\mathbf{r}) (\Phi_p(\mathbf{r}) - \hat{\phi}_p(\mathbf{r})) + \rho_s \int d\mathbf{r} W_s(\mathbf{r}) (\Phi_s(\mathbf{r}) - \hat{\phi}_s(\mathbf{r})) \right. \\ & \left. + \frac{\rho_p}{N} \int d\mathbf{r} (\Xi(\mathbf{r}) (1 - \Phi_p(\mathbf{r}) - \Phi_s(\mathbf{r})) - \chi N \Phi_p(\mathbf{r}) \Phi_s(\mathbf{r})) \right] \end{aligned} \quad (2.16)$$

Here, by using the definition of $\hat{\phi}_p(\mathbf{r})$ and $\hat{\phi}_s(\mathbf{r})$,

$$\frac{\rho_p}{N} \int d\mathbf{r} W_p(\mathbf{r}) \hat{\phi}_p(\mathbf{r}) - \rho_s \int d\mathbf{r} W_s(\mathbf{r}) \hat{\phi}_s(\mathbf{r}) = - \sum_{\alpha=1}^{n_p} \int ds W_p(\mathbf{r}_\alpha(s)) - \sum_{i=1}^{n_s} W_s(\mathbf{r}_i) \quad (2.17)$$

Now, the partition function is written with field functions

$$\begin{aligned} Z = & \frac{1}{n_p! n_s!} \int D\Phi_p D\Phi_s DW_p DW_s D\Xi Q_p^{n_p} Q_s^{n_s} \\ & \times \exp \left[\frac{\rho_p}{N} \int d\mathbf{r} (W_p(\mathbf{r}) \Phi_p(\mathbf{r}) + W_s(\mathbf{r}) \Phi_s(\mathbf{r}) \right. \\ & \left. + \Xi(\mathbf{r}) (1 - \Phi_p(\mathbf{r}) - \Phi_s(\mathbf{r})) - \chi N \Phi_p(\mathbf{r}) \Phi_s(\mathbf{r}) \right], \end{aligned} \quad (2.18)$$

where

$$Q_p \equiv \int \tilde{D}\mathbf{r}_\alpha e^{-\int_0^1 ds W_p(\mathbf{r}_\alpha(s))} \quad (2.19)$$

$$Q_s \equiv \int d\mathbf{r} e^{-\alpha W_s(\mathbf{r})} \quad (2.20)$$

which are the partition functions of a polymer and solvent molecule respectively based on subject to the fields ω_p and ω_s . α is the ratio of the volume of a solvent molecule to polymer molecule ($\alpha = \rho_p/(N\rho_s)$). Finally, we obtain the partition function

$$Z = \frac{1}{n_p!n_s!} \int D\Phi_p D\Phi_s DW_p DW_s D\Xi \exp\left(-\frac{F}{k_B T}\right), \quad (2.21)$$

where

$$\begin{aligned} \frac{F}{k_B T} = & n_p \ln Q_p - n_s \ln Q_s \\ & - \frac{\rho_p}{N} \int d\mathbf{r} [\Xi(\mathbf{r})(1 - \Phi_p(\mathbf{r}) - \Phi_s(\mathbf{r})) - \chi N \Phi_p(\mathbf{r}) \Phi_s(\mathbf{r}) \\ & + W_p(\mathbf{r}) \Phi_p(\mathbf{r}) + W_s(\mathbf{r}) \Phi_s(\mathbf{r})]. \end{aligned} \quad (2.22)$$

Now, though we got the partition function expression of our system, we can not calculate the functional integrals. Thus, in SCFT one approximates this integral by the extremum of the integrand. By the Saddle-Point method[7], we take the minimum Helmholtz free energy $F = -k_B T \ln Z$ as our inhomogeneous system free energy. Thus, our inhomogeneous free energy is given by $F[\varphi_p, \varphi_s, \omega_p, \omega_s, \xi]$, where $\varphi_p, \varphi_s, \omega_p, \omega_s, \xi$ are the functions for which F has the minimum. From the minimum condition - the functional derivative of each variable is zero - we get following self consistent equations.

$$\omega_p(\mathbf{r}) = \chi N \varphi_s(\mathbf{r}) + \xi(\mathbf{r}) \quad (2.23)$$

$$\omega_s(\mathbf{r}) = \chi N \varphi_p(\mathbf{r}) + \xi(\mathbf{r}) \quad (2.24)$$

$$\varphi_p(\mathbf{r}) + \varphi_s(\mathbf{r}) = 1 \quad (2.25)$$

$$\varphi_p(\mathbf{r}) = -\frac{\phi_p V}{Q_p} \frac{\delta Q_p}{\delta \omega_p(\mathbf{r})} \quad (2.26)$$

$$\varphi_s(\mathbf{r}) = \frac{\phi_s V}{Q_s} e^{-\alpha \omega_s(\mathbf{r})} \quad (2.27)$$

By solving these equations self-consistently, the inhomogeneous free energy is obtained. At this point, we can use an alternative expression of the partition function of a polymer molecule, i.e.,

$$Q_p = \int d\mathbf{r} q(\mathbf{r}, 1), \quad (2.28)$$

where the end-segment distribution function $q(\vec{r}, 1)$ is given by

$$q(\mathbf{r}, 1) = \int D\mathbf{r}_\alpha P[\mathbf{r}_\alpha; 0, 1] \delta(\mathbf{r} - \mathbf{r}_\alpha(1)) \exp\left[-\int_0^1 \omega_p(\mathbf{r}_\alpha(s)) ds\right] \quad (2.29)$$

which is the functional integral over all configuration with the functionals

$$P[\mathbf{r}_\alpha; 0, 1] \propto \exp\left\{-\frac{3}{2Na^2} \int_0^1 ds \left|\frac{d}{ds} \mathbf{r}_\alpha(s)\right|^2\right\} \quad (2.30)$$

Then, with the identity [16],

$$\left(\frac{3}{2\pi Na^2 \Delta s}\right)^{\frac{3}{2}} \exp\left[-\frac{3}{2Na^2 \Delta s} |\mathbf{r} - \mathbf{s}|^2\right] = \exp\left(-\frac{1}{6} Na^2 \Delta s \nabla_r^2\right) \delta(\mathbf{r} - \mathbf{s}), \quad (2.31)$$

this end-segment distribution function satisfies the modified diffusion equation.

$$\frac{\partial q(\mathbf{r}, s)}{\partial s} = \frac{1}{6} Na^2 \nabla^2 q(\mathbf{r}, s) - \omega_p(\mathbf{r}) q(\mathbf{r}, s) \quad (2.32)$$

By solving this modified diffusion equation, the $\varphi_p(\mathbf{r})$ is given by

$$\varphi_p(\mathbf{r}) = \frac{\phi_p V}{Q_p} \int_0^1 q(\mathbf{r}, s) ds \quad (2.33)$$

From those self-consistent equations, once we obtain $\varphi_p(\mathbf{r}), \varphi_s(\mathbf{r}), \omega_p(\mathbf{r}), \omega_s(\mathbf{r}), \xi(\mathbf{r})$, the dimensionless inhomogeneous system free energy is given by

$$\begin{aligned} \frac{NF}{\rho_p k_B T V} &= -\phi_p \ln\left(\frac{Q_p}{V\phi_p}\right) - \frac{\phi_s}{\alpha} \ln\left(\frac{Q_s}{V\phi_s}\right) \\ &\quad - \frac{1}{V} \int d\mathbf{r} [\xi(\mathbf{r})(1 - \varphi_p(\mathbf{r}) - \varphi_s(\mathbf{r})) - \chi N \varphi_p(\mathbf{r}) \varphi_s(\mathbf{r}) \\ &\quad + \omega_p(\mathbf{r}) \varphi_p(\mathbf{r}) + \omega_s(\mathbf{r}) \varphi_s(\mathbf{r})], \end{aligned} \quad (2.34)$$

where

$$Q_p = \int d\mathbf{r} q(\mathbf{r}, 1) \quad (2.35)$$

$$Q_s \equiv \int d\mathbf{r} e^{-\alpha\omega_s(\mathbf{r})}, \quad (2.36)$$

ϕ_s and ϕ_p are the overall volume fractions of solvent and polymer, and $\varphi_s(\mathbf{r})$ and $\varphi_p(\mathbf{r})$ are the local volume fractions of solvent and polymer, respectively. $\omega_p(\mathbf{r})$ and $\omega_s(\mathbf{r})$ are the mean fields felt by polymer and solvent at position \mathbf{r} .

This inhomogeneous free energy expression becomes to the Flory-Huggins homogeneous free energy if $\omega_p(\mathbf{r})$ and $\omega_s(\mathbf{r})$ are constant, i.e.,

$$\frac{NF}{\rho_p k_B TV} = \phi_p \ln \phi_p + \frac{\phi_s}{\alpha} \ln \phi_s + \chi N \varphi_p(\mathbf{r}) \varphi_s(\mathbf{r}) \quad (2.37)$$

2.2.3 Numerical Method

Equations (2.23) - (2.27) are self-consistently solved numerically in real space. First, we guess the fields $\omega_p(\mathbf{r})$ and $\omega_s(\mathbf{r})$, and with these we solve the modified diffusion equation (2.32). Then we compute the local volume fraction $\varphi_p(\mathbf{r})$ from eq.(2.33) and $\varphi_s(\mathbf{r})$ from eq.(2.25). Also from eq.(2.23) and eq.(2.24) we get

$$\xi(\mathbf{r}) = \frac{1}{2}(\omega_p(\mathbf{r}) + \omega_s(\mathbf{r})) + \chi N \quad (2.38)$$

With the volume fraction values $\varphi_p(\mathbf{r})$, $\varphi_s(\mathbf{r})$, and pressure field $\xi(\mathbf{r})$, we get new fields $\omega_p(\mathbf{r})$ and $\omega_s(\mathbf{r})$. We iterate this process until the new fields and old fields differ 10^{-8} . Figure (2.2) shows the procedure.

To solve the modified diffusion eq. we used a Crank-Nicolson algorithm with reflecting boundary conditions.

2.3 Theory for a Compressible System

2.3.1 Compressible Lattice Liquid Theory

To deal with a compressible system, we used a compressible field theory that Hong and Noolandi developed to take into account free volume effects[18]. Hong and Noolandi modified their formalism for an incompressible multicomponent system simply by taking one of the small-molecule components to be vacancies. Thus, we used exactly same formula

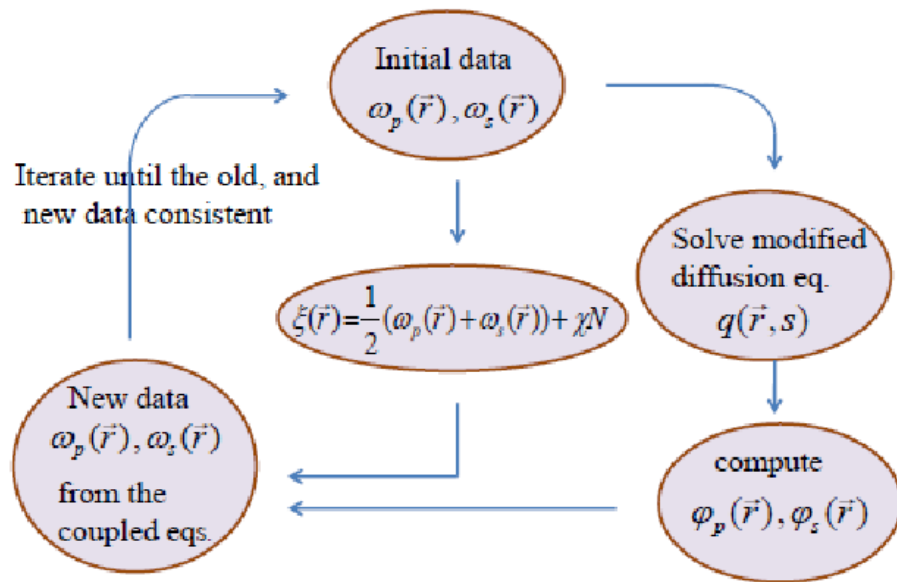


Figure 2.2: numerical method of solving self-consistent eqs. in real space

of the inhomogeneous free energy of the incompressible system for the inhomogeneous free energy of the compressible system, but our compressible system is homopolymer + solvent + holes.

With constraint of $\phi_p + \phi_s + \phi_h = 1$ instead of $\phi_p + \phi_s = 1$ of the incompressible system, the dimensionless inhomogeneous free energy density functional of our compressible system is given by

$$\begin{aligned} \frac{NF}{\rho_p k_B T V} = & -\phi_p \ln \left(\frac{Q_p}{V \phi_p} \right) - \frac{\phi_s}{\alpha_s} \ln \left(\frac{Q_s}{V \phi_s} \right) - \frac{\phi_h}{\alpha_h} \ln \left(\frac{Q_h}{V \phi_h} \right) \\ & + \frac{1}{V} \int d\mathbf{r} \left\{ \chi_{ps} N \varphi_p(\mathbf{r}) \varphi_s(\mathbf{r}) + \frac{1}{2} \chi_{pp} N \varphi_p(\mathbf{r}) \varphi_p(\mathbf{r}) \right. \\ & + \frac{1}{2} \chi_{ss} N \varphi_s(\mathbf{r}) \varphi_s(\mathbf{r}) - \omega_p(\mathbf{r}) \varphi_p(\mathbf{r}) - \omega_s(\mathbf{r}) \varphi_s(\mathbf{r}) \\ & \left. - \omega_h(\mathbf{r}) \varphi_h(\mathbf{r}) - \xi(\mathbf{r}) [1 - \varphi_p(\mathbf{r}) - \varphi_s(\mathbf{r}) - \varphi_h(\mathbf{r})] \right\} \end{aligned} \quad (2.39)$$

with

$$Q_p \equiv \int d\vec{r} q(\mathbf{r}, 1) \quad (2.40)$$

$$Q_s \equiv \int d\mathbf{r} e^{-\alpha_s \omega_s(\mathbf{r})} \quad (2.41)$$

$$Q_h \equiv \int d\mathbf{r} e^{-\alpha_h \omega_h(\mathbf{r})}, \quad (2.42)$$

where the all parameters meanings are the same as in the previous section except the subscription h means hole. From the minimum condition of the Saddle - Point method, the variation of the above eq.(2.36) with respect to the functions $\phi_s(\vec{r})$, $\phi_p(\mathbf{r})$, $\phi_h(\mathbf{r})$, $\omega_s(\mathbf{r})$, $\omega_p(\mathbf{r})$, $\omega_h(\mathbf{r})$, and $\xi(\mathbf{r})$ results in a set of equations which are solved self-consistently.

The equations are

$$\omega_s(\mathbf{r}) = \chi_{ps} N \varphi_p(\mathbf{r}) + \chi_{ss} N \varphi_s(\mathbf{r}) + \xi(\mathbf{r}) \quad (2.43)$$

$$\omega_p(\mathbf{r}) = \chi_{ps} N \varphi_p(\mathbf{r}) + \chi_{pp} N \varphi_p(\mathbf{r}) + \xi(\mathbf{r}) \quad (2.44)$$

$$\omega_h(\mathbf{r}) = \xi(\mathbf{r}) \quad (2.45)$$

$$\varphi_s(\mathbf{r}) + \varphi_p(\mathbf{r}) + \varphi_h(\mathbf{r}) = 1 \quad (2.46)$$

$$\varphi_s(\mathbf{r}) = \frac{\phi_s V}{Q_s} e^{-\alpha_s \omega_s(\mathbf{r})} \quad (2.47)$$

$$\varphi_h(\mathbf{r}) = \frac{\phi_h V}{Q_h} e^{-\alpha_h \omega_h(\mathbf{r})} \quad (2.48)$$

$$\varphi_p(\mathbf{r}) = \frac{\phi_p V}{Q_p} \int_0^1 ds q(\mathbf{r}, s) q(\mathbf{r}, 1-s) \quad (2.49)$$

We solved these eqs. by using the numerical method described in section 2.2.3.

2.3.2 Equation of State

For a homogeneous system, the dimensionless free energy density of our compressible system is given by

$$\begin{aligned} \frac{NF}{\rho_p k_B T V} = & \phi_p \ln \phi_p + \frac{\phi_s}{\alpha_s} \ln \phi_s + \frac{\phi_h}{\alpha_h} \ln \phi_h \\ & + \chi_{ps} \phi_p \phi_s + \frac{1}{2} \chi_{pp} N \phi_p \phi_p + \frac{1}{2} \chi_{ss} N \phi_s \phi_s \end{aligned} \quad (2.50)$$

To make contact with the equation of state theory of Sanchez and Lacombe [51, 23], we define

$$\chi_{pp} = -\frac{2\epsilon_{pp}^*}{k_B T} \quad (2.51)$$

$$\chi_{ss} = -\frac{2\epsilon_{ss}^*}{k_B T} \quad (2.52)$$

$$\chi_{ps} = -\frac{2\epsilon_{ps}^*}{k_B T} \quad (2.53)$$

$$\phi_p = \frac{V_p^*}{V} \quad (2.54)$$

$$\phi_s = \frac{V_s^*}{V} \quad (2.55)$$

$$\phi_h = 1 - \left(\frac{V_p^* + V_s^*}{V} \right) = 1 - \frac{V^*}{V}, \quad (2.56)$$

where V_p^* and V_s^* are close-packed volumes of polymer and solvent molecules in the system, respectively.

Then, the Helmholtz free energy is written

$$\begin{aligned} F = & v_p^{*-1} \left\{ \frac{k_B T V_p^*}{N} \ln \left(\frac{V_p^*}{V} \right) + \frac{1}{\alpha_s} \frac{k_B T V_s^*}{N} \ln \left(\frac{V_s^*}{V} \right) + \frac{1}{\alpha_h} \frac{k_B T (V - V^*)}{N} \ln \left(1 - \frac{V^*}{V} \right) \right. \\ & \left. - \epsilon_{pp}^* \frac{V_p^* V_p^*}{V} - \epsilon_{ss}^* \frac{V_s^* V_s^*}{V} - 2\epsilon_{ps}^* \frac{V_p^* V_s^*}{V} \right\}, \end{aligned} \quad (2.57)$$

and the pressure of the homogeneous system is

$$\begin{aligned}
P &= - \left(\frac{\partial F}{\partial V} \right)_{T, N_p, N_s} \\
&= -v_p^{*-1} \left\{ -k_B T \left(\frac{V_p^*}{NV} + \frac{V_s^*}{\alpha_s NV} \right) + \frac{k_B T}{\alpha_h N} \ln \left(1 - \frac{V^*}{V} \right) + \frac{k_B T}{\alpha_h N} \left(\frac{V^*}{V} \right) \right. \\
&\quad \left. + \epsilon_{pp}^* \frac{V_p^{*2}}{V^2} - \epsilon_{ss}^* \frac{V_s^{*2}}{V^2} - 2\epsilon_{ps}^* \frac{V_p^* V_s^*}{V^2} \right\}
\end{aligned} \tag{2.58}$$

with

$$\alpha_s N = \frac{v_s^*}{v_p^*} = 1 \tag{2.59}$$

$$\alpha_h N = \frac{v_h^*}{v_p^*} = 1, \tag{2.60}$$

where v_p^* , v_s^* , and v_h^* are the close-packed volumes of one segment of polymer, one solvent molecule, and the volume of a hole, respectively.

If we set $\alpha_s N = \alpha_h N = 1$, then

$$\begin{aligned}
P &= -v_p^{*-1} \left\{ k_B T \left[- \left(\frac{V_p^*}{NV} + \frac{V_s^*}{V} \right) + \ln \left(1 - \frac{V^*}{V} \right) + \frac{V^*}{V} \right] \right. \\
&\quad \left. + \epsilon_{pp}^* \frac{V_p^{*2}}{V^2} - \epsilon_{ss}^* \frac{V_s^{*2}}{V^2} - 2\epsilon_{ps}^* \frac{V_p^* V_s^*}{V^2} \right\},
\end{aligned} \tag{2.61}$$

which is identical with the equation of state obtained by Lacombe and Sanchez.

We set $\alpha_s N = \alpha_h N = 1$ in our compressible system.

Chapter 3

Microscopic Origin of the Failure of Classical Nucleation Theory

Classical Nucleation Theory (CNT) [62, 70, 3] is often used to predict bubble nucleation rates in polymer foaming [28, 13], but due to several assumptions of CNT - sharp flat surface and bulk phase inside a bubble - CNT has limitations when calculating the nucleation rate of nano-cellular polymer foams. Since the size of the nano-cellular bubble is comparable with the polymer size, the polymer must “see” the interface curvature and the interface curvature must have effects on the nucleation of the nano-cellular bubble. Moreover, the nano bubble might not be in the bulk phase inside at all due to its small size.

To investigate the effect of curvature on bubble nucleation, we used both flat and curved bubble surfaces, and to compare the two cases, we used the same model for both. To estimate the nucleation rate based on CNT, we calculated the nucleation barrier by calculating the free energy of the inhomogeneous system with Self-Consistent Field Theory (SCFT). One example calculation presented in this chapter shows that a curved surface has several orders of magnitude smaller homogenous nucleation rate than that of a flat surface case predicted by CNT. We observed that surface tension and volume free energy density, which corresponds to the pressure difference between the inside and outside of a bubble in CNT, are functions of the radius of a bubble in contrast to the constant surface tension and volume free energy density of the flat surface.

Accordingly, we see that the origin of the significant deviation of nucleation rate from the prediction of CNT is the decreasing surface tension and the increasing (negative) volume free energy density for smaller bubbles. We investigated the microscopic origin of the failure of the CNT by calculating thermodynamic components of the surface tension and the volume free energy density. It turns out that the main cause of the deviation is the

sharper curvature at smaller bubble radius which allows more available polymer configurations with lower internal energy. The collapse of the bulk region inside bubble for small bubbles near the critical radius leading to lower internal energy is a secondary cause of the decreasing surface tension for smaller bubbles. In addition, the same mechanisms, namely the increasing internal energy causing increasing entropy for smaller bubbles is also the microscopic origin of the increase of the (negative) volume free energy density.

In the first section of this chapter, we summarize how we calculate the nucleation barrier, i.e., how surface tension and volume free energy density are defined and calculated in our model. In section 2, we present an example calculation comparing the flat surface case and the curved surface case. In section 3, we discuss the microscopic origins of the CNT failure, and conclusions and discussions are presented in the final section.

3.1 Theory

In Classical Nucleation Theory, the homogeneous nucleation rate is given by

$$J = J_0 \exp(-\Delta F^*/k_B T), \quad (3.1)$$

where J_0 is a prefactor associated with the characteristic time scales of motion of the system, and ΔF^* is the free energy necessary to form a critical radius bubble R^* smaller than which the bubble shrinks and disappears and larger than which the bubble grows [43]. According to CNT, the free energy ΔF necessary to form a typical bubble of an arbitrary radius R is

$$\Delta F(R) = \frac{4\pi}{3} R^3 \Delta F_V + 4\pi R^2 \gamma, \quad (3.2)$$

where γ is surface tension defined as the excess free energy per unit area required to form interface, and ΔF_V is free energy change per bubble volume due to the new bulk phase formation of a bubble. In this chapter we call it the volume free energy density which corresponds to Δp in the CNT expression, and the sign of ΔF_V is minus.

Fig. 3.1 shows the structures we used to calculate the surface tension and volume free energy density. Fig. 3.1 (a) is the profile of the initial homogeneous system, (b) is the profile of the bulk phase separated homogeneous system, which would be formed if there is no interface - the system consists of two bulk homogeneous systems with volume fraction values on either side of the interface of the final inhomogeneous system, and (c) is the

profile of final inhomogeneous system with the interface. One can notice that (a) and (c) are real systems, while (b) is a virtual system which would be formed if there is no interface.

To calculate the excess free energy density of the interface, we subtract the free energy density of panel (b) from the free energy density of panel (c), i.e., we subtract the free energy density of the bulk phase separated system \tilde{F}_s from the inhomogeneous free energy density \tilde{F} , i.e.,

$$\tilde{F}_{ex} = \tilde{F} - \tilde{F}_s, \quad (3.3)$$

where tildes mean dimensionless quantities.

The dimensionless inhomogeneous system free energy \tilde{F} is given by

$$\begin{aligned} \tilde{F} &\equiv \frac{NF}{\rho_0 k_B T V} \\ &= (1 - \phi_s) \ln \left(\frac{Q_p}{V(1 - \phi_s)} \right) - \frac{\phi_s}{\alpha} \ln \left(\frac{Q_s \alpha}{V \phi_s} \right) \\ &\quad - \frac{1}{V} \int d\mathbf{r} \left\{ \chi N \varphi_p(\mathbf{r}) \varphi_s(\mathbf{r}) - \omega_p(\mathbf{r}) \varphi_p(\mathbf{r}) - \omega_s(\mathbf{r}) \varphi_s(\mathbf{r}) \right\}, \end{aligned} \quad (3.4)$$

where $\varphi_p(\mathbf{r})$ and $\varphi_s(\mathbf{r})$ are the local volume fractions of polymer and solvent, and ϕ_s and ϕ_p are the global volume fraction values, i.e., volume fraction values of the initial homogeneous system. Q_p and Q_s are single molecule partition functions of polymer and solvent, respectively. The ratio of volume of a solvent molecule to a polymer molecule is denoted by alpha with the volume of one polymer segment being ρ_0^{-1} and the degree of polymerization being N . The Flory-Huggins parameter χ is the segregation parameter between polymer and solvent, and $\omega_p(\mathbf{r})$ and $\omega_s(\mathbf{r})$ are the mean fields on polymer and solvent at position \mathbf{r} by surrounding molecules.

The free energy density of the bulk phase separated system, $\tilde{\mathcal{F}}_s$ is given by

$$\tilde{\mathcal{F}}_s = \tilde{\mathcal{F}}_h^{(1)} \frac{V_1}{V} + \tilde{\mathcal{F}}_h^{(2)} \frac{V_2}{V}, \quad (3.5)$$

where $\tilde{\mathcal{F}}_h^{(1)}$ and $\tilde{\mathcal{F}}_h^{(2)}$ are the bulk homogeneous free energy densities on either side of the interface. To calculate the energy density of the bulk homogeneous system we used the dimensionless homogeneous free energy density eq. (3.6) which is derived from Flory-Huggins theory.

$$\tilde{\mathcal{F}}_h^{(i)} = (1 - \phi_s^{(i)}) \ln(1 - \phi_s^{(i)}) + \frac{\phi_s^{(i)}}{\alpha} \ln \left(\frac{\phi_s^{(i)}}{\alpha} \right) + \chi N (1 - \phi_s^{(i)}) \phi_s^{(i)}, \quad (3.6)$$

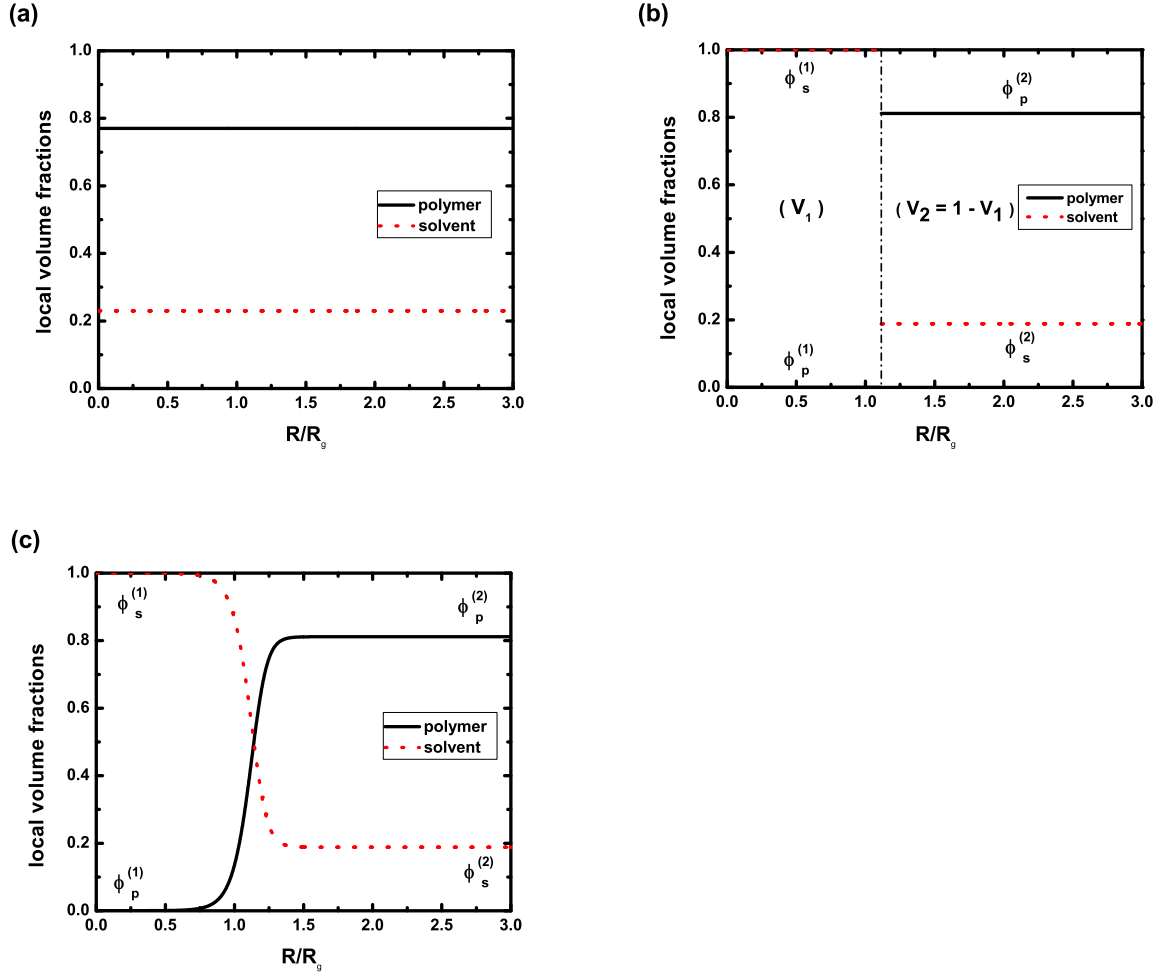


Figure 3.1: (a) Profile of the initial homogeneous system which has initial global volume fraction values. (b) Profile of the bulk phase separated homogeneous system which would be formed if there was no interface. Each bulk system has volume fraction values on either side of interface of the inhomogeneous system. Each bulk system volume V_1 and V_2 are determined by conservation of molecules. (c) Profile of the final inhomogeneous system after formation of a bubble, i.e., after formation of interface

where $\phi_s^{(i)}$, $i = 1, 2$, are solvent volume fraction values on either side of interface that would be used to get $\tilde{F}_h^{(1)}$ and $\tilde{F}_h^{(2)}$ respectively. V_1 and V_2 are the volumes of the homogeneous phase separated regions given by

$$V_1 + V_2 = V \quad (3.7)$$

$$\frac{V_1}{V} = \frac{\phi_s^{(2)} - \phi_s}{\phi_s^{(2)} - \phi_s^{(1)}}, \quad (3.8)$$

which is derived by the conservation of total volume of solvent. Dividing the excess free energy by interfacial area A , the dimensionless surface tension γ is

$$\tilde{\gamma} \equiv \frac{\tilde{F}_{ex}}{A} = \tilde{F}_{ex} \left(\frac{R_g^2}{4\pi R^2} \right), \quad (3.9)$$

where R is the bubble radius and R_g is the radius of gyration of a polymer. R_g is the unit of length used in this thesis.

To calculate the $\Delta F(R)$ in eq.(3.2), we need to know the volume free energy density ΔF_V which corresponds to Δp in CNT. Δp in CNT is defined as the energy change due to the phase transition of bulk inside the bubble divided by the bubble volume, which has a negative sign, i.e., the driving force of the bubble formation. Similarly, our ΔF_V in eq.(3.2) is found by subtracting the homogeneous system energy from the bulk phase separated homogeneous system energy and dividing by the bubble volume. The dimensionless volume free energy density ΔF_V is given by

$$\Delta F_V \equiv \frac{V}{V_1} (\tilde{F}_s - \tilde{F}_h), \quad (3.10)$$

where \tilde{F}_s is the free energy density of Fig.(3.1) panel(b) and \tilde{F}_h is the free energy density of Fig.(3.1) panel(a), V and V_1 are the volumes of the system and the bubble respectively. We define volume V_1 as the bubble volume[21], because this definition gives the same definition of the bubble radius as CNT. The prefactor $\frac{V}{V_1}$ is given by eq.(3.8).

The dimensionless free energy $\widetilde{\Delta F}(R)$ necessary to form a bubble of an arbitrary radius R is given by

$$\widetilde{\Delta F}(R) = 4\pi \left(\frac{R}{R_g} \right)^2 \tilde{\gamma}(R) + \frac{4\pi}{3} \left(\frac{R}{R_g} \right)^3 \Delta F_V(R), \quad (3.11)$$

where R is radius of the bubble, i.e., radius of volume V_1 .

Alternatively, for the curved surface, we can calculate the $\widetilde{\Delta F}(R)$ directly from SCFT. It is given by

$$\Delta \tilde{F}(R) = \left(\frac{V(R)}{R_g^3} \right) (\tilde{F}(R) - \tilde{F}_h(R)) \quad (3.12)$$

We are now ready to calculate the free energy change as a function of the bubble radius R . One should notice that the box volume is increasing as the bubble is growing, but we fix the global volume fraction values of the box. The global volume fraction values of all boxes of the bubbles need to be the same as the global volume fraction values of the initial homogeneous system, because the bubbles we make have the same initial homogeneous system. Consequently our bubble is a representative bubble of our macroscopic system - in our macroscopic system, there must be many sizes of bubbles growing and shrinking, but we can imagine one size of bubble as a representative bubble which fills in our macroscopic system, because the global solvent density of the system is the same as the global solvent density of the macroscopic system.

3.2 Surface Tension, Volume Free Energy Density and Nucleation Barrier in a Curved Surface and a Flat Surface

We examined systems with $\alpha = 0.01$, χN ranging from 120 to 160 and ϕ_s ranging from 0.2 to 0.33 which is the nucleation and growth region. In this chapter, we present results of one example case of $\chi N = 140$ and $\phi_s = 0.23$. Fig.(3.2) shows the homogeneous free energy as a function of solvent density. One can see that our system would be phase separated into $\phi_s = 1$ (inside bubble) and $\phi_s = 0.16465$ (outside bubble) in equilibrium.

Fig.(3.3) and Fig.(3.4) show local volume fractions of three different sizes of bubble with flat and curved surfaces, respectively. In the flat surface case, as we expected, Fig.(3.3) shows all the solvent volume fraction values outside the bubble are the same with the expected value in Fig. (3.2) irrespective of bubble size. On the contrary, Fig.(3.4) shows the solvent volume fraction values outside the bubble are changing depending on bubble size, and we observe that for a smaller bubble, the solvent volume fraction value is more deviated from the equilibrium solvent volume fraction value. Therefore, we can expect that there must be a curvature effect in the formation of a curved surface bubble.

By using eqs.(3.8) (3.9) (3.10), we calculated the surface tension $\tilde{\gamma}$ and the volume free energy $\widetilde{\Delta F}_V$ of flat and curved surface cases. For the flat surface case, we get a constant

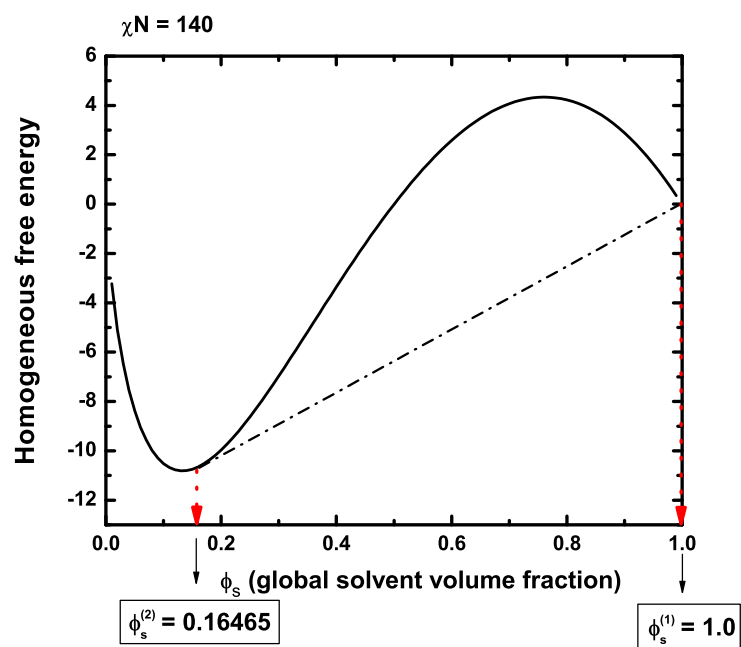


Figure 3.2: Homogeneous free energy versus global solvent volume fraction at $\chi N = 140$

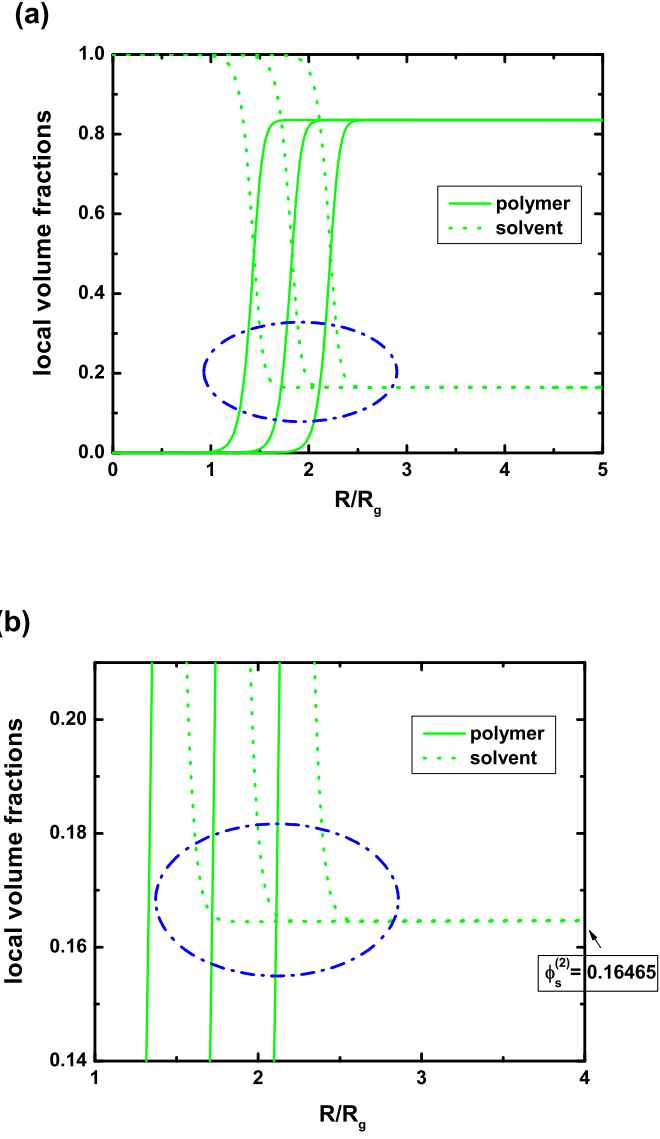


Figure 3.3: (a) Profiles of local volume fractions of three different sizes of bubble in the flat surface case. (b) In this blow up graph, we can see that at the outside of a bubble, three different sizes of bubble have the same solvent volume fraction value, which is the equilibrium value.

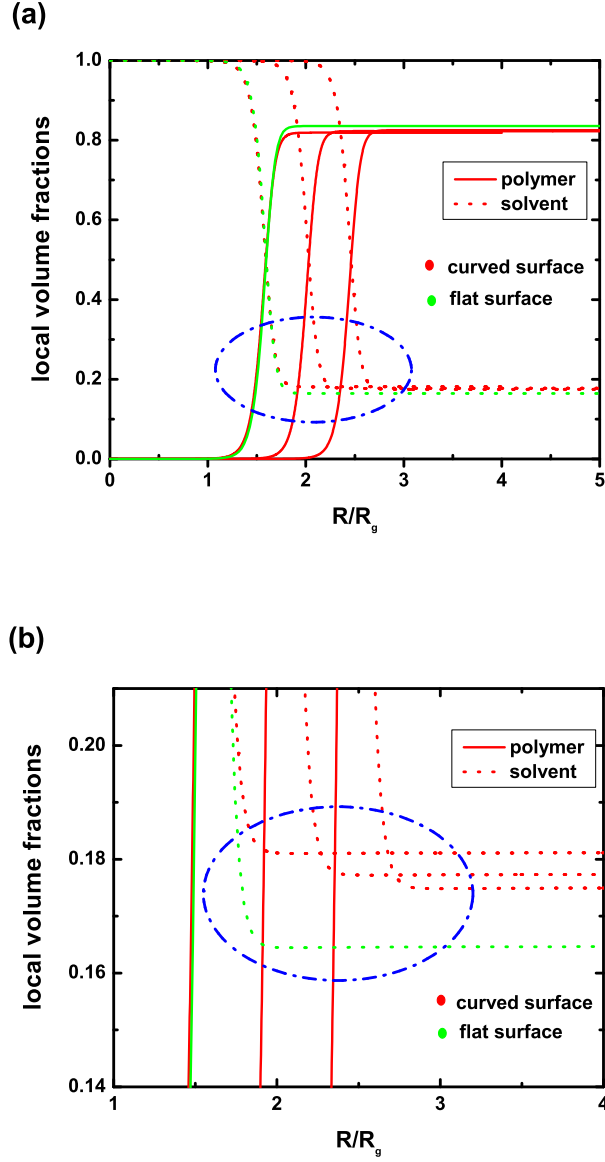


Figure 3.4: (a) Profiles of local volume fractions of three different sizes of bubble in the curved surface case and one profile of a flat surface. (b) In this blow up graph, we can see that in curved surface, three different sizes of bubble have different solvent volume fraction values at the outside of a bubble. Compared to the flat surface, in curved surface, smaller bubbles have more deviated volume fraction values from the equilibrium solvent volume fraction value.

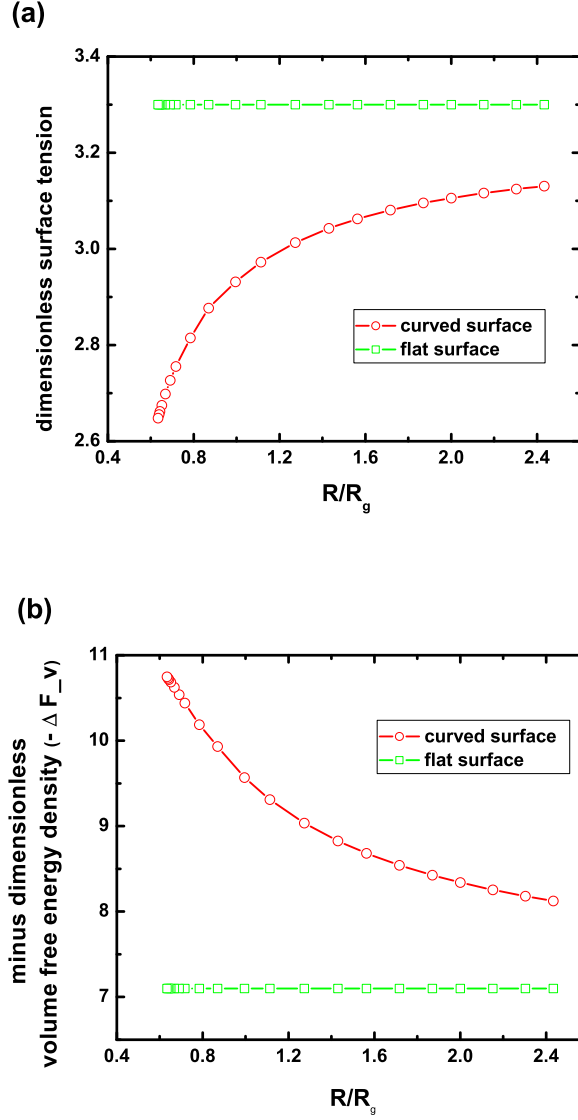


Figure 3.5: (a) Surface tension values versus radius of a bubble. For curved surfaces, surface tension is decreasing for the smaller bubble in contrast to the constant value of surface tension for the flat surface. (b) The negative of volume free energy density ($-\Delta F_V$) versus radius of a bubble. As the sign of ΔF_V is minus, the sign of $-\Delta F_V$ is positive. The negative volume free energy density is increasing for smaller bubbles in contrast to the constant value of volume free energy density for the flat surface.

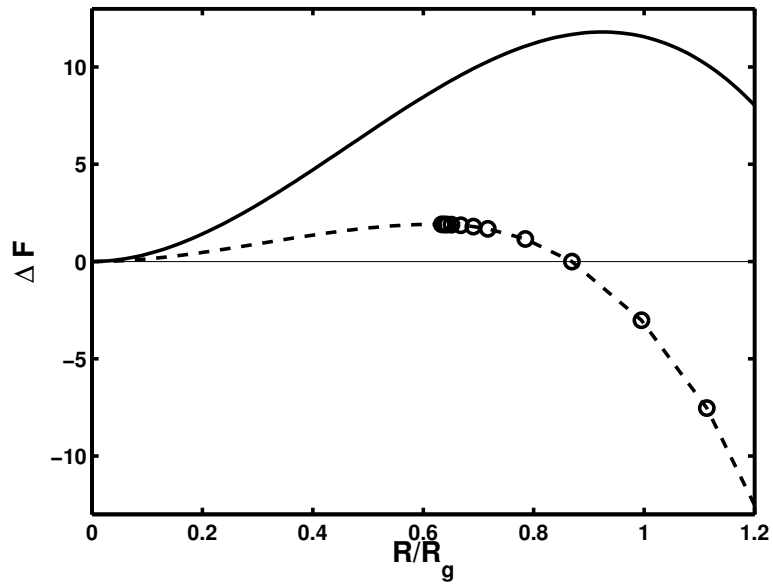


Figure 3.6: The solid line shows the free energy necessary to form a bubble of radius R ($\Delta F(R)$) in the flat surface case. The open circle and dotted line shows the free energy necessary to form a bubble of radius R ($\widetilde{\Delta F}(R)$) in the curved surface case.

value, $\widetilde{\Delta F_V} = 7.1$ and $\tilde{\gamma} = 3.3$ irrespective of bubble size, which is the expectation of CNT. However, for the curved surface case, we observe that the surface tension $\tilde{\gamma}$ and the volume free energy density $\widetilde{\Delta F_V}$ are functions of bubble radius - for smaller bubbles, surface tension is decreasing and negative volume free energy density is increasing. Fig.(3.5) shows the results.

To calculate the dimensionless free energy $\widetilde{\Delta F}(R)$ necessary to form a bubble of radius R , for the flat surface case we used eq.(3.11) and used the constant values $\widetilde{\Delta F_V} = 7.1$ and $\tilde{\gamma} = 3.3$. The solid line of Fig. (3.6) is the result of the flat surface case. For curved surface case, we directly calculated the $\widetilde{\Delta F}(R)$ using eq.(3.12). We made the box volume smaller until we could not find a solution which converged stably, i.e., which defined the critical radius. We observed that below the critical radius, intermediate accuracy calculation showed the bubble is shrinking during the course of calculation. The open circles in Fig.(3.6) is the result of the curved surface case.

From Fig. (3.6), we see that the flat surface (CNT expectation) has more than 1.5 times bigger critical radius and more than 6 times bigger nucleation barrier than the curved surface. Accordingly, our result indicates CNT predicts a much lower homogeneous nucleation rate than our results. Thus, due to the low nucleation rate expected by CNT, it has been thought that heterogeneous nucleation dominates bubble nucleation; however, our results indicate that there might be much more homogeneous nucleation possible than previously thought.

3.3 Microscopic Origins of the Failure of CNT

In the previous section, our result shows much smaller nucleation barrier $\widetilde{\Delta F^*}$ for curved surfaces compared to the $\widetilde{\Delta F^*}$ for flat surfaces(CNT). We noticed that for curved surfaces, the value of surface tension $\tilde{\gamma}$ and volume free energy density $\widetilde{\Delta F_V}$ is a function of bubble radius in contrast to the constant $\tilde{\gamma}$ and $\widetilde{\Delta F_V}$ for the flat surface. Therefore, we saw that the variation of $\tilde{\gamma}$ and $\widetilde{\Delta F_V}$ as a function of bubble radius for small radius of bubbles (nano-sized bubbles) was the reason for the significant deviation of $\widetilde{\Delta F^*}$ for curved surfaces from the $\widetilde{\Delta F^*}$ of flat surfaces. We investigate the microscopic origin of the failure of CNT by breaking down the free energy (i.e., $\tilde{\gamma}$ and $\widetilde{\Delta F_V}$) into the thermodynamic components, i.e., internal free energy, polymer configurational entropy, polymer translational entropy, and solvent translational entropy[36].

The below equations are used to calculate the components.

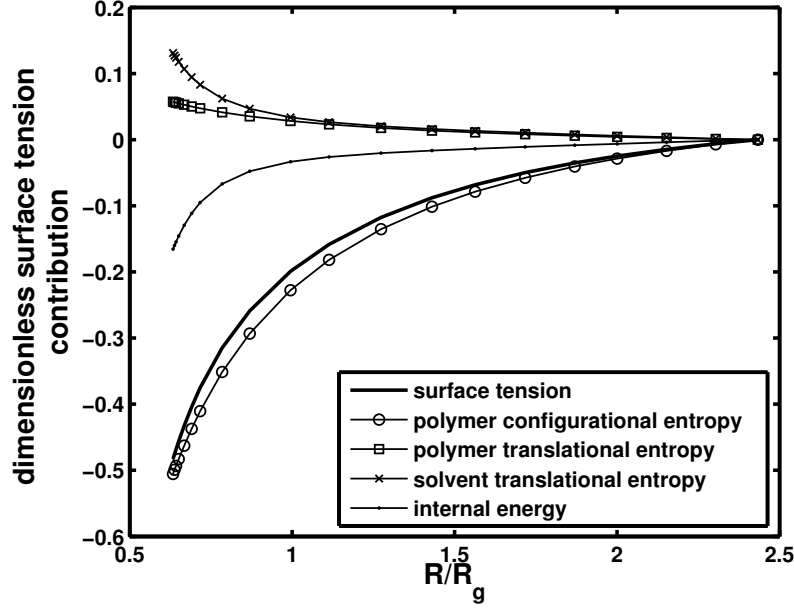


Figure 3.7: Thermodynamic components of surface tension versus bubble radius R . Increasing polymer configurational entropy is the main cause, and the decreasing internal energy is a secondary cause of decreasing surface tension for smaller bubbles. Below $0.9 R_g$, the internal energy shows a sharper decreasing.

$$\frac{U}{\rho_p k_B T V} = \frac{\chi N}{V} \int \phi_p(\vec{r}) \phi_s(\mathbf{r}) d\mathbf{r} \quad (3.13)$$

$$\frac{S_{cp}}{\rho_p k_B V} = \frac{1}{V} \int \rho_p \ln q(\mathbf{r}, 1) d\mathbf{r} + \frac{1}{V} \int \omega_p(\mathbf{r}) \phi_p(\mathbf{r}) d\mathbf{r} \quad (3.14)$$

$$\frac{S_{tp}}{\rho_p k_B V} = \frac{1}{V} \int \rho_p \ln \rho_p d\mathbf{r}, \rho_p = -\frac{\phi_p V q(\mathbf{r}, 1)}{Q_p} \quad (3.15)$$

$$\frac{S_{ts}}{\rho_p k_B V} = \frac{\phi_s}{\alpha} \ln \left(\frac{Q_s}{\phi_s V} \right) + \frac{1}{V} \int \omega_s(\mathbf{r}) \phi_s(\mathbf{r}) d\mathbf{r}. \quad (3.16)$$

If we look at the surface tension result first, Fig. (3.7), we can see that the main cause of decreasing surface tension at smaller radii of bubbles is the increasing polymer configurational entropy at smaller radii. Fig.(3.8) explains why the polymer configurational

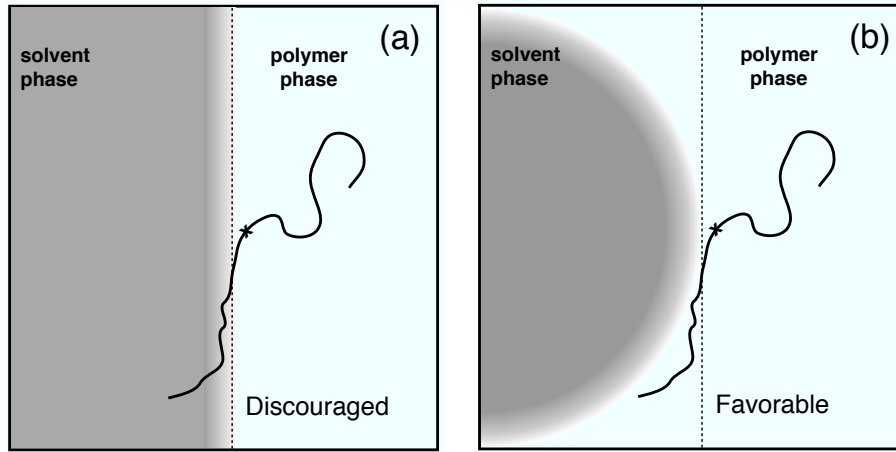


Figure 3.8: In (a) and (b) the polymer has same configuration. However, for the flat surface (a), since the surface is flat, the polymer has more contact with solvent causing higher internal energy. (b) In the curved surface, since the surface has curvature, the polymer has less contact with solvent causing lower internal energy.

entropy is decreasing at the smaller radii. In Fig.(3.8) (a) and (b), one can see two polymers which have the same configuration. However, the polymer near curved surface has less interaction energy, because the polymer near curved surface has less interaction with solvent molecule due to the curvature of the surface - the solvent and polymer molecules are immiscible.

Therefore, for bubbles with smaller radii, due to the sharper curvature of surface, the polymer has more available configurations which have lower internal energy. Consequently, the increasing conformational entropy at higher curvatures makes the free energy decrease more at smaller radii. And this causes the decreasing surface tension for smaller bubbles.

In addition, Fig.(3.7) shows that decreasing internal energy at higher curvatures is a secondary contributor causing decreased surface tension for smaller radii bubbles. Decreasing internal energy can be explained by the same mechanism as the increasing configurational entropy - as explained in Fig.(3.8). Due to the higher curvature, more conformations which have less interaction energy are available for smaller bubble radii; accordingly the internal energy is decreased and the surface tension decreases at smaller bubble radii.

From Fig.(3.7), we can also notice that the internal energy of surface tension decreases more sharply at bubbles smaller than $0.9 R_g$. This is due to the disappearance of the bulk phase inside the bubble - See Fig.(3.10). Due to the collapse of the bulk phase inside

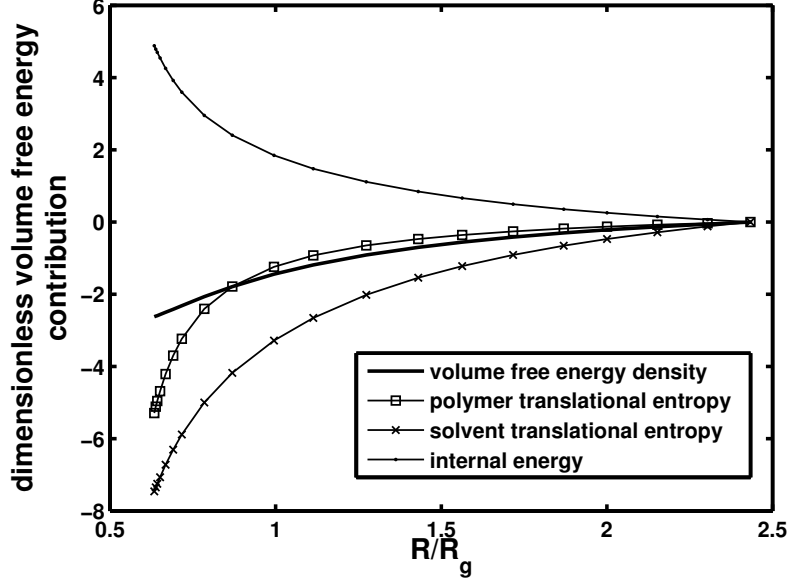


Figure 3.9: Thermodynamic components of volume free energy density versus bubble radius R . By same mechanism of surface tension, together with increasing internal energy, increasing entropy is the cause of increasing volume free energy density for smaller bubbles.

bubble, internal energy increases, i.e., there is more mixing of polymer and solvent. But, it turns out that the collapse of bulk phase inside a bubble causes a decrease of internal energy. Since surface tension is found by subtracting the free energy of the bulk phase separated system from the free energy of the inhomogeneous system, and the internal energy of the bulk phase separated system is increasing more quickly than internal energy of the inhomogeneous system, there is a sharp decrease of the internal energy at bubbles smaller than $0.9 R_g$. Consequently, the collapse of the bulk phase inside the bubble appears as a secondary cause of decreasing surface tension for smaller bubbles.

The changing volume free energy density $\widetilde{\Delta F_V}$ is also another cause of the small nucleation barrier in curved surfaces. We broke down $\widetilde{\Delta F_V}$ into its thermodynamic components. Fig.(3.9) shows the result. We see the increasing entropy for smaller bubbles is a cause of the increasing of $\widetilde{\Delta F_V}$ at small radii. This can be explained by the same mechanism with which we explained the decreasing surface tension for the small radii bubbles.

Due to the higher curvature of the surface and the collapse of the bulk phase inside the

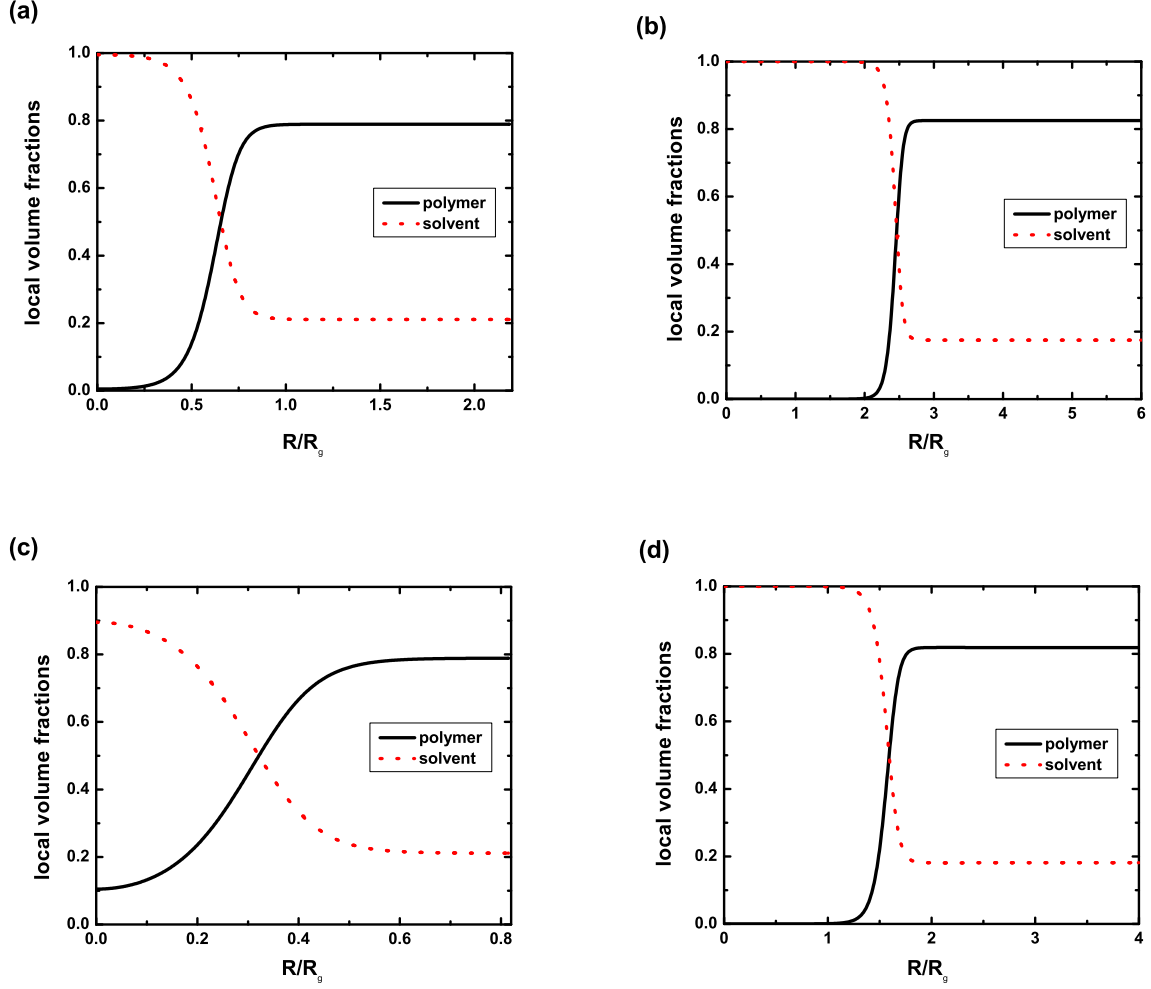


Figure 3.10: (a) Profile of a critical radius of a bubble in which inside the bubble does not reach the perfect bulk phase in case of $\chi N = 120$, $\phi_s = 0.23$. (b) Profile of a bubble with a perfect bulk phase inside a bubble in the case of $\chi N = 120$, $\phi_s = 0.23$. (c) Profile of a critical radius of $\chi N = 160$, $\phi_s = 0.26$ case. We can see a clear collapse of the bulk phase inside the bubble. (d) To compare with (c), one profile of a bubble with perfect bulk phase inside the bubble for the $\chi N = 160$, $\phi_s = 0.26$ case.

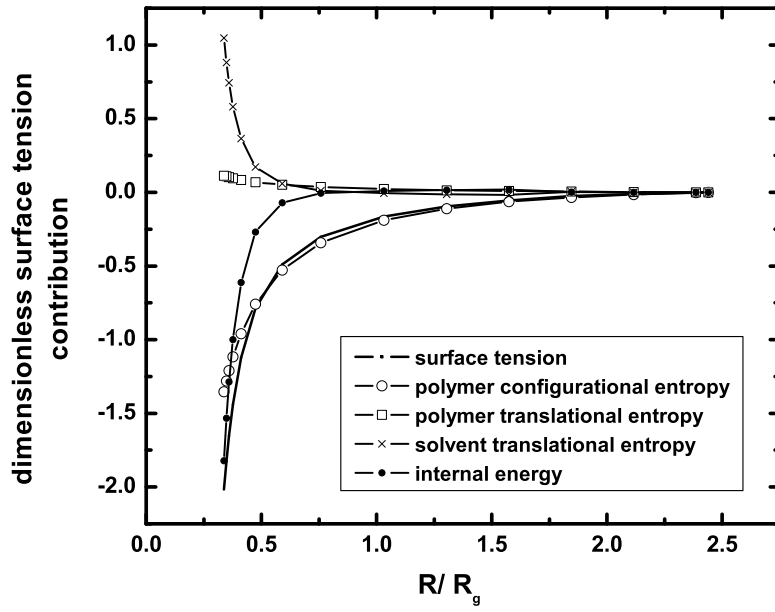


Figure 3.11: Thermodynamic components of surface tension versus bubble radius R for the case of $\chi N = 160$, $\phi_s = 0.26$. Near the critical radius, at a small radius of bubble, the decreasing internal energy becomes a main cause of decreasing surface tension for smaller bubbles.

bubble, there is more mixing of polymer and solvent molecules and consequently, there is increasing internal energy for the smaller bubbles. Consequently, because of the balance of internal energy and entropy, the entropy increases for smaller bubbles. The increasing entropy results in increasing $\widetilde{\Delta F_V}$ for smaller bubbles and causes the small nucleation barrier for curved surfaces.

In our example case, the increasing conformational entropy due to higher curvature was the main origin for the increasing surface tension, but for another case, $\chi N = 160, \phi_s = 0.26$ showed that the increasing internal energy due to the collapse of the bulk inside the bubble dominates the conformational entropy effect near the critical radius. Fig. (3.10)(c) shows the volume fractions profile of the critical radius, and Fig.(3.11) shows the thermodynamic components of the $\chi N = 160, \phi_s = 0.26$ case. Thus, in the higher segregation case, the internal energy effect might become a dominant factor though our example case in this chapter shows it as a minor origin.

3.4 Discussion and Conclusion

Considering that the flat interface assumption of CNT is not appropriate for nano-polymeric bubbles, and since nano-polymeric bubbles are comparable to polymers in size, we modelled the surface of nano-polymeric bubbles as curved surfaces. To investigate the effect of the curvature on the nucleation of bubbles, we studied flat and curved surfaces by using the same model for both. We also compared the nucleation barrier calculated in both cases. For the calculation of the free energy of inhomogeneous system, we used SCFT. For our example case, $\chi N = 140, \phi_s = 0.23$ and $\alpha = 0.01$, the results show that the flat surface(CNT expectation) has more than 1.5 times bigger critical radius, more than 6 times bigger nucleation barrier and more than five orders smaller nucleation rate than the corresponding values of curved surfaces.

Investigation of the microscopic origins of the failure of CNT revealed that higher curvatures and the disappearance of the bulk phase inside bubbles causes the decreasing surface tension and the increasing negative volume free energy density for smaller bubble. Consequently, there was a smaller nucleation barrier for the curved surface case. In our example case, the increasing conformational entropy due to higher curvature was the main origin for the increasing surface tension, but for a higher segregation case, our results showed the internal energy effect is a dominant factor.

In conclusion, our calculation of nucleation rate for nano-polymeric bubbles using SCFT with the assumption of curved surfaces shows much smaller nucleation barriers with the

smaller critical radii than predicted by CNT(flat surfaces). It turns out that the origins of the failure of the CNT are the assumptions of CNT which are not appropriate for nano-sized bubbles - sharp flat surfaces and bulk phases inside bubbles. Curved surface results show that the high curvature and the collapse of the bulk phase inside a small bubble makes for much smaller nucleation barriers, i.e., much bigger homogeneous nucleation rates than CNT predicts. Thus, our results indicate that there is a much higher possibility of homogeneous nucleation than previously thought based on CNT.

In this chapter we used an incompressible system for simplicity, but to deal with more realistic systems, we will need to use a compressible model by using an equation of state, i.e., by incorporating pressure.

Chapter 4

Maximal Cell Density and Temperature Effect on Cell Density

Generally, “Good quality foam” means a foam which has a high cell density with closely spaced and uniformly distributed small bubbles. CNT is often used to calculate cell density, but in CNT, calculation of the nucleation barrier or nucleation rates are needed to calculate the cell density. However, as we showed in the previous chapter, CNT is not appropriate for predicting nucleation rates for nano-cellular foams, as CNT makes assumptions that are not applicable to nano-sized bubbles. In this chapter, we calculated the maximum possible bubble number density directly by using SCFT without calculation of nucleation barrier or nucleation rates.

In contrast to CNT, which can only calculate nucleation rates at the critical radius, we calculated cell density as a function of bubble radius. Interestingly, our results show that the radius of the maximal bubble surface area is different from the critical radius - it is slightly bigger than the critical radius. Also, we noticed that the bulk condition at the center of the bubble is reached at yet another radius, which is slightly bigger than the radius of maximal surface area per unit volume. Thus, unlike CNT, we can find the upper bound maximal cell density corresponding to the critical radius, the radius of maximal bubble surface area, and the radius of the bubble with bulk condition at the center of the bubble. Thus, one can choose the “best foam” depending on the application.

On the other hand, our maximal cell density in this chapter is an upper bound on the cell density, i.e., experimentalists would get lower cell densities. However, our results can

qualitatively show at which experimental conditions - temperature, solvent density, ratio of solvent and polymer molecular weight, etc - experimentalists can get better foams. We examined maximal density in different solvent density cases at two different temperatures. Our results show that foams generally have higher maximal cell densities at lower temperatures despite the higher surface tension at lower temperatures - contradicts with CNT prediction, since CNT predicts a higher cells density at higher temperatures because surface tension is lower at higher temperature. Our SCFT results also reveal that in polymeric foaming at different temperatures, the volume free energy density is a more important factor than surface tension.

In the first section, we describe how we calculate bubble number density as a function of bubble radius. In section 2, we show example results for $\chi N = 160$ - bubble number density of three “best foams” in view of maximal cell density, maximal bubble surface area per unit volume, and bulk condition at the center of a bubble at different solvent density cases. Then, we discuss the conditions for the better foam which SCFT and CNT provide at one temperature. In section 4, we compare the results of two different temperature cases, $\chi N = 160$ and $\chi N = 120$, and discuss the prediction of SCFT that CNT can’t provide. In the final section, the conclusion and discussion are written.

4.1 Calculation of Bubble Number Density

In CNT, the nucleation rate is written

$$J = J_0 \exp\left(-\frac{\Delta F^*}{k_B T}\right) \quad (4.1)$$

, where the nucleation barrier ΔF^* is given by

$$\Delta F^* = \frac{16\pi}{3} \left(\frac{\gamma^3}{\Delta \mathcal{F}_V^2} \right) \quad (4.2)$$

Therefore, to calculate the cell density in CNT one needs to integrate the nucleation rate over time based on the nucleation barrier and also derive the prefactor J_0 through other means. We showed in the previous chapter that for high curvature surfaces, the nucleation barrier deviates from the nucleation barrier expected in CNT. Also, CNT can only predict cell densities at the critical radius.

Using SCFT, we calculate the bubble number density as a function of the radius of a bubble directly. In this chapter, we use the same inhomogeneous free energy formula and the same model as the previous chapter. Therefore, as we described in the previous chapter, in our model, we change the size of a bubble by changing the size of the system while the global volume fraction ϕ_s is held constant. In the previous chapter, since we examined the free energy necessary to form a typical size of bubble, we had to subtract the initial homogeneous system energy from the inhomogeneous system energy, i.e., the system after formation of the bubble. Since the number of molecules is conserved, we put the global volume fraction value of the initial homogeneous system as our system global volume fraction value. Thus, our system global volume fraction values are the same as the macroscopic system global volume fraction values.

Therefore, our bubbles are representative bubbles of our macroscopic system, i.e., we can think as if the macroscopic system is filled with the one representative bubble though in reality the macroscopic system would be filled with various sizes of bubbles. Thus, we can calculate the bubble number density simply as the inverse of the system(box) volume. However, in this chapter, we use the cell density definition for polymer foaming, i.e., the number of bubbles per unit volume of polymer. Therefore, we calculate the cell density as the inverse of the box volume times polymer volume fraction.

4.2 The "Best" Foam

We investigated a case of $\chi N = 160$ and different global volume fraction values ranging from 0.17 to 0.29, which is in the nucleation and growth region. As mentioned, we calculated bubble number density, bubble surface area per polymer volume, and the solvent volume fraction at the center of a bubble as a function of bubble radius at each different solvent volume fraction case. Fig. 4.1 (a) shows the result of the bubble number density as a function of radius of a bubble. It is not surprising that at the smallest radius, i.e., at the critical radius, the foam has the maximal bubble number density. Thus, if we choose a foam which has the maximal bubble number density as the best foam, the best foam is formed at the critical radius, and we can simply get a result of Fig.4.1(b). Fig.4.1(b) shows the maximal bubble number density at different solvent volume fractions, and we see a higher cell density with increased blowing agent, which is consistent with observations. [13],[28],[19],[60],[14].

Fig. 4.2(a) shows the bubble surface area per bubble box volume as a function of bubble radius at different solvent volume fractions. As mentioned above, surprisingly the maximal

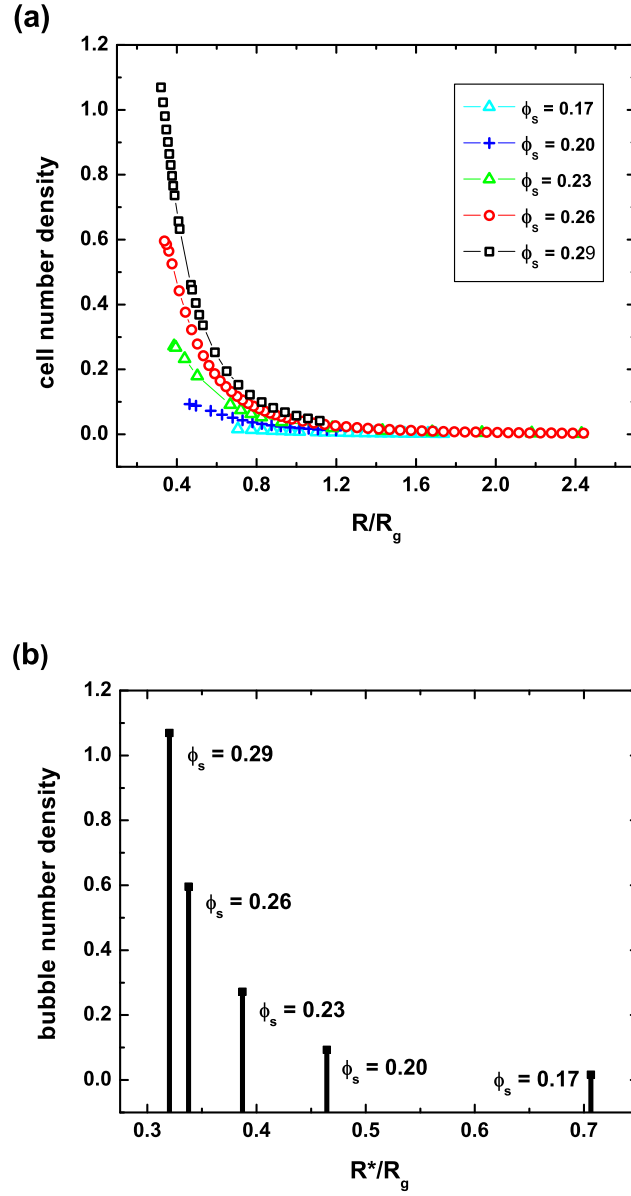


Figure 4.1: At $\chi N = 160$ (a) Dimensionless bubble number density versus radius of a bubble. (b) Dimensionless bubble number density at the critical radius of a bubble at different solvent volume fraction systems.

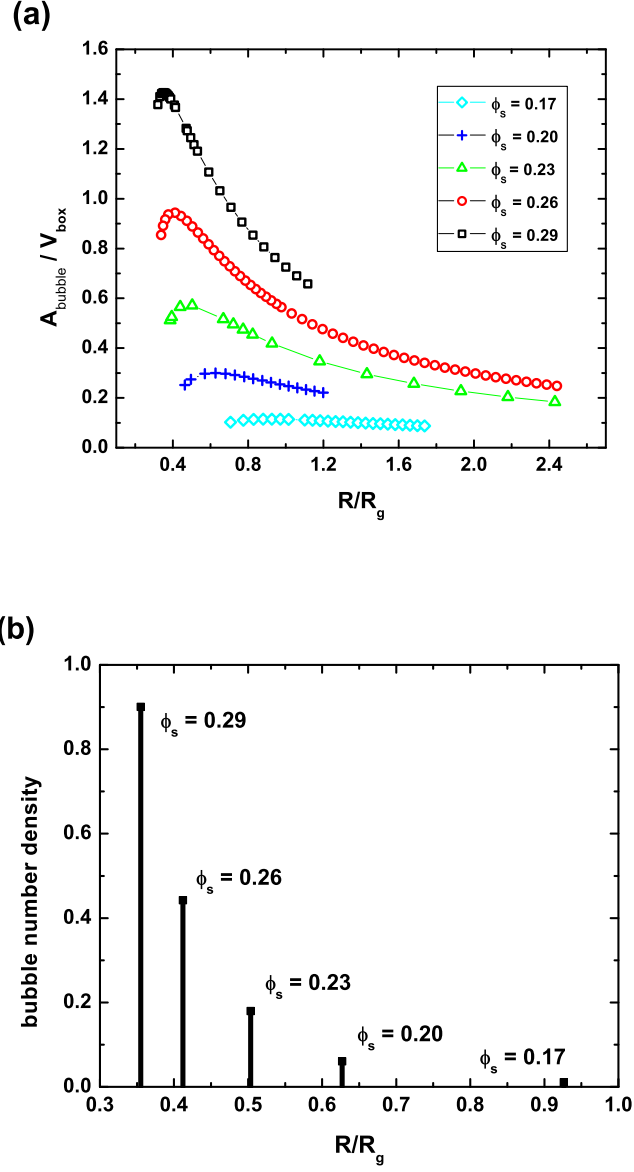


Figure 4.2: At $\chi N = 160$ (a) Dimensionless bubble surface area per bubble box volume ($\phi_s \times V_{box}$) versus radius of bubble. (b) Dimensionless bubble number density at the radius of the maximum of A/V .

surface area doesn't occur at the critical radius - it occurs at a slightly bigger radius than the critical radius. Interestingly, this means that a foam which has the maximal number density does not have the maximal bubble surface area. It seems that before the radius of maximal surface area, bubble nucleation dominates the bubble growing, and after the radius of maximal surface area, the bubble growing dominates the bubble nucleation. Fig. 4.2(a) shows the cell density as a function of bubble radius at different solvent volume fraction. We can see that at higher volume fraction of blowing agent, the radius of the maximal surface area is reached more quickly, so it seems that more active nucleation occurs with increased blowing agent. Fig. 4.2(b) shows the cell density at the radius of the maximal bubble surface area at different solvent volume fraction cases. It also shows the higher cell density with increased solvent.

On the other hand, we examined the solvent volume fraction at the center of a bubble. Fig.(4.3)(a) is the plot of solvent volume fraction at the center of a bubble as a function of bubble radius at different solvent volume fraction. It shows that at the critical radius and the radius of the maximal bubble surface area, the bulk condition at the center of a bubble was not reached. Thus, from the perspective of the quality of a bubble, at the critical radius and the maximal surface area, the bubble quality is poor.

From the point of view of the quality of a bubble, the best foam can be defined as a foam filled with bubbles which reach the bulk condition at the center. Fig. 4.3(a) shows all points fall on top of each other irrespective of the global solvent density. That means the solvent volume fraction at the center of a bubble is a function of bubble radius. We can see that at the bubble radius $R = 0.7R_g$, the bulk condition is reached inside the bubble irrespective of the global solvent density. Fig. 4.3(b) shows the bubble number density at $R = 0.7R_g$ at different solvent volume fraction, and again this result shows a higher cell density with increased solvent volume fraction.

For all three cases - critical radius, maximal surface area, and bulk condition at the center of a bubble - results show that the greater the solvent volume fraction, the higher the cell density. However, at the critical radius case or at the maximal surface area case, the cell density was quickly increased with increased solvent volume fraction compared to the bulk condition inside the bubble case. Also for the bubble size, at the critical radius or at the maximal surface area cases, the bubble size is smaller with the increased blowing agent volume fraction whereas for the bulk condition at the center case, the bubble size was same.

Accordingly, SCFT shows several interesting results CNT can't provide - 1) the radius of the maximal surface area is different with the critical radius, i.e., a little bigger than the

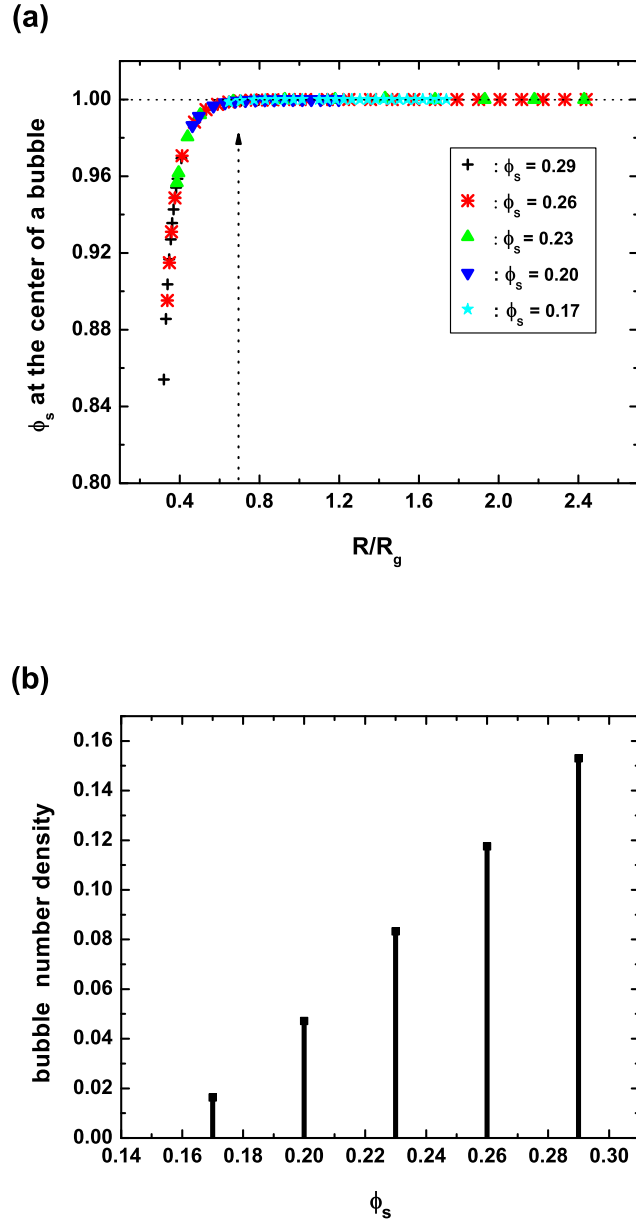


Figure 4.3: At $\chi N = 160$ (a) Solvent volume fraction value at the center of bubble versus radius of the bubble (b) Dimensionless bubble number density at the bubble radius $R = 0.7R_g$ at different solvent volume fraction systems

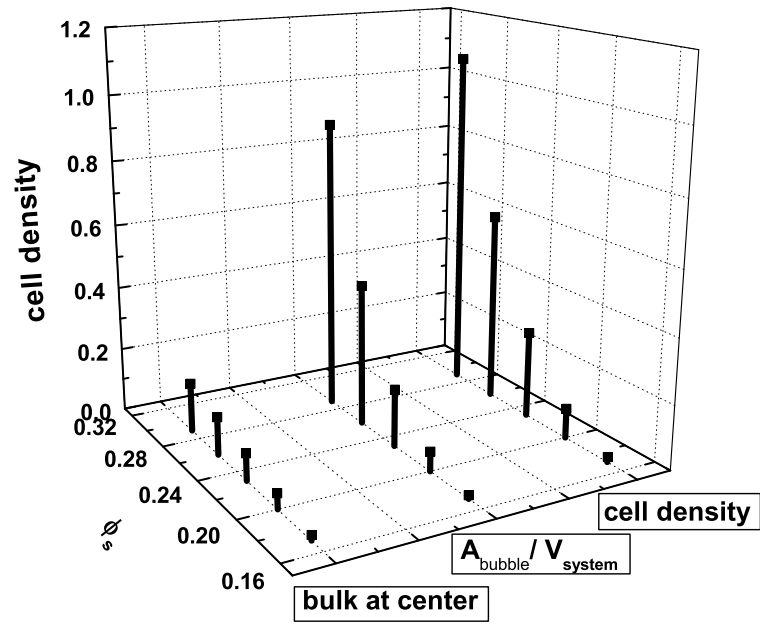


Figure 4.4: At $\chi N = 160$, dimensionless bubble number density at different solvent volume fraction systems in view of maximal number density, maximal bubble surface area, and bulk condition at the center of a bubble.

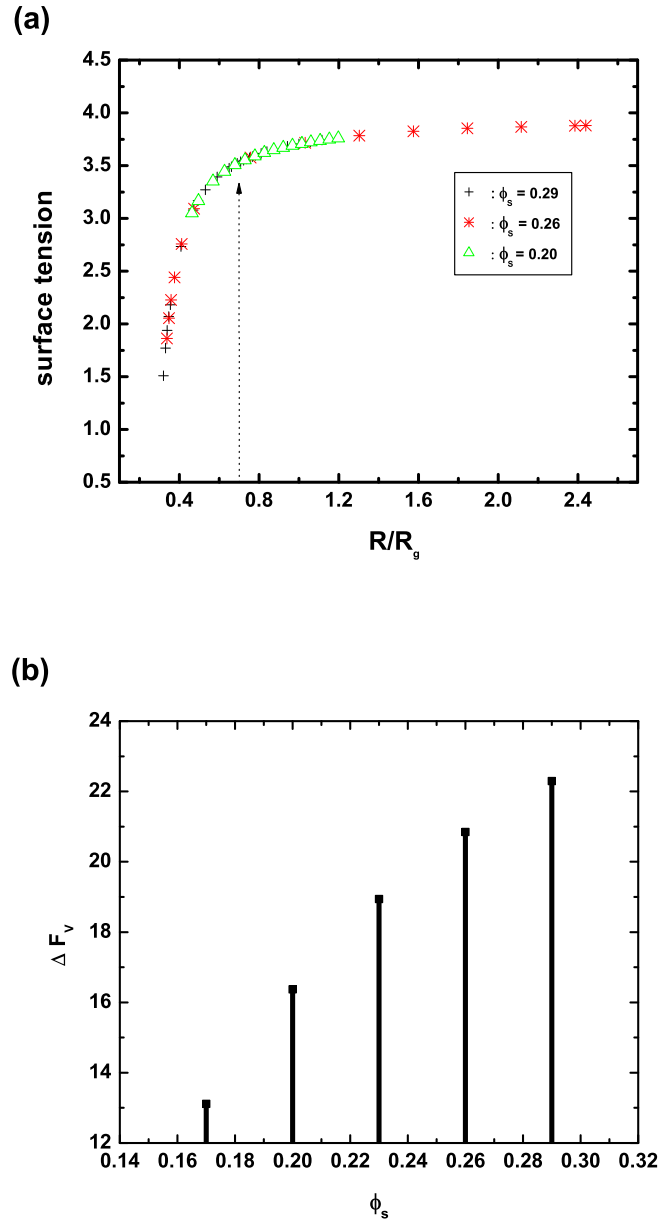


Figure 4.5: At $\chi N = 160$, (a) Dimensionless surface tension γ versus radius of bubble. (b) $-\Delta F_V$ at $R = 0.7R_g$ at different solvent volume fraction systems.

critical radius. 2) at the critical radius, and the maximal surface radius, the bulk condition at the center of a bubble is not reached - interestingly, the solvent volume fraction is a function of the radius of a bubble, and consequently, the radius of the bulk condition inside the bubble is the same irrespective of the global solvent volume fraction.

Thus, if one is more interested in small bubble sizes and high bubble number densities rather than bubble quality, then high solvent volume fraction would be effective. But, if one is more interested in bubble quality and the bubble size, then at the same temperature, the high solvent volume fraction would not be effective in that purpose. Even though the cell density would be still better at high solvent volume fraction, but the difference is not significant like at the critical radius and the maximal surface area as we can see in Fig. (4.4).

4.3 Temperature Effect on the Bubble Number Density

At mentioned above, qualitatively our SCFT results provide conditions under which a better foam could be formed. Now, we investigate whether predictions of SCFT are qualitatively consistent with CNT predictions. In the previous chapter, we showed that for nano-polymeric bubbles, surface tension γ and the volume free energy density ΔF_V are functions of bubble radius whereas in CNT, γ and ΔF_V are constant. Therefore, it is appropriate to compare the predictions of SCFT and CNT for cell density. First, at a given temperature, i.e., $\chi N = 160$, we calculated surface tension γ and the volume free energy density ΔF_V at different solvent volume fraction cases. Fig. 4.5 shows the results. Interestingly, like the solvent volume fraction at the center, all the points fall on top of each other. This means surface tension γ is also a function of the radius of a bubble irrespective of the solvent volume fraction.

Therefore, if we choose the good quality foam as the "best" foam rather than the maximal cell density or maximal surface area, surface tension γ is same at different solvent volume fraction. Thus, as far as γ is concerned the prediction of SCFT and CNT are same. However, for the ΔF_V , our results show ΔF_V increases with increasing solvent volume fraction.

Since our results show bigger ΔF_V at higher solvent volume fraction, in CNT, according to eq. 4.2 the nucleation barrier is smaller at higher solvent volume fraction. That means higher nucleation and higher cell density at the higher solvent density, which is consistent with SCFT predictions. Therefore, at a given temperature, both SCFT and CNT predic-

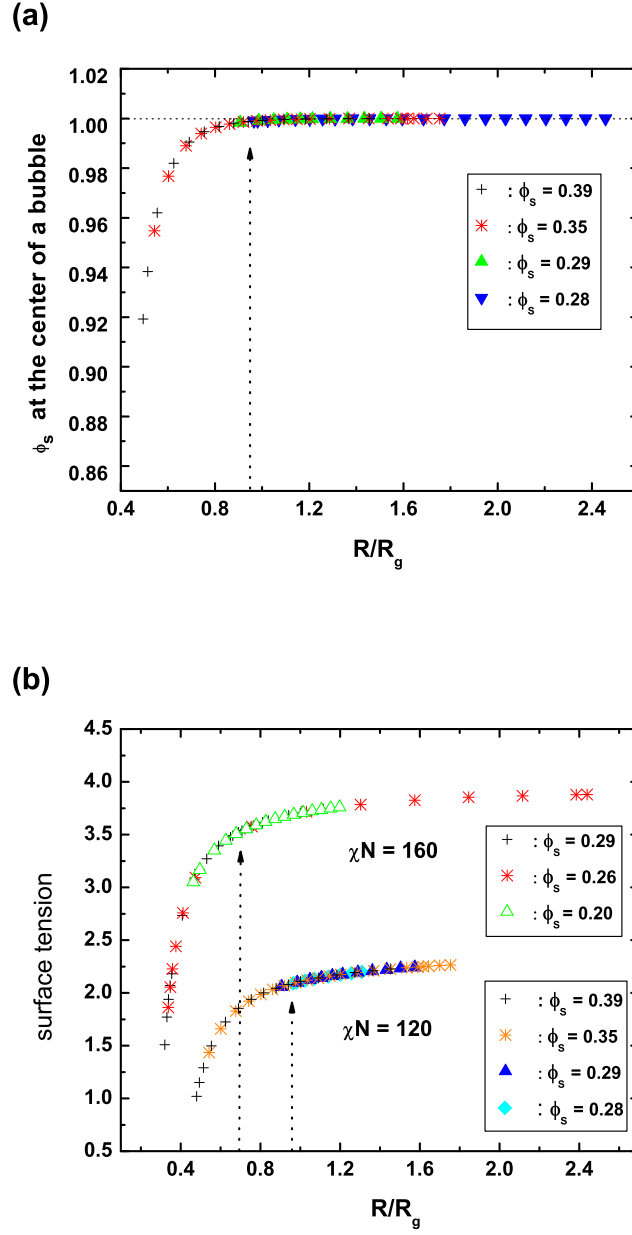
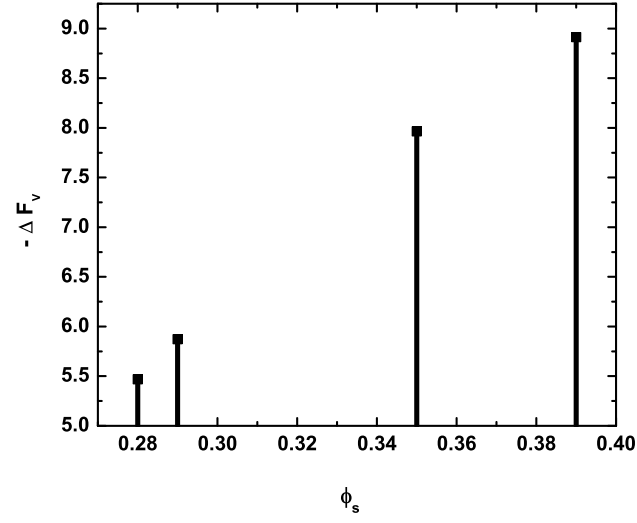


Figure 4.6: Solvent volume fraction value at the center of a bubble versus radius of the bubble at different solvent volume fraction systems at $\chi N = 160$. (b) Surface tension versus radius of a bubble at different solvent volume fraction systems at $\chi N = 120$ and at $\chi N = 160$

(a)



(b)

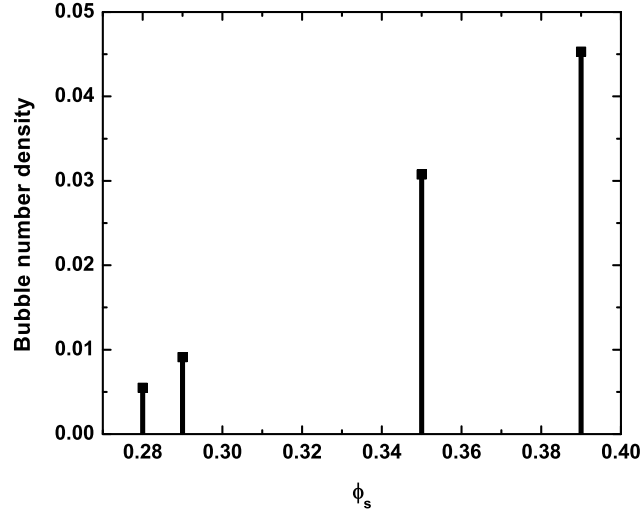


Figure 4.7: At $\chi N = 120$, (a) Negative volume free energy density ΔF_v and (b) dimensionless bubble number density at different solvent volume fraction systems

tions are the same - higher cell density at a higher solvent volume fraction.

However, at different temperatures, we observe that SCFT reveals information which CNT can not provide. We investigate a different temperature case, $\chi N = 120$, which is a higher temperature than $\chi N = 160$, with ϕ_s varying from 0.28 to 0.39, which is the nucleation and growth region. Like the case of $\chi N = 160$, the solvent volume fraction at the center and surface tension are functions of bubble radius as can be seen from Fig. 4.6 (a). Like the case of $\chi N = 160$, ΔF_V and cell density are increasing with increased solvent volume fraction at $\chi N = 120$. Therefore, we can confirm that at a given temperature, SCFT and CNT give same information - higher cell density at a higher solvent volume fraction. However, unexpectedly at $\chi N = 120$, the bubble size at which bulk conditions are reached at the center is $R = 0.96R_g$, which is bigger than the $R = 0.7R_g$ at $\chi N = 160$. We might expect at $\chi N = 120$, that the bubble size would be smaller, because as we can see from Fig. 4.6 (b) at higher temperature, i.e., smaller $\chi N = 120$, surface tension is smaller. According to CNT, as critical radius is written as

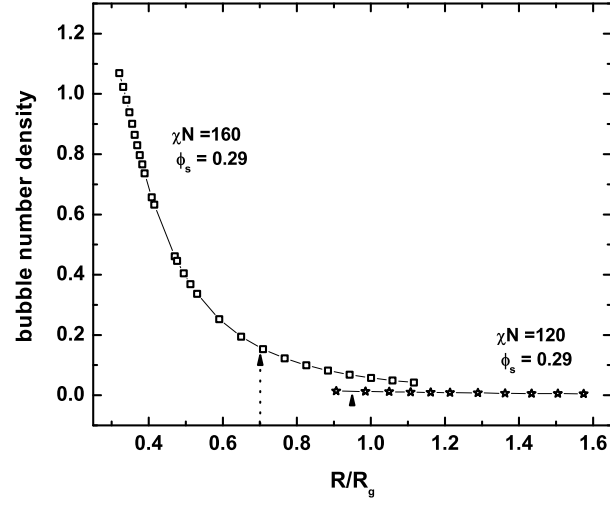
$$R^* = \frac{\gamma^3}{\Delta F_V^2} \quad (4.3)$$

if γ is small, we can expect the critical radius to be small, and the radius of bulk condition at the center of bubble to be smaller.

However, we find the opposite result - a bigger bubble radius at a higher temperature.

Thus, we investigated the volume free energy density ΔF_V , which is another parameter in CNT. To investigate the temperature effect, we chose the same solvent volume fraction case for the two temperatures - $\phi_s = 0.29$ at $\chi N = 120$ and $\chi N = 160$. From Fig. 4.8, we see the bubble number density is bigger at $\chi N = 160$, low temperature, as is the bubble size. However, in Fig. 4.8(b) we see that ΔF_V is bigger at the lower temperature case, $\chi N = 160$. Therefore, we can conclude that the volume free energy density ΔF_V is a more dominant factor than surface tension γ on cell density. From CNT eq.(4.2) we can predict this : if surface tension is smaller and volume free energy density is bigger, then the nucleation barrier would be smaller, i.e., the cell density would be higher. But, CNT doesn't predict which parameter is a more dominate factor on cell density. Fig. 4.9 (a) and (b) show bubble number density and ΔF_V at $\chi N = 120$ and 160 at different solvent densities. Despite of the bigger surface tension at $\chi N = 160$, *foamshaveahigher celldensityat* $\chi N = 160$ except much smaller solvent density cases. Thus, our SCFT results reveal that the volume free energy density ΔF_V is the dominant factor to make good quality, high cell density foams. Consequently, SCFT predicts that low temperature is more important than high solvent

(a)



(b)

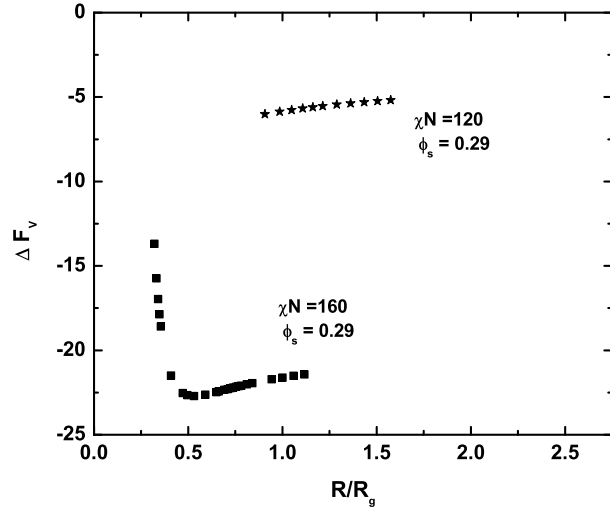
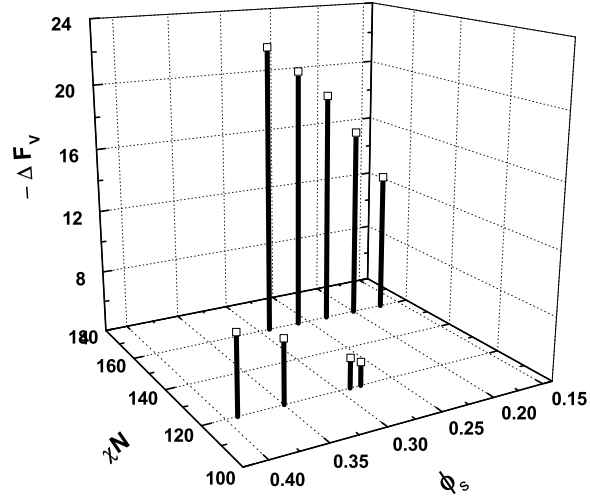


Figure 4.8: At $\chi N = 160$, $\phi_s = 0.29$ and $\chi N = 120$, $\phi_s = 0.29$ (a) Dimensionless bubble number density. (b) ΔF_v versus radius of bubble

(a)



(b)

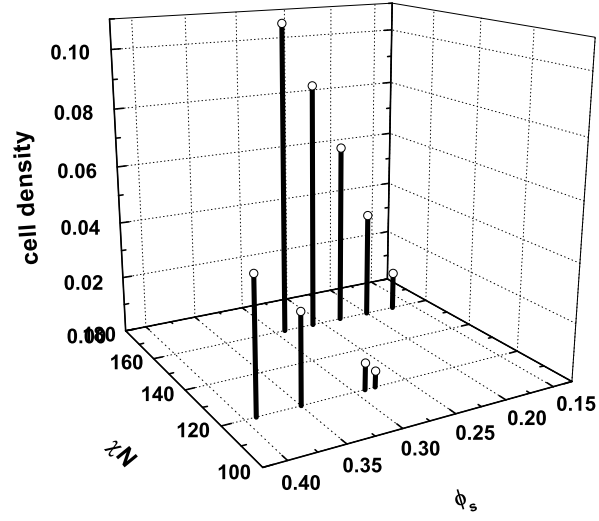


Figure 4.9: At different solvent density systems at $\chi N = 120$ and $\chi N = 160$ (a) $-\Delta F_v$ (b) Dimensionless bubble number density

density for producing a good quality foam of high bubble density. These properties are not predicted by CNT.

4.4 Discussion and Conclusion

By using a SCFT model, we directly calculated cell density as a function of bubble radius without calculation of nucleation barrier and nucleation rates in CNT. Therefore, we investigated the cell density in view of maximal cell density(critical radius), maximal bubble surface area, and bulk conditions at the center of a bubble. Our examples show that the maximal cell density and maximal bubble surface area cases do not form good quality bubbles - at the center of a bubble, bulk condition are not met - thus, we choose the best foam as the foam that has bubbles with bulk conditions at the center. By using the cell density of the best foam at different solvent volume fractions, at a given temperature, SCFT and CNT predictions show the same trend - higher solvent volume fraction gives higher cell density. However, at different temperatures, SCFT results reveal that at lower temperatures [13, 56, 55], a higher cell density is formed, despite the fact that surface tension is bigger at low temperatures. It turns out that the negative volume free energy, which is higher at lower temperatures, contributes to the higher cell density at lower temperatures. Therefore, our SCFT results show that the volume free energy density is a more important factor than surface tension determining cell density of polymer foams.

In this chapter, we demonstrated that SCFT calculations show the optimal conditions such as temperature, chemistry, or amount of blowing agent for the formation of the best foams. At a given temperature, we see that CNT and SCFT prediction is same - higher cell density at higher solvent density. However, we observed that SCFT results reveal higher cell densities at lower temperatures and that volume free energy density ΔF_V is a more important factor than surface tension γ for determining nucleation barriers. This is not predicted by CNT.

Like the previous chapter, we used the incompressible system in this chapter for simplicity. For future work, we will need to use a compressible system which is a more realistic system, and confirm if the results of this chapter are qualitatively consistent with results of the compressible system.

Chapter 5

Maximal Cell Density in Compressible Systems

In this chapter, we drop the incompressible limitation we have in the previous chapters. We use a hole -based self-consistent field theory [17] to deal with a compressible system. Thus, by adding holes, our system volume expands, and our system volume is described as a function of hole volume fraction. According to our model, the representative bubble is filled in the system, the system pressure should be the same as the representative bubble pressure. In view of a good quality foam, as a representative bubble we chose the smallest bubble of $\varphi_s(0) \approx 1$. $\varphi_s(0) \approx 1$ means that at the center of a bubble, the solvent volume fraction value is near 1.0, i.e., the bulk condition is reached at the center.

We calculated the inhomogeneous system pressure, homogeneous system pressure, and cell density as a function of the system volume. Inhomogeneous system is a system in which the representative bubbles are filled in, and homogeneous system is a system in which there is no bubble. Using the results we investigated not only the cell density but also the correlation between the pressure drop rate and cell density. We also qualitatively compared results of compressible system with the results of the incompressible system.

In the first section, we explain how the inhomogeneous system pressure is calculated. In the second section, we investigate the maximal cell density for three different processing conditions ; different temperatures with the same initial high pressure; different solvent volume fractions at the same temperature; and different temperatures with the same solvent volume fraction. Conclusions and discussion are written in the last section.

5.1 Theory

5.1.1 Optimal Pressure

In compressible systems, one needs to determine the system pressure at different system volume. At an initial high pressure, one can determine the system pressure experimentally because the system is in equilibrium with the outside pressure, and since the system is homogeneous, one can calculate the initial pressure by using an equation of state. However, when system pressure is dropping, the system is inhomogeneous. Therefore, the system pressure is unknown, because we cannot use an equation of state to calculate the inhomogeneous system pressure.

However, in this chapter with an assumption the system has an optimal pressure, we calculate system pressure as a function of system volume by using our model. In our incompressible system model in the previous chapters, the observed bubbles were the representative bubbles of the incompressible system. Since we use the same model used in the compressible system, if we find out a representative bubble of a compressible system, then the representative bubble pressure should be same with the compressible system pressure.

The following is the method used to determine the optimal pressure of the inhomogeneous system as a function of the system volume when the system volume expands with dropping pressure.

First, when the system volume expands, the system volume is described as a function of the global hole volume fraction - by increasing the global hole volume fraction, we make the system volume bigger. Since we assume the polymer and solvent closed packed volumes are not changed, the global polymer and solvent volume fraction values are described as a function of the expanding system volume. As a result, the global hole volume fraction is also a function of the expanding system volume by the constraint of the incompressibility.

If V_p^*, V_s^* are the initial total polymer and solvent molecule closed packed volumes, V_p^*, V_s^* are written

$$V_p^* = n_p N v_p^* \quad (5.1)$$

$$V_s^* = n_s v_s^* \quad (5.2)$$

, where n_p and n_s are total number of polymer and solvent molecules respectively, N is the degree of polymerization, and v_p^* and v_s^* are the closed packed polymer segment volume

and solvent molecule volume respectively. Therefore, V_p^* and V_s^* don't change when the system volume expands. If V_0 is the initial system volume, then the initial global polymer volume fraction ϕ_p^0 and initial global solvent volume fraction ϕ_s^0 are written

$$\phi_p^0 = \frac{V_p^*}{V_0} \quad (5.3)$$

$$\phi_s^0 = \frac{V_s^*}{V_0} \quad (5.4)$$

$$V_p^* + V_s^* = V_0 \quad (5.5)$$

Then, at one specific expanded system volume V_{sys} ,

$$V_{sys} = cV_0, (c > 1) \quad (5.6)$$

the global polymer, solvent, and hole volume fractions at one system volume V_{sys} are written

$$\begin{aligned} \phi_p &= \frac{V_p^*}{V_{sys}} \\ &= \frac{V_p^*}{cV_0} = \frac{1}{c}\phi_p^0 \end{aligned} \quad (5.7)$$

$$\begin{aligned} \phi_s &= \frac{V_s^*}{V_{sys}} \\ &= \frac{V_s^*}{cV_0} = \frac{1}{c}\phi_s^0 \end{aligned} \quad (5.8)$$

$$\begin{aligned} \phi_h &= \frac{V_h}{V_{sys}} \\ &= 1 - \phi_p - \phi_s \end{aligned} \quad (5.9)$$

The last eq. (5.9) obeys the relation

$$\phi_p + \phi_s + \phi_h = 1 \quad (5.10)$$

Therefore, the global polymer, solvent, and hole volume fraction values are functions of system volume V_{sys} ($= cV_0$).

Second, we fix the system volume, i.e., at one constant c , we can change the cell size by changing the bubble box volume until we get the critical cell in that fixed system volume as we did in the incompressible system. Third, we determine a representative bubble for a specific system. As we did in the previous chapter, we choose three bubbles which give the highest cell density, maximum bubble surface area per unit volume, and the smallest bubble with $\varphi_s(0) \approx 1$. Then, we have three optimal pressures of the system corresponding to the highest cell density, the maximum bubble surface area per unit volume, and the smallest bubble with $\varphi_s(0) \approx 1$.

To calculate the bubble(box) pressure we use the thermodynamic pressure definition

$$P = -\left(\frac{\partial F}{\partial V}\right)_{n_p, n_s, T}, \quad (5.11)$$

and calculate numerically.

For the numerical calculation of the pressure, we use the below equations for the value of global volume fractions. To conserve the polymer and solvent molecules in the bubble box, the global polymer, solvent, and hole volume fraction values at bubble box $V + \Delta V$ are written

$$\phi_p(V + \Delta V) = \left(\frac{V}{V + \Delta V}\right)\phi_p(V) \quad (5.12)$$

$$\phi_s(V + \Delta V) = \left(\frac{V}{V + \Delta V}\right)\phi_s(V) \quad (5.13)$$

$$\phi_h(V + \Delta V) = 1 - \phi_p(V + \Delta V) - \phi_s(V + \Delta V) \quad (5.14)$$

Fig 5.1(a) shows one example plot of pressure at each system volume. Because of the scale of the plot, the pressure values looks the same in plot (a), but in plot (b), which is a blow-up figure of $V = 1.1V_0$, we can see seven different pressure values corresponding to different sizes of bubble at $V = 1.1V_0$. Plot (c) shows which bubble corresponds to a representative bubble of the highest cell density, the maximum bubble surface area per unit volume, and the smallest bubble with $\varphi_s(0) \approx 1$.

Fig. 5.2 (a), (b) and Fig 5.3 (a) show plots of bubble density, bubble surface area per unit volume, and solvent volume fraction at the center of a bubble respectively as a

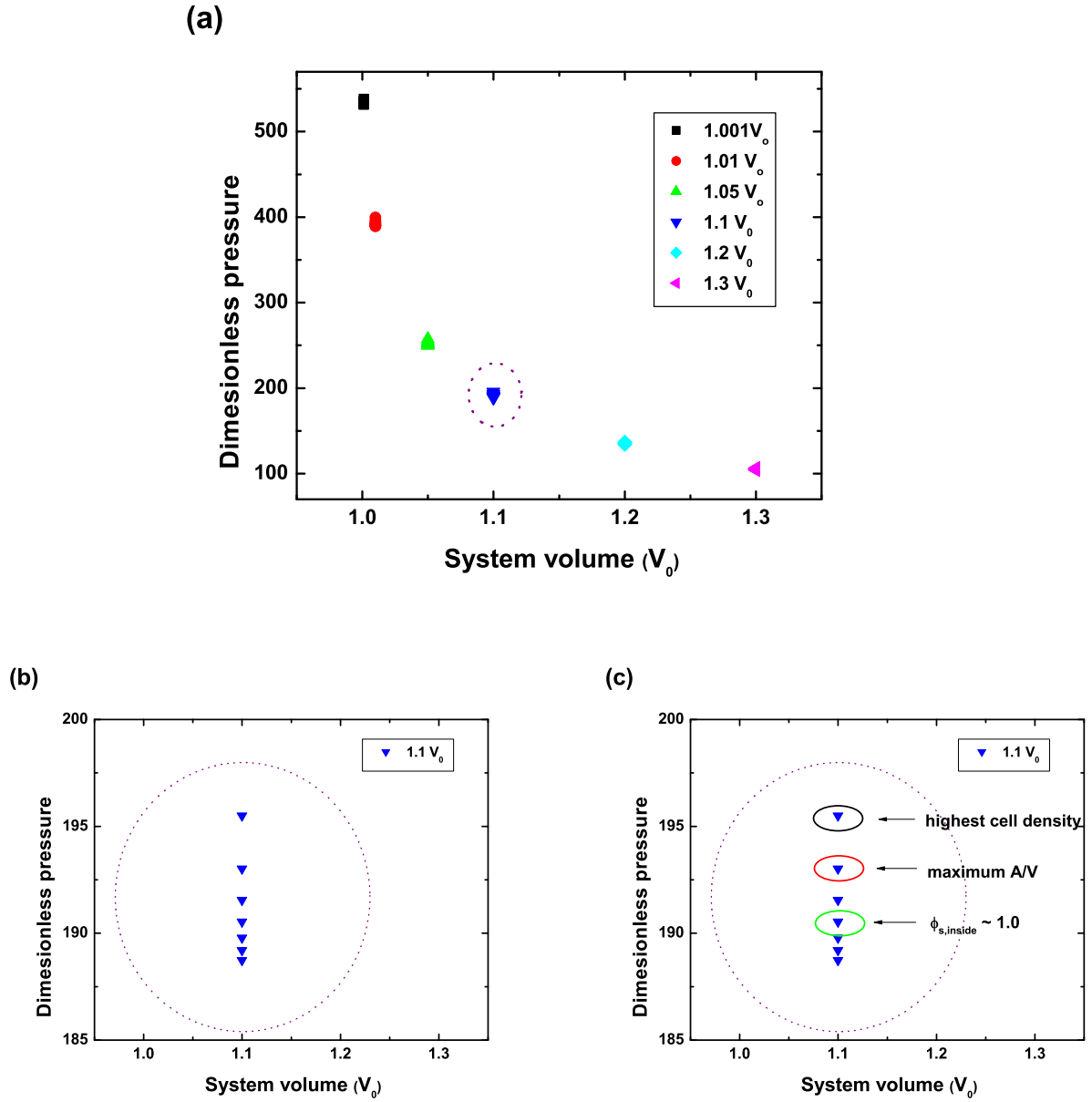
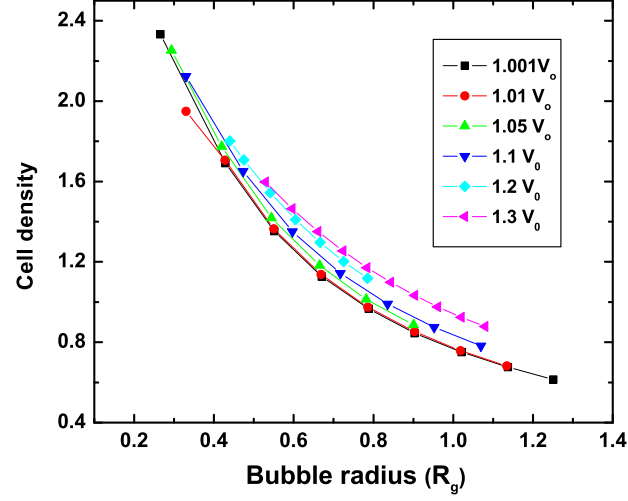


Figure 5.1: (a) Plot of several bubble pressures at different system volumes. (b) Blow up of several bubble pressures at $V_{sys} = 1.1V_0$. (c) Three representative bubble pressures at $V_{sys} = 1.1V_0$.

(a)



(b)

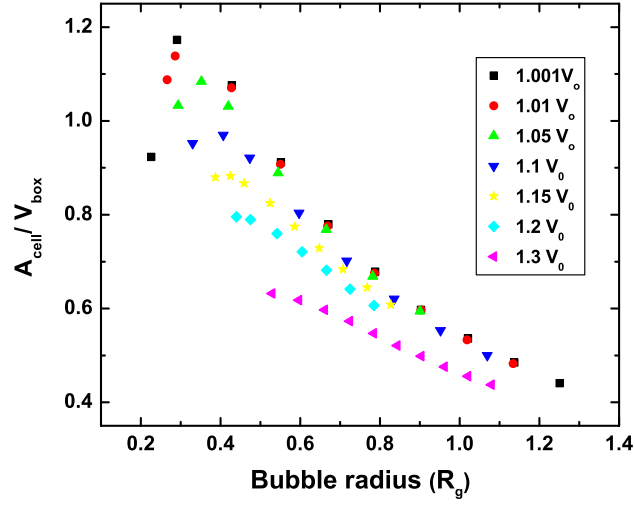


Figure 5.2: (a) Cell density versus bubble radius at different system volumes. (b) $A_{\text{bubble}}/V_{\text{box}}$ versus bubble radius at different system volume.

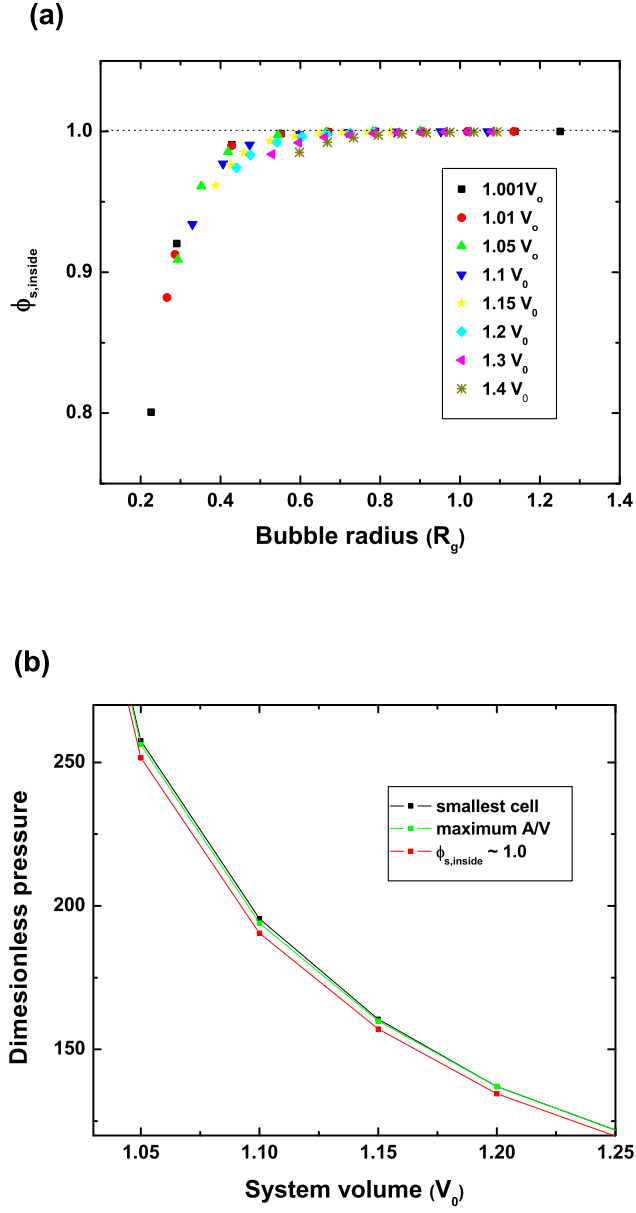


Figure 5.3: (a) Solvent volume fraction value at the center of bubble versus bubble radius at different system volumes. (b) Plot of three optimal pressures of smallest cell, maximum A_{bubble}/V_{box} , and $\varphi_s(0) \approx 1$ at the center of bubble.

function of bubble radius. We defined the radius at which the solvent and polymer volume fraction values are cross as the bubble radius. We can see from Fig. 5.2 (a) that at the critical radius, the foam has the highest cell density. Also we can see from Fig. 5.2(b) that at a little bigger radius than critical radius, a maximum A_{bubble}/V_{box} exists for a system volume just like the incompressible system. With data of Fig. 5.2 (a), (b) and Fig 5.3 (a) we plot the three optimal pressures corresponding to the highest cell density, a maximum A_{bubble}/V and the smallest bubble with $\varphi_s(0) \approx 1$. Fig. 5.3(b) shows one example result.

Like in the previous chapters, the cell density is calculated as the number of bubbles per unit volume of polymer, i.e., the inverse of the product of the bubble box volume times the global polymer volume fraction.

5.2 Maximal Cell Density

5.2.1 Different Temperature Cases with the Same Initial High Pressure

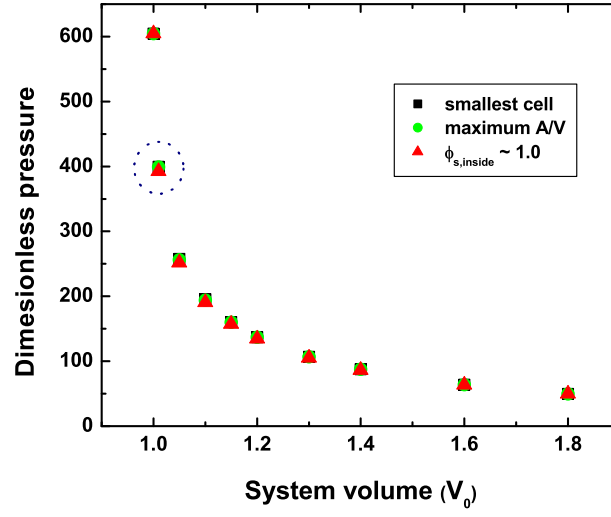
First, we examine a case of different dimensionless temperatures $T = 1.5$ and $T = 2.0$ with the same initial high pressure. We assume a dimensionless temperature dependence for each Flory-Huggins parameters $\chi_{pp}N$, $\chi_{ss}N$, and $\chi_{ps}N$ of

$$\chi N = \frac{A}{T} + B, \quad (5.15)$$

where we choose $A_{pp} = -12$, $A_{ss} = 0$, $A_{ps} = 270$, and all B 's as zero. We assume a weak attractive interaction between polymer molecules and a strong repulsive interaction between polymer and solvent molecules. We think of the phase of the solvent as a gas phase. Therefore, for $T = 1.5$, the χ values are $\chi_{pp}N = -8$, $\chi_{ss} = 0$, and $\chi_{ps}N = 180$, and for $T = 2.0$, $\chi_{pp}N = -6$, $\chi_{ss} = 0$, and $\chi_{ps}N = 135$. For the same initial pressure, we choose the initial solvent volume fraction $\phi_s^0 = 0.26$ for $T = 1.5$, and $\phi_s^0 = 0.31$ for $T = 2.0$. From the data, we observe that with our χN values, the solubility is higher at higher temperature. This means our solvent is a nitrogen N_2 like solvent not a carbon dioxide CO_2 like, because N_2 has higher solubility at higher temperature and CO_2 has higher solubility at lower temperature. We will discuss this more later in the discussion and conclusions section.

Fig. 5.4 (a) shows the three optimal pressures as a function of the system volume at $T = 1.5$. Due to the scale of the plot, the three optimal pressure values seem the same, but

(a)



(b)

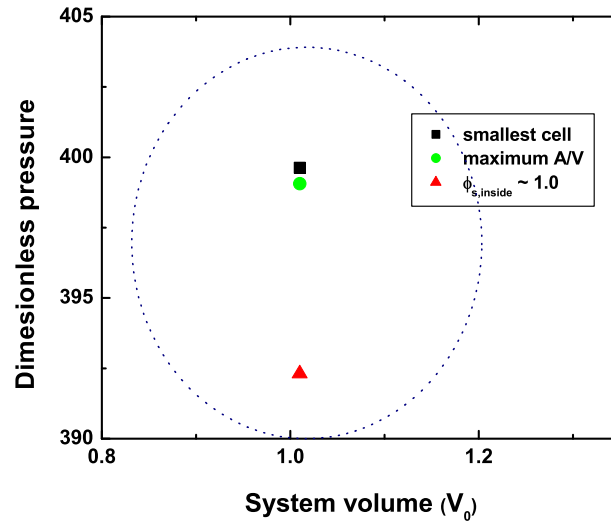


Figure 5.4: At $T = 1.5$ (a) Three optimal pressures versus system volume. (b) Blow up plot of optimal pressure values at $V_{sys} = 1.1V_0$.

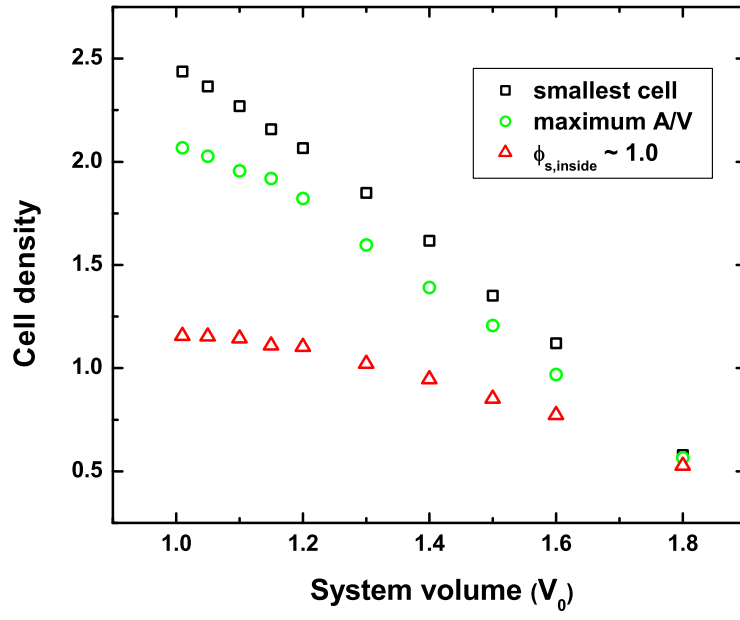


Figure 5.5: Three maximal cell densities corresponding to three optimal pressures versus system volume at $T = 1.5$.

if we blow up the pressure values at $1.01 V_0$, in the blow-up Fig. 5.4 (b) one can see that the pressure of the smallest bubble is the highest and the pressure of $\varphi_s(0) \approx 1.0$ bubble is much lower than the smallest bubble pressure. From this, we can say that for the better quality bubble formation, the system pressure needs to be dropped more.

Fig. 5.5 shows cell density as a function of system volume corresponding to the three optimal pressures. From this plot, we can easily see that at the smallest system volume, $V = 1.01V_0$, the foam has the highest cell density for all three optimal pressures. Therefore, the incompressible system cell density must be the upper bound of the maximal cell density for all three optimal pressures.

Also, unlike the incompressible system, Fig. 5.5 gives information on how much the system expand before the system is in the spinodal region. We notice that for systems bigger than $V = 1.8V_0$, i.e., 80% expansion, our code does not form a bubble, and the nucleation barrier approaches zero. We assume the system approaches to the spinodal region as the nucleation barrier approaches zero.

We examine another temperature case $T = 2.0$ which has the same initial high pressure as the $T = 1.5$ case. As mentioned above, with our χN values the solubility is higher at high temperature. For $T = 2.0$, $\phi_s^0 = 0.31$, which is bigger than the solubility of $T = 1.5$ case, $\phi_s^0 = 0.26$.

Fig. 5.6 (a) shows the three optimal pressures for $T = 2.0$. If we blow up the pressures at $V = 1.01V_0$, Fig. 5.6 (b) shows that compared to $T = 1.5$ the pressure difference between the smallest bubble and the $\varphi_s(0) \approx 1$ bubble is smaller than $T = 1.5$ case. And, we also notice that the cell density difference between the smallest and the $\varphi_s(0) \approx 1$ bubble is smaller than $T = 1.5$ case. In addition, like the $T = 1.5$ case, the pressure of the $\varphi_s(0) \approx 1$ bubble is lower than the pressure of the critical radius. This means for a better quality foam it needs to drop more pressure, i.e. a higher pressure drop.

Fig. 5.7 shows the cell density of three optimal pressures for $T = 2.0$ as a function of system volume. We also notice that at the smallest system volume the foam has the highest cell density; thus, we conclude that the incompressible system has the upper bound maximal cell density.

Now, to compare the two temperature cases, we choose the optimal pressure of the $\varphi_s(0) \approx 1$ bubble as the optimal pressure of a good quality foam as we did in the previous chapter. From this point, in this chapter, the optimal pressure means the optimal pressure

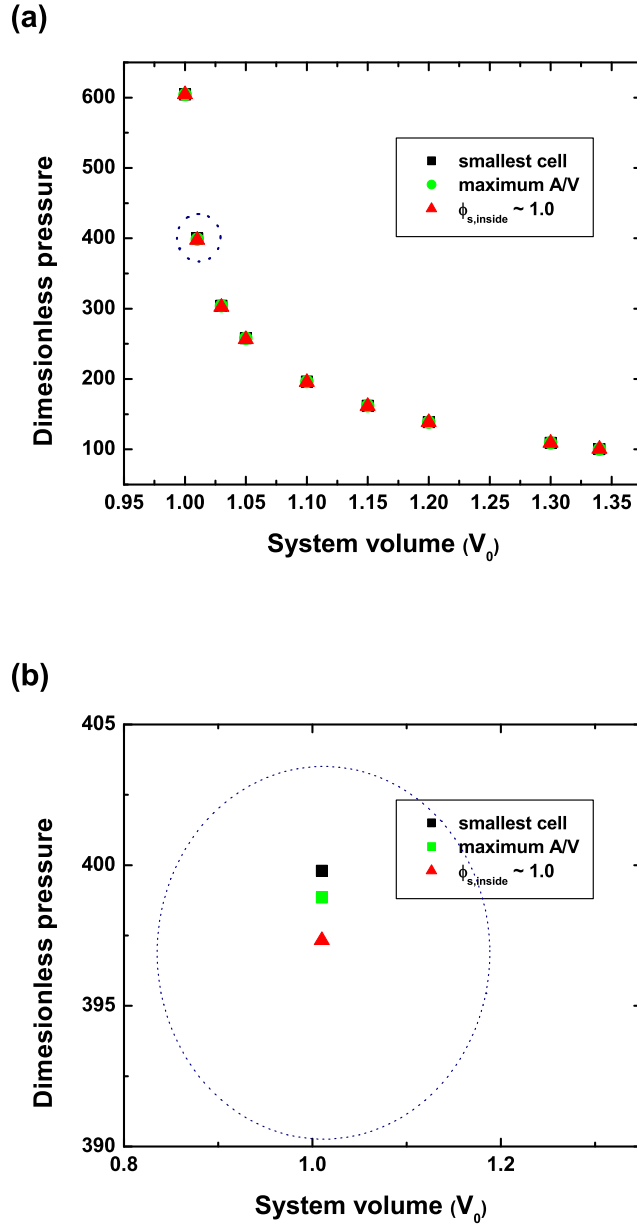


Figure 5.6: At $T = 2.0$ (a) Three optimal pressures versus system volume. (b) Blow up plot of optimal pressure values at $V_{sys} = 1.1V_0$.

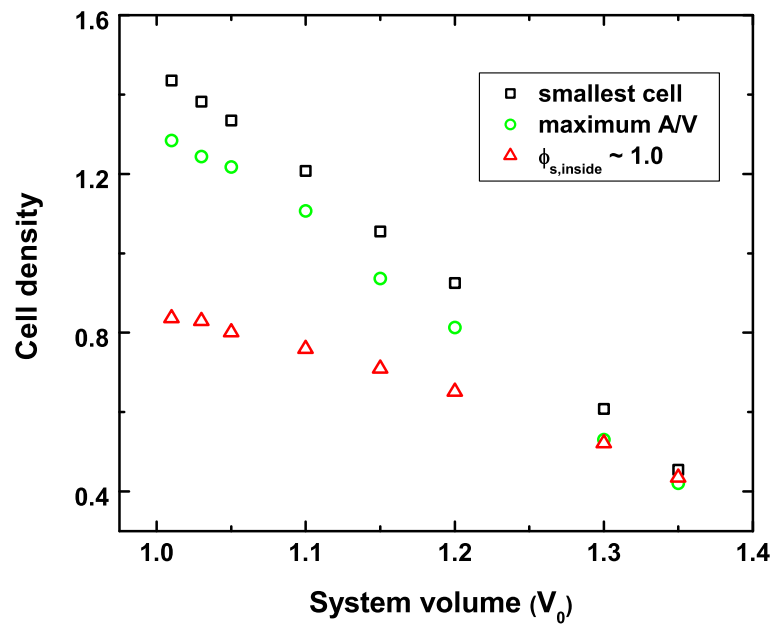


Figure 5.7: Three maximal cell densities corresponding to the three optimal pressures versus system volume at $T = 2.0$.

of the smallest bubble with $\varphi_s(0) \approx 1$.

Fig. 5.8 (a) shows an inhomogeneous system pressure and a homogeneous system pressure as a function of system volume at $T = 1.5$ and $T = 2.0$. Inhomogeneous system means a system in which representative bubbles are filled in, and homogeneous system means a system in which there is no bubble.

In the blow up figures Fig. 5.8 (b) and (c) we can see that the pressure difference between the inhomogeneous system and the homogeneous system is bigger for the lower temperature $T = 1.5$. Also, from Fig. 5.9 (a) which shows the cell density as a function of system volume for each temperature $T = 1.5$ and $T = 2.0$, we observe that the cell density is higher for lower temperature $T = 1.5$ despite a lower solubility than $T = 2.0$.

Therefore, we assume that the bigger pressure difference between the inhomogeneous system and the homogeneous system for $T = 1.5$ causes the cell density higher for $T = 1.5$ despite the lower solvent density. Also, from this result, we assume that the temperature is a more dominant factor than solubility.

In addition, the blow up figure Fig. 5.8 (c) shows the pressure difference between the homogeneous system and the inhomogeneous system at $V = 1.05V_0$ is bigger than the pressure difference at $V = 1.3V_0$ for each temperature $T = 1.5$ and $T = 2.0$. Fig. 5.9 (a) shows cell density at $V = 1.05V_0$ is higher than cell density at $V = 1.3V_0$ for each temperature $T = 1.5$ and $T = 2.0$. We can conclude that higher cell density at smaller system volume is also from the bigger pressure difference between the homogeneous system and the inhomogeneous system at smaller system volume.

Consequently, we assume that to make foams of a high cell density of a good quality, a big pressure drop is required before the system expands, i.e., a high pressure drop rate.

With our reasoning, from Fig. 5.8 (c), we can see that if the two systems have the same pressure at $V = 1.3V_0$, then higher temperature $T = 2.0$ would have a higher cell density, because if the two systems have the same pressure at $V = 1.3V_0$, the pressure difference between the homogeneous system and the inhomogeneous system of higher temperature $T = 2.0$ would be bigger than the corresponding value of $T = 1.5$. Thus, we need to emphasize that we deal with the possible maximal cell density under a condition that systems have the optimal pressure.

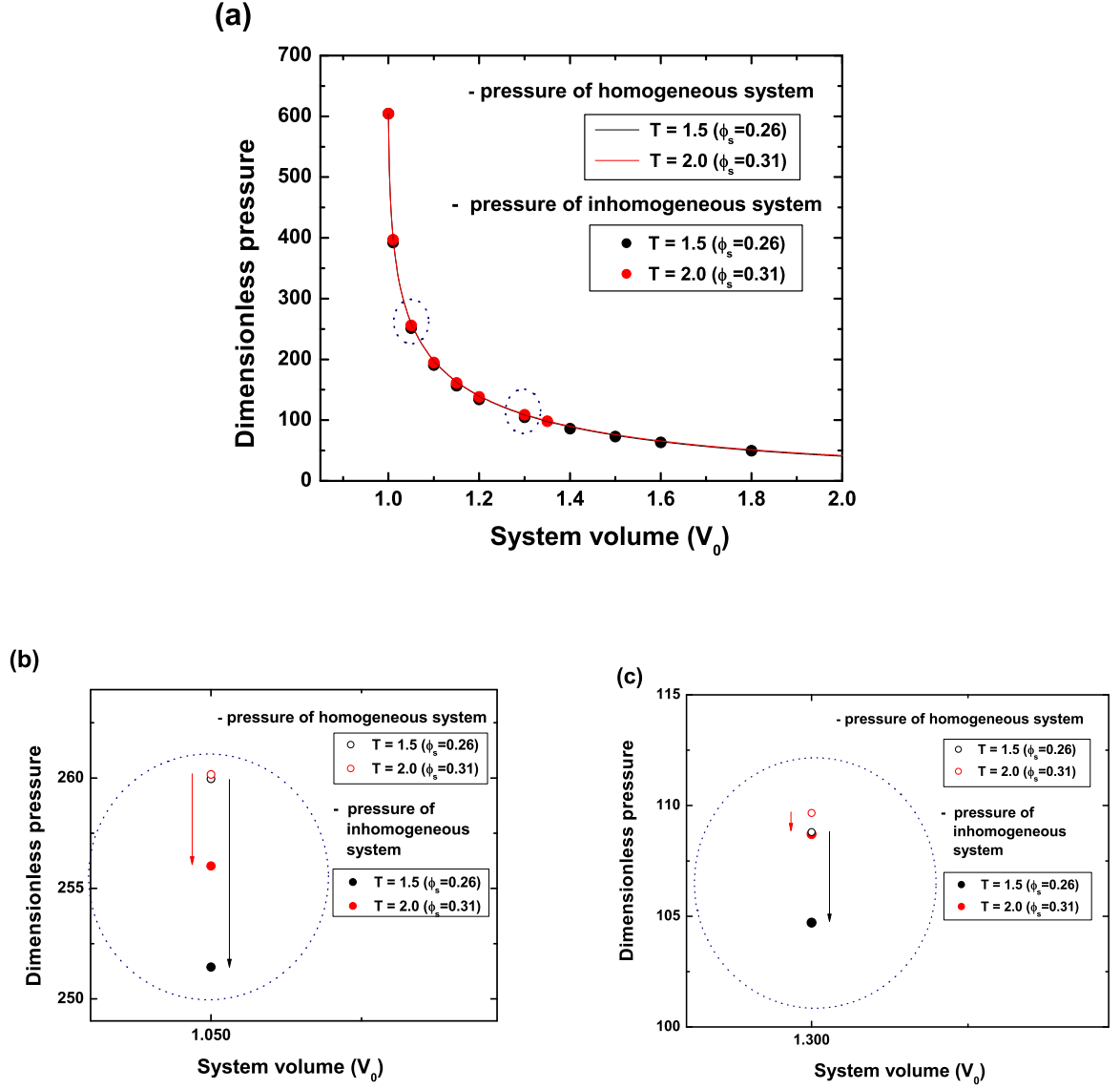


Figure 5.8: At $T = 1.5$ and $T = 2.0$ (a) Pressure of the inhomogeneous system and the homogeneous system versus system volume (b) Blow up plot of the pressure at $V = 1.05V_0$. (c) Blow up plot of the pressure at $V = 1.3V_0$.

(a)

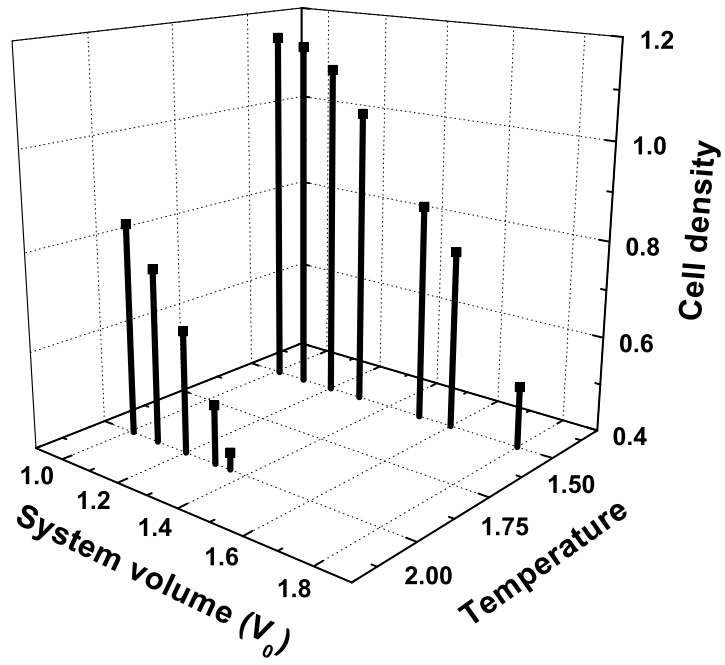


Figure 5.9: Cell density versus system volume at $T = 1.5$ and $T = 2.0$

On the other hand, we also see that at lower temperature, the system expands more. We assume that the initial higher cell density at lower temperature causes the system volume expand more.

5.2.2 Different Solvent Density Cases at the Same Temperature

In the previous chapter, we examined different solubility cases (different solvent volume fraction cases) at the same temperature. To check in the compressible system if we get the same result as the incompressible system, we examined different solubility cases at the same temperature in this section. We used the same parameter values as the incompressible system, $\chi N = 120$ ($\chi_{pp}N = -6$, $\chi_{ss}N = 0$, $\chi_{ps}N = 117$) with ϕ_s ranging from 0.32 to 0.39.

Fig. 5.10 shows the optimal pressure of $\varphi_s(0) \approx 1$ bubble as we mentioned above, as we can expect, despite of the scale of the plot we see that the highest solubility $\phi_s = 0.39$ has the highest initial high pressure. The blow up Fig. 5.10 (b) and (c) show that the pressure difference from the homogeneous system is bigger for higher solvent density. Therefore, we expect a higher solvent case would have a higher cell density.

Fig. 5.11 shows the results of the cell density of the three solubility cases as a function of system volume. As we expect, a higher solvent case has a higher cell density, and also expands more in a higher solvent case.

Thus, we can conclude that for the different solvent density cases at the same temperature, the compressible system result is the same as the incompressible result - a higher cell density at a higher solubility.

In addition, from Fig. 5.10 (a),(b) and Fig. 5.11, we can see

5.2.3 Different Temperature Cases with the Same Solvent Volume Fraction

As we did in the previous chapter, to investigate the effect of temperature on cell density, we examine different χN value cases, i.e., $\chi N = 120$ ($\chi_{pp}N = -6$, $\chi_{ss}N = 0$, $\chi_{ps}N = 117$)

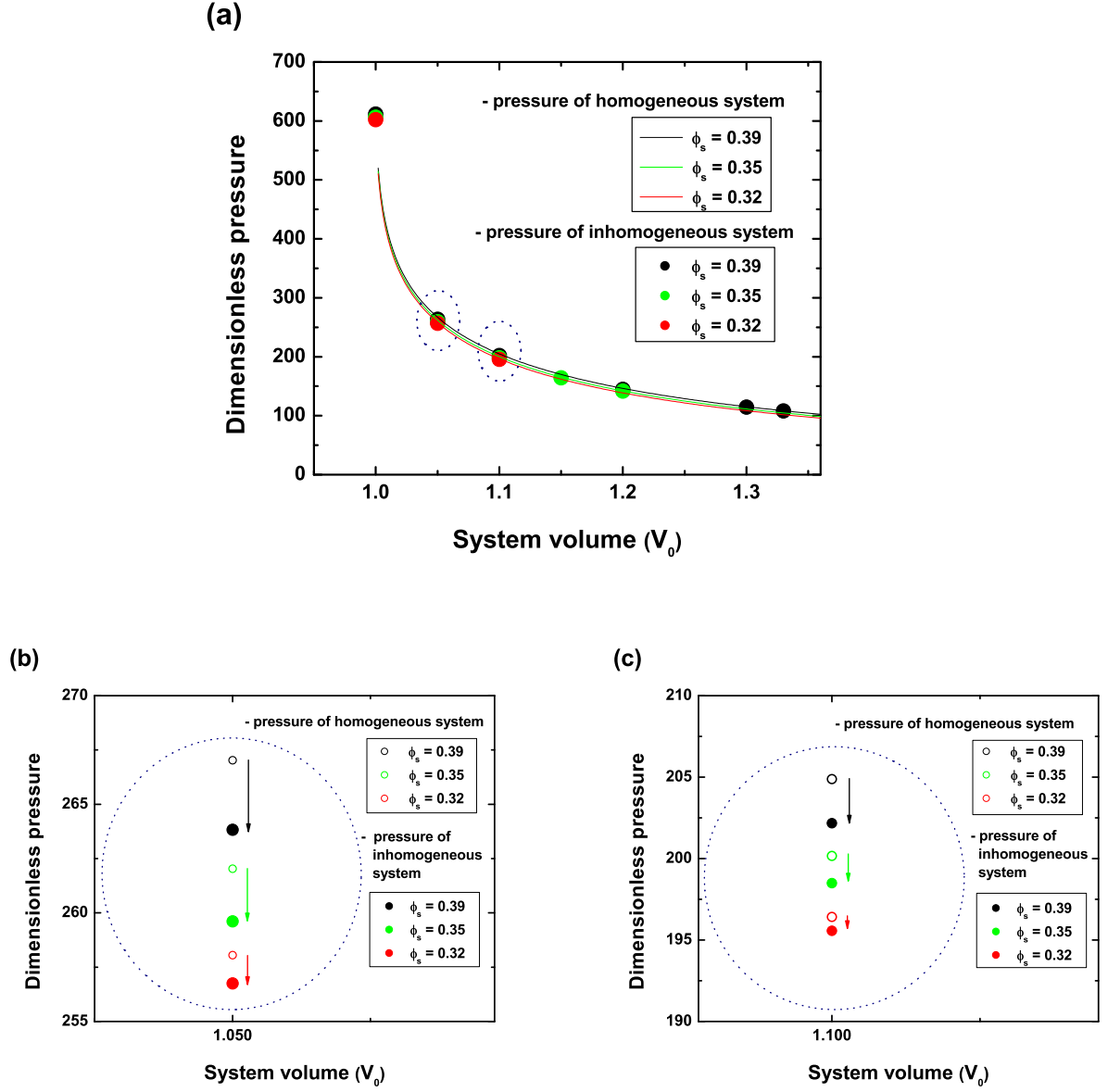


Figure 5.10: At different solvent volume fractions (solubilities) for $\chi N = 120$ (a) Pressure of the inhomogeneous system and the homogeneous system versus system volume (b) Blow up plot of the pressure $V = 1.05V_0$. (c) Blow up plot of the pressure at $V = 1.1V_0$

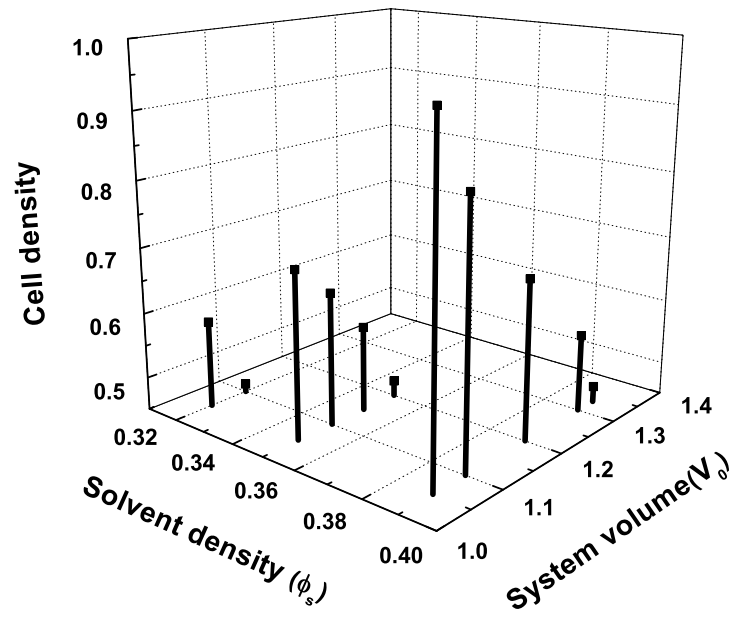


Figure 5.11: Cell density versus system volume at different solvent volume fractions (solubilities) for $\chi N = 120$

and $\chi N = 160$ ($\chi_{pp}N = -8$, $\chi_{ss}N = 0$, $\chi_{ps}N = 156$) with the same solvent volume fraction $\phi_s = 0.32$. Fig. 5.12 (a) shows the optimal pressure of the two cases and the corresponding homogeneous system pressure as a function of system pressure. We see at $\chi N = 160$, the low temperature case needs higher pressure to have the same solubility as the $\chi N = 120$, high temperature, as we expect. In figure Fig. 5.12 (b) we see a much bigger pressure difference between the inhomogeneous system pressure and the homogeneous system pressure at $\chi N = 160$. Thus, we can expect a much bigger higher cell density at $\chi N = 160$ which we can see in Fig. 5.13 (a). Also, though we didn't calculate a bigger system case than $1.3V_0$ for $\chi N = 160$, we see more expansion at $\chi N = 160$.

Consequently, for the different temperature cases with the same solvent volume fraction, we also get the same result as the incompressible system - low temperature has a higher cell density. In addition, we see also a bigger volume expansion at $\chi N = 160$, low temperature. We assume that this is from the higher cell density due to the bigger pressure difference between the inhomogeneous system pressure and homogeneous system pressure at the smallest system volume for $\chi N = 160$.

5.3 Discussion and Conclusion

In this chapter, we chose the optimal pressure of $\phi_s(0) \approx 1$ bubble as the system pressure, and calculated pressure of inhomogeneous system and the homogeneous system, cell density as a function of system volume.

Our compressible system prediction of cell density shows that the incompressible system cell density is the upperbound of the maximal cell density. Thus, in view of cell density the compressible system predictions are consistent with the incompressible system predictions - Low temperature and high solvent volume fraction have a higher maximal cell density[47, 41].

We noticed that when the system expands, the nucleation barrier approaches zero, and our code doesn't form a bubble as the nucleation barrier approaches to zero . (around $\sim 10^{-3}$) We assume the system approaches the spinodal region when the nucleation barrier approaches zero.

We investigated three cases - different temperatures with the same initial high pressure; different solvent volume fraction at the same temperature; and different temperatures with

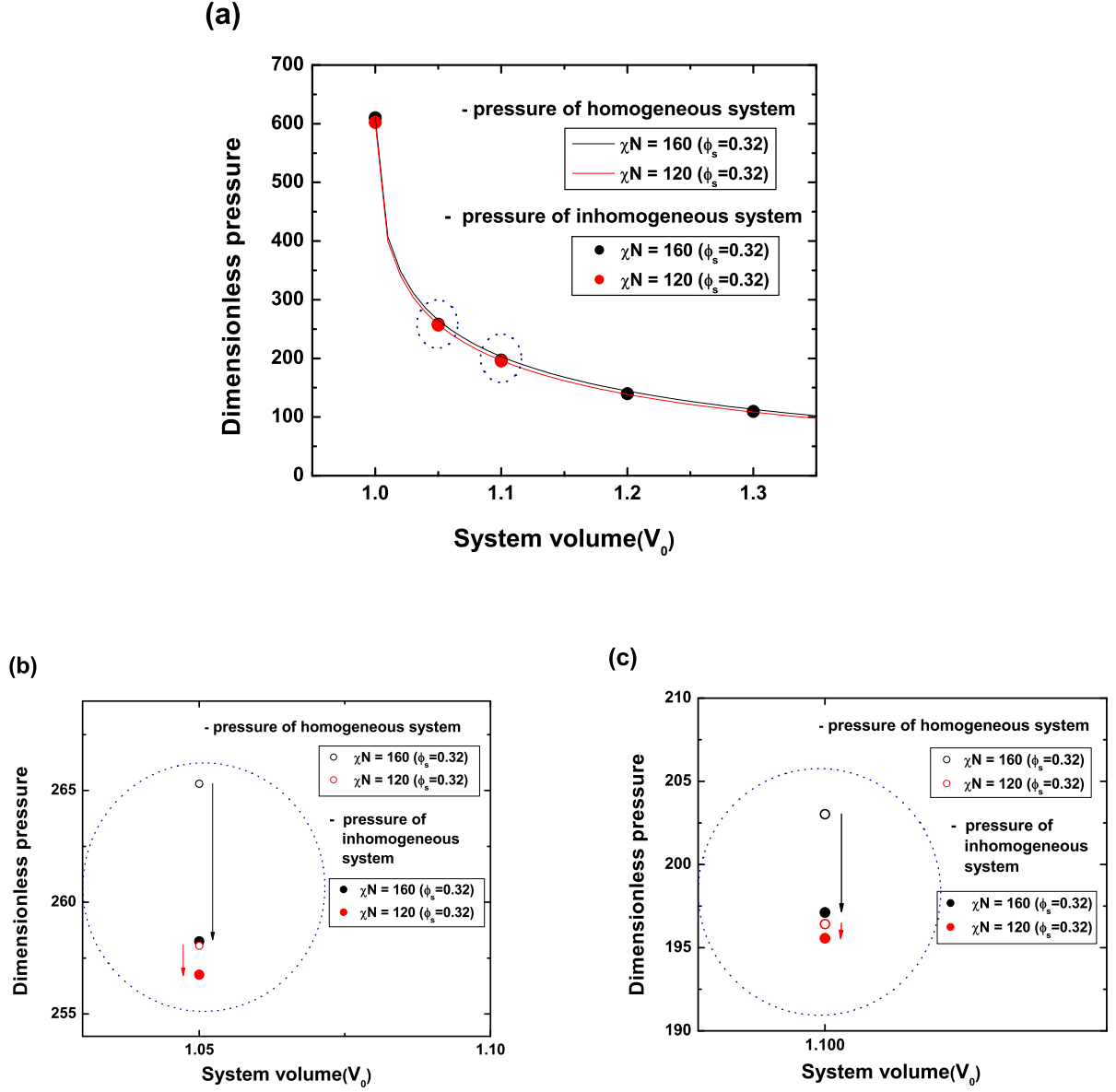


Figure 5.12: At $\chi N = 120$, $\phi_s = 0.32$ and $\chi N = 160$, $\phi_s = 0.32$ (a) Pressure of the inhomogeneous system and the homogeneous system versus system volume (b) Blow up plot of pressure at $V = 1.05V_0$. (c) Blow up plot of pressure at $V = 1.1V_0$

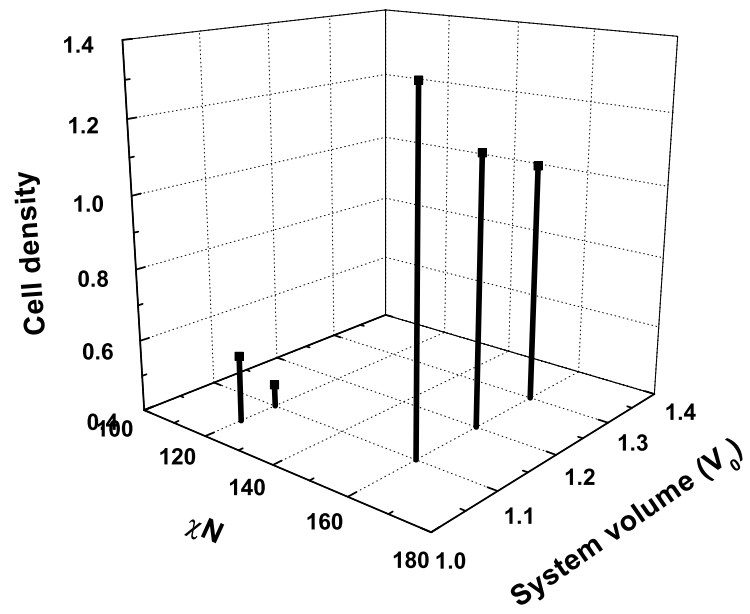


Figure 5.13: Cell density versus system volume at $\chi N = 120$, $\phi_s = 0.32$ and $\chi N = 160$, $\phi_s = 0.32$.

the same solvent volume fraction.

Commonly for all cases, our results show that the highest cell density occurs at the smallest system. And, bigger pressure difference between the homogeneous system and the inhomogeneous system makes higher cell density. Therefore, to make foams of the high cell density with good quality bubbles, high pressure dropping rate is required. [45, 67, 46]. And, also our result - high cell density at low temperature and high cell density for a high pressure drop rate - is similar with carbon dioxide case. Thus, since usually in experiments of nitrogen solvent the solubility is very small, by using a higher χ_{ps} and lower solubility, we can compare the results with the experimental results of nitrogen case - there is little effect of temperature and pressure drop rate on cell density.

On the other hand, by raising the pressure we can increase solubility with the same temperature or lower temperature with same solubility. Our results show lowering temperature is a more efficient way to get a better quality foam than increasing solubility, which is consistent with the result of the previous chapter - temperature is a dominant factor.

As for the solubility, according to our investigation, with magnitude of χ_{ps} smaller than half the magnitude of χ_{pp} or if χ_{ps} has minus sign, the solubility has higher at lower temperature which is a character of the solubility of CO_2 [52]. However, our code does not make a cell if we use above parameter values. Thus, to investigate the CO_2 case, we might need to use the Simha -Chomkynsky eq. in which a van der Waals interaction potential used. Or a modified Sanchez -Lacombe eq. can be used by setting polymer segment volume and hole volume differently, i.e., $v_p^* \neq v_h^*$.

Chapter 6

Conclusions

We studied cell nucleation and growth in nano polymer foams in this thesis. For the calculation of the inhomogeneous polymer system free energy we used self-consistent field theory (SCFT).

As our research is about nano-sized bubbles, which are comparable in size to polymer molecules, we represented a bubble surface as a curved surface, and investigated the curvature effect on cell nucleation. Unlike classical nucleation theory (CNT), in which values of surface tension γ and volume free energy density ΔF_V are constant, our results show that surface tension γ is decreasing and (negative) volume free energy density, $-\Delta F_V$, is increasing for smaller bubbles (higher curvature). We investigated the microscopic origins of the decreasing surface tension γ and increasing (negative) volume free energy density $-\Delta F_V$ at smaller bubbles by breaking down the components of free energy. It turns out that the higher curvature of small bubbles gives polymer molecules more available configurations leading to the lower internal energy, and also the bulk phase breakdown inside smaller bubbles decreases the internal energy. Consequently, our SCFT results show that nano-polymeric bubbles have a much smaller nucleation energy, i.e., a much larger nucleation rate than predicted by CNT ; therefore, we can expect a much higher possibility of homogeneous nucleation than previously calculated by CNT.

In our model, each bubble we make is a representative bubble of each corresponding sample system. With our model, we directly calculated the maximal cell density as a function of bubble radius without calculation of nucleation barrier and nucleation rates in CNT. We investigated under what conditions of parameters such as temperature and

solvent density better foams might be formed in view of cell density and cell size. Our results show that at one given temperature, CNT and SCFT predictions are the same - better foam at higher solvent density. However, for different temperatures, SCFT predictions show that a better foam (higher cell density and smaller cell size) is formed at lower temperatures despite lower solvent density, and it turns out that the free volume energy density, ΔF_V , is a more dominant factor than surface tension γ for cell density and critical cell size predictions. This is not revealed by CNT.

We calculated the maximal density in compressible systems as well as the incompressible system. We used hole-based SCFT for compressible system calculations. With an assumption that our system has an optimal pressure at which the system has the maximal cell density with a good quality bubble, i.e., bulk condition inside a bubble, we calculated inhomogeneous system pressure, homogeneous system pressure, maximal cell density, expansion ratio, and void fraction as functions of system volume.

We observed that when system volume expands nucleation barrier approaches to zero, and we couldn't make a bubble when the nucleation barrier is very small. Thus, we assumed that when the nucleation barrier approaches to zero, system approaches to spinodal region, and we assumed the biggest system volume which we could make is the final system volume.

Therefore, with data of cell density, pressure, expansion ratio, and void fraction we could investigate maximal density, expansion ratio and cell morphology of the final system depending on different processing conditions - different temperatures with same initial high pressure, different solvent density cases at the same temperature, and different temperatures with same solvent volume fraction. First of all, our results showed that the incompressible maximal cell density is the upper bound of the maximal cell density, and qualitatively consistent with the compressible prediction; higher cell densities at lower temperatures and higher solvent densities.

Our compressible systems also showed higher expansion ratio at low temperature and high solvent densities. Since we noticed that the pressure difference between homogeneous system and inhomogeneous system is bigger at low temperature and high solvent cases, we concluded that the bigger pressure difference between homogeneous system and inhomogeneous system must cause the higher cell density, and the initial higher cell density must cause the bigger final system volume. We also observed that for all our results, the smallest volume has the highest cell density, thus; big pressure drop rate is required for high cell density of good quality foams.

In addition, though higher solubility and low temperature make a higher cell density,

our results showed temperature is a more dominant factor for a higher cell density. From one system if we can raise solubility or lower temperature by raising a same amount of the initial pressure, it turns out that raising temperature is more efficient to make a higher cell density of good quality foam, but a bigger pressure drop rate was required.

On the other hand, overall our void fraction values were high since our system has a high solubility. And, though our solvent type is nitrogen since with our χ values, our compressible system has higher solvent density at higher temperature[52], our results were similar with the carbon dioxide results - significant effect of temperature and pressure drop rate on cell density. In experiments using nitrogen, usually the solubility is very small, and results show little effect of temperature and pressure drop rate on cell density[25].

Therefore, for future work, we can use bigger χ_{ps} and smaller solubility, and compare the results with the experimental results, i.e., the extent of the effect of processing condition on cell density.

In addition, we observed that if the magnitude of repulsive force between polymer and solvent, χ_{ps} , was approximately smaller than half the magnitude of attractive force between polymer molecules χ_{pp} or if repulsive force between polymer and solvent, χ_{ps} , was negative, then the solubility is higher at lower temperatures, which is a character of the solubility of carbon dioxide. If we use the range of above χ_{ps} values, our code didn't make a bubble. We assume the pair wise contact potential of the molecules interaction of our model might cause the incapability for the carbon dioxide case. According to our investigation of χ_{ps} values, the repulsive force of carbon dioxide and polymer molecules must be much smaller than the repulsive force of nitrogen and polymer molecules. thus; interaction range between carbon dioxide and polymer molecules must be bigger. Therefore, for the investigation of the solvent carbon dioxide case, we might need to use the Simha - Somcynsky equation[54, 20], because in Simha - Somcynsky equation, van der Waals potential which has a longer attractive interaction range than our model is used.

On the other hand, in our model, by setting the closed packed polymer segment volume is equal to hole volume, our code was based on Sanchez -Lacombe equation, but we might use a modified Sanchez -Lacombe equation [51, 23] by setting the closed packed polymer segment volume and hole volume differently, i.e., $v_p^* \neq v_h^*$.

Furthermore, we noticed that our results showed different homogeneous system pressure for different χ values, thus; we might investigate effects of different χ or α values on foams

quality. And, our calculation was qualitative calculation, but quantitative calculation and comparison with experiment would give more insight about bubble nucleation and growth mechanisms.

Permissions

This is a License Agreement between Yeongyoon Kim ("You") and Elsevier ("Elsevier") provided by Copyright Clearance Center ("CCC").

Supplier : Elsevier Limited
The Boulevard, Langford Lane
Kidlington, Oxford, OX5 1GB, UK
Registered Company Number : 1982084
Customer name : Yeongyoon Kim
Customer address : 314 B
Waterloo, ON N2L 6P4
License number : 3016000076124
License date : Oct 25, 2012
Licensed content publisher : Elsevier
Licensed content publication : Polymer
Licensed content title :
Towards maximal cell density predictions for polymeric foams
Licensed content author :
Yeongyoon Kim, Chul B. Park, P. Chen, Russell B. Thompson
Licensed content date : 10 November 2011
Licensed content volume number : 52
Licensed content issue number : 24
Number of pages : 8
Start Page : 5622
End Page : 5629
Type of Use : reuse in a thesis/dissertation
Intended publisher of new work : other
Portion : full article

Format : electronic
Are you the author of this Elsevier article? : Yes
Will you be translating? : No
Order reference number
Title of your thesis/dissertation :
Study of cell nucleation in nano polymer foams : SCFT approach
Expected completion date : Oct 2012
Estimated size (number of pages) : 91
Elsevier VAT number : GB 494 6272 12
Permissions price : 0.00 USD
VAT/Local Sales Tax : 0.0 USD / 0.0 GBP
Total : 0.00 USD

References

- [1] M. Amon and C. D. Denson. A study of the dynamics of foam growth: Analysis of the growth of closely spaced spherical bubbles. *Polym. Eng. Sci.*, 24(13):1026–1034, 1984.
- [2] D. F. Baldwin, D. Tate, Park. C. B., S. W. Cha, and N. P. Suh. Microcellular plastics processing technology (1). *J. Jpn. Soc. Polym. Proc.*, 6:187, 1994.
- [3] D. F. Becker and W. Doring. *Ann. Phys.*, 24:719, 1935.
- [4] K. Binder, M Muller, P. Virnau, and L. G. MacDowell. Polymer + Solvent systems: phase diagrams, interface free energy, and nucleation. *Adv. Polym. Sci.*, 173:1, 2005.
- [5] J. S. Colton and N. P. Suh. The nucleation of microcellular thermoplastic foam with additives: Part 2: Experimental results and discussion. *Polym. Eng. Sci.*, 27(7):493–499, 1987.
- [6] J. S. Colton and N. P. Suh. The nucleation of microcellular thermoplastic foam with additives: Part 1: Theoretical consideration. *Polym. Eng. Sci.*, 27(7):485–492, 1987.
- [7] A. Das. *Field Theory: A path integral approach*. World Scientific, Singapore, 2006.
- [8] G. T. Dee and B. B. Sauer. The molecular weight and temperature dependence of polymer surface tension: Comparison of experiment with interface gradient theory. *J. Colloid. Interf. Sci.*, 152:85–103, 1992.
- [9] G. T. Dee and B. B. Sauer. The surface tension of polymer liquids. *Adv. Phys.*, 47:161–205, 1998.
- [10] G. H. Fredrikson. *The equilibrium theory of inhomogeneous polymers*. Oxford University Press, New York, 2006.

- [11] Y. Fujimoto, S. S. Ray, and M. Okamoto. Well controlled biodegradable nanocomposite foams: from microcellular to nanocellular. *Macromol. Rapid Comm.*, 24:457–461, 2003.
- [12] S. Ghosh and S. K. Ghosh. Homogeneous nucleation in vapor-liquid phase transition of Lennard-Jones fluids: A density functional theory approach. *J. Chem. Phys.*, 134(024502):1–8, 2011.
- [13] S. K. Goel and E. J. Beckman. Generation of microcellular polymeric foams using supercritical carbon dioxide. 1: Effect of pressure and temperature on nucleation. *Polym. Eng. Sci.*, 34(14):1137–1147, 1994.
- [14] X. Han, K. W. Koelling, D. L. Tomasko, and L. J. Lee. Continuous microcellular polystyrene foam extrusion with supercritical study. *Polym. Eng. Sci.*, 42:2094–2106, 2002.
- [15] M. M. Hasan, Y. G. Li, G. Li, C. B. Park, and P. Chen. Determination of solubilities of CO_2 in linear and branched polypropylene using a magnetic suspension balance and a PVT apparatus. *J. Chem. Eng. Data*, 55:4885–4895, 2010.
- [16] Eugene Helfand. Theory of inhomogeneous polymers: Fundamentals of the Gaussian random-walk model. *J. Chem. Phys.*, 62:999–1005, 1995.
- [17] K. Hong and J. Noolandi. Conformational energy effects in a compressible lattice fluid theory of polymers. *Macromolecules*, 14:1229–1234, 1981.
- [18] K. Hong and J. Noolandi. Theory of inhomogeneous multicomponent polymer systems. *Macromolecules*, 14:727–736, 1981.
- [19] S. Ito, K. Matsunaga, M. Tajima, and Y. Yoshida. Generation of microcellular polyurethane with supercritical carbon dioxide. *J. Appl. Polym. Sci.*, 106:3581–3586, 2007.
- [20] R. K. Jain and R. Simha. On the statistical thermodynamics of multicomponent fluids: Equation of state. *Macromolecule*, 13(6):1501, 1980.
- [21] R. A. L. Jones and R. W. Richards. *Polymers at Surfaces and Interfaces*. Cambridge University Press, Cambridge, 1999.
- [22] B. Krause, K. Dickmann, van der Vegt, and Wessling N. F. A. Open nanoporous morphologies from polymeric blends by carbon dioxide foaming. *Macromolecules*, 35:1738–1745, 2003.

- [23] R. H. Lacombe and I. C. Sanchez. Statistical thermodynamics of fluid mixtures. *J. Phys. Chem.*, 80(23):2568, 1976.
- [24] J. G. Lee and R. W. Flumerfelt. A refined approach to bubble nucleation and polymer foaming process: Dissolved gas and cluster size effects. *J. Colloid Interf. Sci.*, 184:335–348, 1994.
- [25] J. W. S. Lee and C. B. Park. Use of nitrogen as a blowing agent for the production of fine-celled high-density HDPE foams. *Macromol. Mater. Eng.*, 291:1233–1244, 2006.
- [26] S. T. Lee, B. C. Park, and N. S. Ramesh. *Polymeric Foams: Science and Technology*. CRC press, Boca Raton, 2007.
- [27] D. G. LeGrand and G. L. Gains. The molecular weight dependence of polymer surface tension. *J. Colloid. Interf. Sci.*, 31:162–167, 1969.
- [28] S. N. Leung, A. Wong, Q. Guo, C.B. Park, and J. H. Zong. Change in the critical nucleation radius and its impact on cell stability during polymeric foaming process. *Chem. Eng. Sci.*, 64:4899–4907, 2009.
- [29] S. N. Leung, A. Wong, C. B. Park, and Q. Guo. Strategies to estimate the pressure drop threshold of nucleation for polystyrene foam with carbon dioxide. *Ind. Eng. Chem. Res.*, 48:1921–1927, 2002.
- [30] G. Li, J. Wang, C. B. Park, P. Moulinie, and R. Simha. Comparison of ss-based and sl-based estimation of gas solubility. *ANTEC2004*, pages 2566–2575, 2004.
- [31] G. Li, J. Wang, C. B. Park, and R. Simha. Measurement of gas solubility in linear/branched PP melts. *J. Polym. Sci. Pol. Phys.*, 45:2497–2508, 2007.
- [32] L. Li, H. Yokoyama, T. Nemoto, and K. Sujiyama. Facile fabrication of nanocellular block copolymer thin films using supercritical carbon dioxide. *Adv. Mater.*, 16:1226–1229, 2004.
- [33] J. Matini, F. A. Waldman, and N. P Suh. The production and analysis of microcellular thermoplastic foams. *SPE ANTEC Technol. paper*, 28:674, 1982.
- [34] M. W. Matsen. The standard gaussian model for block copolymer. *J. Phys-Condens Mat.*, 14:R21–R47, 2002.
- [35] M. W. Matsen. Self-consistent field theory and its appilcation. *Soft Matter*, 1:1–84, 2006.

- [36] M. W. Matsen and F. S. Bates. Block copolymer microstructures in the intermediate-segregation regime. *J. Chem. Phys.*, 106:2436–2448, 1997.
- [37] L. M. Matuana and C. A. Diaz. Study of cell nucleation in microcellular poly(lactic acid) foamed with supercritical CO_2 through a continuous-extrusion process. *Ind. Eng. Chem. Res.*, 49:2186–2193, 2010.
- [38] J. Merikanto, E. Zapadinsky, A. Lauri, and H. Vehkamäki. Origin of the failure of classical nucleation theory: incorrect description of the smallest clusters. *Phys. Rev. Lett.*, 98(145702):1–4, 2007.
- [39] M. Müller, L. G. MacDowell, P. Virnau, and K. Binder. Interface properties and bubble nucleation in compressible mixtures containing polymers. *J. Chem. Phys.*, 117:5480, 2002.
- [40] H. E. Naguib, C. B. Park, and P. C. Lee. Effect of Talc content on the volume expansion behavior of extended PP foams. *J. Cell. Plast.*, 39:499, 2003.
- [41] H. E. Naguib, C. B. Park, and N. Reichelt. Fundamental foaming mechanics governing the volume expansion of extruded polypropylene foam. *J. Appl. Polym. Sci.*, 91(4):2661–2668, 2004.
- [42] V. Neimark and A. Vishnyakov. Monte carlo simulation study of droplet nucleation. *J. Chem. Phys.*, 122(145702):1–11, 2005.
- [43] D. W. Oxtoby. Density functional methods in the statistical mechanics of materials. *Annu. Rev. Mater. Res.*, 32:39–52, 2002.
- [44] D. W. Oxtoby and R. Evans. Nonclassical nucleation theory for the gas-liquid transition. *J. Chem. Phys.*, 89:7529, 1988.
- [45] C. B. Park, D. F. Baldwin, and N. P. Suh. Effect of pressure drop rate on cell nucleation in continuous processing of microcellular polymers. *Polym. Eng. Sci.*, 35:432, 1995.
- [46] C. B. Park and N. P. Suh. Filamentary extrusion of microcellular polymers using a rapid decompressive element. *Polym. Eng. Sci.*, 36:34, 1996.
- [47] C. B. Park, A. H. Behraves, and R. D. Venter. Low density, microcellular foam processing in extrusion using CO_2 . *Polym. Eng. Sci.*, 38(11):1812–1823, 1998.

- [48] H. Park, R. B. Thompson, N. Lanson, C. Tzoganakis, C. B. Park, and P. Chen. Effect of temperature and pressure on surface tension of polystyrene in supercritical carbon dioxide. *J. Phys. Chem.*, 111:3859, 2007.
- [49] E. Parra and J. C. Grana. Influence of the attractive pair-potential in density functional models of nucleation. *J. Chem. Phys.*, 132(034702):1–9, 2010.
- [50] B Rathke. Blasenbildung in gasgesättigten Flüssigkeiten: Der Nachweis homogener Keimbildung. *Fortschritt-Berichte*, 3:770, 2003.
- [51] I. C. Sanchez and R. H. Lacombe. An elementary molecular theory of classical fluids. Pure fluids. *J. Phys. Chem.*, 80(21):2352, 1976.
- [52] Y. Sato, M. Yurugi, K. Fujiwara, S. Takishima, and H. Masuoka. Solubilities of carbon dioxide and nitrogen in polystyrene under high temperature and pressure. *Fluid Phase Equilib.*, 125:129–138, 1996.
- [53] S. Schukla and K. W. Koelling. Classical nucleation theory applied to homogeneous bubble nucleation in the continuous microcellular foaming of the polystyrene- co_2 system. *Ind. Eng. Chem. Res.*, 48:7963–7615, 2009.
- [54] R. Simha and T. Somkynsky. On the statistical thermodynamics of spherical and chain molecule fluids. *Macromolecules*, 2:342, 1969.
- [55] V. Talanquer, C. Cunningham, and D. W. Oxtoby. Bubble nucleation in binary mixtures: A semiempirical approach. *J. Chem. Phys.*, 114:6759–6762, 2001.
- [56] V. Talanquer and D. W. Oxtoby. Nucleation of bubbles in binary fluids. *J. Chem. Phys.*, 102:2156–2164, 1995.
- [57] R. B. Thompson, J. R. MacDonald, and P. Chen. Origin of change in molecular-weight dependence for polymer surface tension. *Phys. Rev. E*, 78:030801, 2008.
- [58] R. B. Thompson, C. B. Park, and P. Chen. Reduction of polymer surface tension by crystalized polymer nanoparticles. *J. Chem. Phys.*, 133:144913, 2010.
- [59] R. C. Tolman. Consideration of gibbs theory of surface tension. *J. Chem. Phys.*, 16:758–774, 1948.
- [60] I. Tsivintzelis, Aangelopoulou A. G., and C. Panayiotou. Foaming of polymers with supercritical co_2 . *Polymer*, 48:5928–5939, 2007.

- [61] P. Virnau, M. Muller, L. G. MacDowell, and K. Binder. Phase separation kinetics in compressible polymer solutions: computer simulation of early stages. *New J. Phys*, 6(7), 2004.
- [62] M. Volmer and A. Z. Weber. *Z. Phys. Chem.*, 119:227, 1926.
- [63] D. Weaire and S. Hutzler. *The Physics of Foams*. Oxford University Press, New York, 1999.
- [64] H. Wei, R. B. Thompson, C. B. Park, and P. Chen. Surface tension of high density polyethylene (HDPE) in supercritical nitrogen: effect of polymer crystallization. *Colloid Surface A*, 354:347–352, 2010.
- [65] A. Wong, S. N. Leung, G. Y. G Li, and C. B. Park. Role of processing temperature in polystyrene and polycarbonate foaming with carbon dioxide. *Ind. Eng. Chem. Res.*, 46:7107–7116, 2007.
- [66] X. Xu and C. B. Park. Effects of the die geometry on the expansion ratio of PS foams blown with CO_2 . *SPE ANTEC, technical papers*, 49:1823, 2003.
- [67] X. Xu and C. B. Park. *SPE ANTEC Technical paper*, page 1053, 2005.
- [68] X. Xu, C. B. Park, D. Xu, and R. Pop-Ilieb. Effects of die geometry on cell nucleation of PS foams blown with CO_2 . *Polym. Eng. Sci.*, 43:1378, 2003.
- [69] H. Yokoyama, L. Li, T. Nemoto, and K. Sugiyama. Tunable nanocellular polymeric monoliths using fluorinated block copolymer templates and supercritical carbon dioxide. *Adv. Mater.*, 16:1542–1546, 2004.
- [70] J. B. Zeldovich. *Acta Physicochim*, 18:1, 1943.